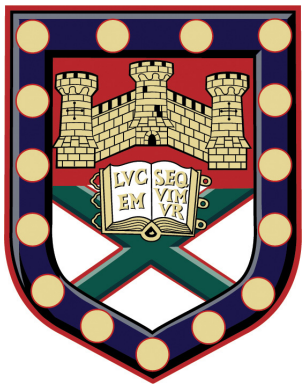

University of Exeter

College of Engineering, Mathematics and Physical Sciences

FUNDAMENTAL PHYSICAL PROPERTIES OF GRAPHENE REINFORCED CONCRETE

Submitted by Dimitar Dimov as a thesis for the degree of

Doctor of Philosophy in Engineering

August 2018

I certify that all material in this thesis which is not my own work has been identified and that no material has previously submitted and approved for the award of a degree by this or any other university.

Dimitar Dimov

Supervisors:

Prof Monica Felicia Craciun

Prof Saverio Russo

Pastoral Mentor:

Prof Akbar Javadi

"At it's heart, engineering is about using science to find creative practical solutions.

It is a noble profession." — Queen Elizabeth II

ABSTRACT

The global warming has increased with unprecedented levels during the last couple of decades and the trend is uprising. The construction industry is responsible for nearly 10% of all carbon emissions, mainly due to the increasing global population and the large demand for housing and civil infrastructure. Concrete, which is the most used construction material worldwide, is found in every type of building as it provides long term structural stability, support and its main constituent – cement, is very cheap. Consequently, due to the raising concerns of high average temperatures, the research community started investigating new, innovative methods for substituting cement with 'greener' materials whilst at the same time improving the intrinsic properties of concrete. However, the manufacturing complications and logistics of these materials make them unfavourable for industrial applications. A novel and truly revolutionary method of enhancing the performance of concrete, thus allowing for decreased consumption of raw materials, lies in nanoengineering the cement crystals responsible for the development of all mechanical properties of concrete. Graphene, a two-dimensional sheet of carbon atoms arranged in a hexagonal lattice, is the most promising nanomaterial for composites' reinforcement to this date, due to it's exceptional strength, ability to retain original shape after strain, water impermeability properties and non-hazardous large scale manufacturing techniques. I chose to investigate the addition of liquid-phase exfoliated graphene suspensions for concrete reinforcement, aiming to improve the fundamental mechanical properties

of the construction material and therefore allowing the industry to design buildings using less volume of base materials. First, the method of liquid exfoliation of graphene was developed and the resulting water suspensions were fully characterised by Raman spectroscopy. Then, concrete samples were prepared according to British standards for construction and tested for various properties such as compressive and flexural strength, cyclic loading, water impermeability and heat transport. A separate, in-depth, study was carried out to understand the formation and propagation of micro-structural cracks between the concrete's internal matrix planes, and graphene's impact on total fracture capacity and resistance of concrete. Lastly, multiple experiments were performed to investigate the microcrystallinity of cement hydration products using X-Ray diffraction. In general, all experimental results show a consistent improvement in concrete's performance when enhanced with graphene on the nanoscale level. The nanomaterial improves the mechanical interlocking of cement crystal, thus strengthening the internal bonds of the composite matrix. This cheap and highly scalable method for producing and mixing graphene with concrete turns it into the first truly applicable method for industrial applications, with a real potential to have positive impact on the global warming by decreasing the production of concrete.

CONTENTS

LIST OF FIGURES

LIST OF TABLES

List of Acronyms

δ_{max} Maximum displacement

ϵ_{pl} Modulus of Plasticity

C_g Concentration of graphene per litre of water

E_c Modulus of Elasticity

E_{cr} Flexural Modulus

G_f Fracture Energy

a_c Critical Length

f_c Compressive Strength of Concrete

f_{cr} Flexural Strength of Concrete

f_{ct} Split Tensile Strength of Concrete

l_{ch} Characteristic Length of Cracks

AFM Atomic Force Microscopy

ASR Alkali Silica Reaction

C_2S Dicalcium Silicate

C_3A Tricalcium Aluminate

C_3S Tricalcium Silicate

C_4AF Tetracalcium Aluminoferrite

C-S-H Calcium Silicate Hydrates

CNT Carbon Nanotubes

CO_2 Carbon Dioxide

CVD Chemical Vapour Deposition

$Ca(OH)_2$ Calcium Hydroxide

$CaCO_3$ Calcium Carbonate

CaO Calcium Oxide

FCM Fictitious Crack Model

FG Functionalised Graphene

FPS Fracture Process Zone

G_{IC}^{un} Unstable Fracture Energy

GNP Graphene Nanoplatelets

GO Graphene Oxide

GS Graphene Supermarket

IG Industrial Graphene

K_{IC}^{e} Critical Stress Intensity Factor

L Length

LEFM Modified Linear Elastic Fracture Mechanics Principles

MLG Multilayer Graphene

MgO Magnesium Oxide

MoS_2 Molybdenum Disulphide

NFM Nonlinear Fracture Mechanics

NFMP Nonlinear Fracture Mechanics Principles

OPC Ordinary Portland Cement

RN US Research Nanomaterials

SCP Sodium Cholate Powder

SEM Scanning Electron Microscopy

SiO_2 Silicon Dioxide

TMD Transition Metal Dichalcogenide

TW Tap Water

UTGr Ultrathin Graphite

XRD X-Ray Diffraction

h-BN hexagonal Boron Nitride

rGO reduced Graphene Oxide

Part I

Introduction and Theory

1

INTRODUCTION

BACKGROUND MOTIVATION

In recent years, the huge economic growth worldwide has raised the overall population on Earth. This inevitably lead to an increase of demand for housing and concrete is the main structural material used, despite the type of property. Consequently, the carbon emissions due to concrete production, have also grown which contributed to change in global temperatures and negative impact on the climate. The construction industry experiences a steady economic growth, with projected budgets of nearly $10 trillion in 2020, according to the Construction Intelligence Center[3]. The most used construction material worldwide – concrete, can be found in every type of building in the civil infrastructure – houses, skyscrapers, bridges, water dams, highways etc. One of its main constituents, cement, accounts for 5%[3] of global CO_2 emissions due to its manufacturing process and the trend has been growing, as shown on Fig.1.1.

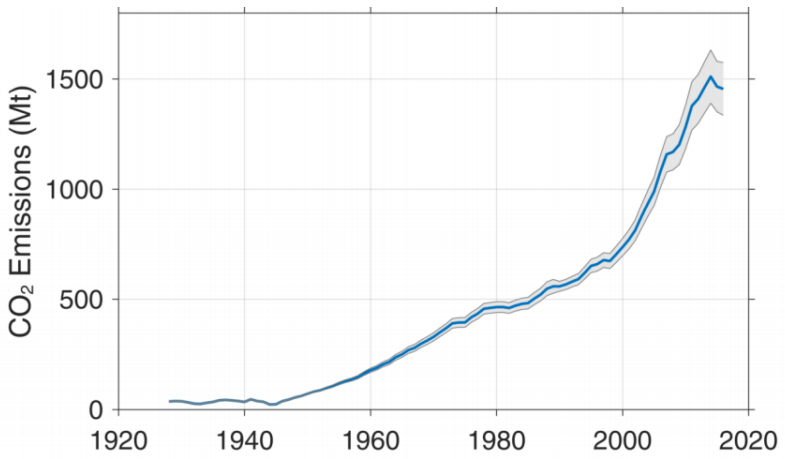

Figure 1.1: Global CO_2 emissions due to cement manufacturing in last decades, adopted from [2].

In the current efforts to reduce the global CO_2 emissions due to cement manufacturing, the main driver is the idea of decreasing the amount of concrete used per m^3, by improving its mechanical performance through various reinforcements. Examples of the latter are conventional steel, fly ash[40], fibers[11;27;46] and silica fume[41], which are some of the many additives used by the industry as reinforcement to reduce the carbon footprint but they are either not very effective, expensive, or require additional industrial admixtures to meet design criteria for building specifications.

However, all these approaches do not consider the fact that concrete itself "is a nano-structured, multi-phase, composite material"[70]. It is composed of an amorphous phase, nanometer to micrometer size crystals, sand and gravel all bound by a reaction between cement and water. The properties of concrete exist in, and the degradation mechanisms occur across, multiple length scales (nano to micro to macro) where the properties of each scale derive from those of the next smaller scale[70]. Therefore one of the best and promising ways to tackle the aforesaid concerns is to look at the nanoscale level as it then determines all the process taking place at micro and macro scales. If the concrete is enhanced at nano-level during the earliest stages of it's development, then the overall properties of this compostie material will be changed and there will be no need

for steel bars or chemical additives.

Since nanotechnology was introduced by Nobel laureate Richard P. Feynman during his now famous 1959 lecture "There's Plenty of Room at the Bottom," [70], there have been many revolutionary developments in physics, chemistry, and biology that have demonstrated Feynman's ideas of manipulating matter at very small scale, the level of molecules and atoms, i.e., the nanoscale. While the meaning of "nanotechnology" varies, nanotechnology is commonly defined as the understanding, control, and restructuring of matter on the order of a nanometer to create materials with fundamentally new properties and functions [70].

To date, nanotechnology applications and advances in the construction and building materials fields have not been fully explored because of the conservative nature of the industry. Due to the huge gap between academia and industry, the exploitation of nanotechnology in concrete on a commercial scale remains quite limited. The main advances have been in the nanoscience of cementitious materials [70] with an increase in the knowledge and understanding of basic phenomena in cement at the nanoscale (e.g., structure and mechanical properties of the main hydrate phases, cement hydration, interfaces in concrete, and mechanisms of degradation). Recent advancements in technical equipment for observation and measurement at the nanoscale are providing a wealth of new information about concrete, some of which is confounding previous conventional thinking.

The nanoscience and nano-engineering, sometimes called nanomodification, of concrete are terms that have come into common usage and describe two main avenues of application of nanotechnology in concrete research [70]. Nanoscience deals with the measurement and characterization of the nano and microscale structure of cement-based materials to better understand how this structure affects macroscale properties and performance through the use of advanced characterization techniques and atomistic or molecular level modelling. Nano-engineering encompasses the techniques of manipulation of the structure at atomic scale, to develop a new generation of tailored, multifunctional, cementitious composites with superior mechanical performance and dura-

bility potentially having a range of novel properties such as: low electrical resistivity, self-sensing capabilities, self-cleaning, self-healing, high ductility, and self-control of cracks. Concrete can be nano-engineered by the incorporation of nanosized building blocks to control material behaviour and add novel properties, or by the grafting of molecules onto cement particles, cement phases, aggregates, and additives to provide surface functionality, which can be adjusted to promote specific interplane interactions.[70].

The broad motivation behind this work is to find a sustainable, large-scale application of nanootechnologies which can help reduce the negative effect of concrete use. The main driver is the idea of decreasing the amount of concrete required per m^3 by improving its intrinsic properties. To this date, this thesis presents a novel way of improving the mechanical properties of concrete, of incorporating graphene as the nanosized building block to control the material behaviour and add novel properties and functionalities to concrete. The idea has been introduced in the scientific community around a decade ago, but the problem was always approached in the wrong way. Researchers focused on improving the cement properties only, which is just one of the four main constituents of concrete, and therefore none of the findings could have been directly applied to large scale applications, and consequently did not really have any impact on the industry.

OBJECTIVE AND SCOPE OF THIS RESEARCH

Recent advancements in cement and concrete science have started to implement nanomaterials as a fraction of weight to cement and mortar mixes, aiming to explore the resultant changes in microstructure[58;31;73;18]. This relatively new field of study has shown promising advancements, such as improvements in mechanical and barrier properties of cement, however there is long road ahead before it can be utilised in real practice. This is due to the very expensive nature of nanomaterials, the complicated multiple-step process of producing and most importantly – the

inability to scale these mixing techniques to concrete manufacturing.

Among all nanomaterials, I chose to use graphene as nanoreinforcement for concrete. Graphene was first demonstrated experimentally in 2004 by Prof Novoselov and Prof Geim[55] by mechanical exfoliation of bulk graphite. Graphene is a single atomic layer of graphite; an abundant mineral which is an allotrope of carbon that is made up of very tightly bonded carbon atoms organised into a hexagonal lattice. This nanomaterial is quite special because it has very thin atomic thickness (of $0.345Nm$) and very strong covalent bonds. These properties are what enable graphene to break so many records in terms of strength, electricity and heat conduction (as well as many others). There are two particularly important ones for this thesis – firstly, graphene's inherent mechanical strength. Due to the strength of its $0.142Nm$-long carbon bonds, it is the strongest material ever discovered, with an ultimate tensile strength of 130,000,000,000 Pa (or 130 GPa), compared to 400,000,000 Pa for A36 structural steel, or 375,700,000 Pa for Kevlar[3]. And secondly, graphene's unique ability to retain its initial size after strain, both make this material very suitable for mixing with concrete and hydration crystals of cement.

In the following decade the scientific community developed various alternatives to mechanical separation for synthesising graphene sheets (layers) such as Chemical Vapour Deposition[14], chemical derivation from graphite oxide[8] and exfoliation in water[48;49;62]. The latter method gives the opportunity to break down bulk graphite powder into atomically thin graphene layers, floating freely in aqueous environment. This turned out, as my thesis presents later on in each chapter, to be extremely efficient for large scale production and particularly for concrete mixing. My doctorate thesis explores the fundamental properties of concrete using liquid-exfoliated graphene as reinforcement on the nanoscale level. The goal is to show how this novel, nanoengineered concrete can benefit from reduced amount of cement while keeping its mechanical performance to a very high level.

The novelty of this work lies in the unprecedented increase in mechanical performance of

concrete, which technically speaking, is a different composite material from cement. These include an increase of up to 146% in the compressive strength, up to 79.5% in the flexural one and a decrease in the maximum displacement due to compressive loading by 78%. At the same time we find an enhanced electrical and thermal performance, with 88% increase in heat capacity. The list of staggering properties demonstrated also includes a decrease in water permeability by nearly 400% compared to the standard concrete, making the graphene-concrete composite material uniquely suitable for constructions in areas subject to flooding. None of these properties have been reported before. Moreover, we have demonstrated for the first time a truly scalable method for preparing concrete, mixed with water-based graphene that can be directly used in industry.

This research work, entitled "Fundamental Physical Properties of Graphene Reinforced Concrete ", aims to bridge the gap between pioneering work on novel nanomaterials and traditional construction materials, or more broadly speaking – between physics, materials science and structural engineering. The experimental work was carried out at the Centre for Graphene Science, part of the Engineering department at the University of Exeter. It is generally split into two main parts – exfoliation and preparation of water-based graphene suspensions and testing fundamental mechanical properties of concrete, including compressive and flexural strength, nonlinear fracture mechanics, electrical conductivity and water impermeability.

The objective of this research was twofold. First, to experimentally demonstrate that graphene can be dispersed in water-based environment and that the method used does not introduce any defects to the graphene sheets. Also, to show that this method is highly scalable and particularly useful for concrete mixing. Second, to perform large number of tests on concrete samples, comparing tap water experimental groups with concrete, benefiting from various concentrations of water-based graphene suspensions. These experiments included standard compressive and flexural strength testing, followed by a more in-depth study on nonlinear fracture parameters for crack propagation and growth in concrete beams, samples with steel electrodes to study the electrical

and thermal conductivity properties of graphene reinforced concrete and lastly, testing the water impermeability of the enhanced construction material. In addition, statistical studies were performed both for the graphene solutions characterizations and for the compressive strength of concrete at early and late stage of strengthening.

OUTLINE OF THIS THESIS

In short, the main sections of this thesis will be outlined. The first part will present the structure of unhydrated cement, the hydration reaction in details, and will outline the difference between cement and concrete in their mechanical performance. This is an important differentiation as previous studies have largely focused on the incorporation of nanomaterials in cement. However, these findings do not extend directly to concrete, as the addition of the other elements of concrete such as sand and aggregate changes the physico-mechanical behaviour of the material. The second part of the theoretical background will explore the structure of graphene, followed by a discussion of various exfoliation methods. In addition, relevant literature on the topic will be discussed.

After in-depth theoretical analysis in Chapter 2, Chapter 3 will discuss the details of all experiments performed. Similarly to the overall structure of this thesis, firstly graphene characterisation methods will be covered and then all experimental techniques used for studying the concrete mechanical properties, including transport and water impermeability.

The core of this thesis, will consist of five chapters and will present all novel results from the experimental work. Chapter 4 will show a systematic study on the liquid-exfoliation of graphene, followed by extensive analysis of the number of graphene layers in flakes and the nature of their defects. Both exfoliation from graphite and 3 different industrial grade graphene powders will be discussed. Chapter 5 will explore the fundamental properties of concrete, enhanced with various graphene concentrations. The results will show the evolution of compressive strength as a time-

dependent process, followed by a statistical study of early age strength. Results on cycling loading, plastic strain and flexural loading will also be discussed in detail.

Chapter 6 will show a systematic analysis of the nonlinear fracture mechanics (NFM) of the graphene reinforced concrete. Two analytical approaches, based on NFM principles, will be applied and they will evaluate important parameters relating the formation and propagation of cracks. The following chapter 7 will explore properties of cement-based composites, reinforced with graphene, beyond the classic compressive and flexural strength. These include studies on electrical conductivity and heat transfer on cement and concrete samples, as well as water permeability in cylinders. The final chapter 8 of the results section will present X-Ray diffraction (XRD) analysis of the hydration crystals of cement. The aim will be to identify the changes in microstructure due to graphene reinforcement at the earliest stages of hydration.

Chapter 9 will present the discussion and conclusions, by summarizing the main results and reflecting on the logical overall presentation. Recommendations for future work will be outlined, as this work is the stepping stone for a much larger and longer interdisciplinary scientific research.

2

THEORETICAL BACKGROUND

INTRODUCTION

In order to fully understand how graphene, a nano-scale material, could enhance the crystals of cement and contribute to unprecedented increase in the mechanical performance of concrete, all theoretical concepts for both materials will be presented in detail in this chapter. In addition, relevant background work on the topic will be presented and analysed.

The first main section will outline the process of cement manufacturing, the importance of the hydration reaction and the consequent hydrated cement crystals. This will be followed by description of the importance of capillary voids and air entrapment during mixing and setting of concrete. Finally, concrete's mechanical performance will be discussed along with the fundamental relationship between the water/cement ratio and concrete's strength.

The second main section of this chapter will explain the atomic structure of graphene and its remarkable mechanical properties. It will also compare different methods for producing graphene and comment on their benefits and drawbacks. This analysis is important to clearly identify the most suitable method for mixing the nanomaterial with concrete on a large scale.

REVIEW ON NANOTECHNOLOGY AND CONCRETE

Before outlining the main theoretical concepts in this chapter, it is much needed to give the reader a broader overview of the research topic/problem investigated and its relevant background work. The concept of applying nanotechnology to cement and concrete has emerged in the past decade, showing consistent and similar conclusions from various authors and groups. They outline that nanomaterials do enhance the structural stability, fracture toughness and overall strength of cement, but without much success in finding ways to scale the work and prepare it for industrial purposes. Only when put on large scale, the benefits of various nanoengineered concrete will have true positive impact on the environment by decreasing the overall carbon emissions.

Nanotechnology was first introduced by Richard Feynman in 1959[25] and since then there have been many revolutionary developments in various fundamental sciences as mentioned earlier. This new branch of science is composed of two main approaches: (i) the "topdown" approach, in which larger structures are reduced in size to the nanoscale while maintaining their original properties without atomic-level control or deconstructed from larger structures into their smaller composite parts and (ii) the "bottom-up" approach, also called "molecular nanotechnology" where materials are engineered from atoms or molecular components through a process of assembly or self-assembly[70].

Definition of nanotechnology in concrete

The nanoscience and nano-engineering, sometimes called nanomodification, of concrete are terms that have come into common usage and describe two main avenues of application of nanotechnology in concrete research[72;70]. Nanoscience deals with the measurement and characterization of the nano and microscale structure of cement-based materials to better understand how this structure affects macroscale properties and performance through the use of advanced characterization techniques

and atomistic or molecular level modeling.

Nanoengineering encompasses the techniques of manipulation of the structure at the nanometer scale to develop a new generation of tailored, multifunctional, cementitious composites with superior mechanical performance and durability potentially having a range of novel properties such as: low electrical resistivity, self-sensing capabilities, self-cleaning, high ductility, and reduction of cracks[70]. Concrete can be nanoengineered by the incorporation of nanosized building blocks or objects (e.g., nanoparticles and nanotubes) to control material behavior and add novel properties, or by the grafting of molecules onto cement particles, cement phases, aggregates, and additives surface functionality, which can be adjusted to promote specific interfacial interactions[70].

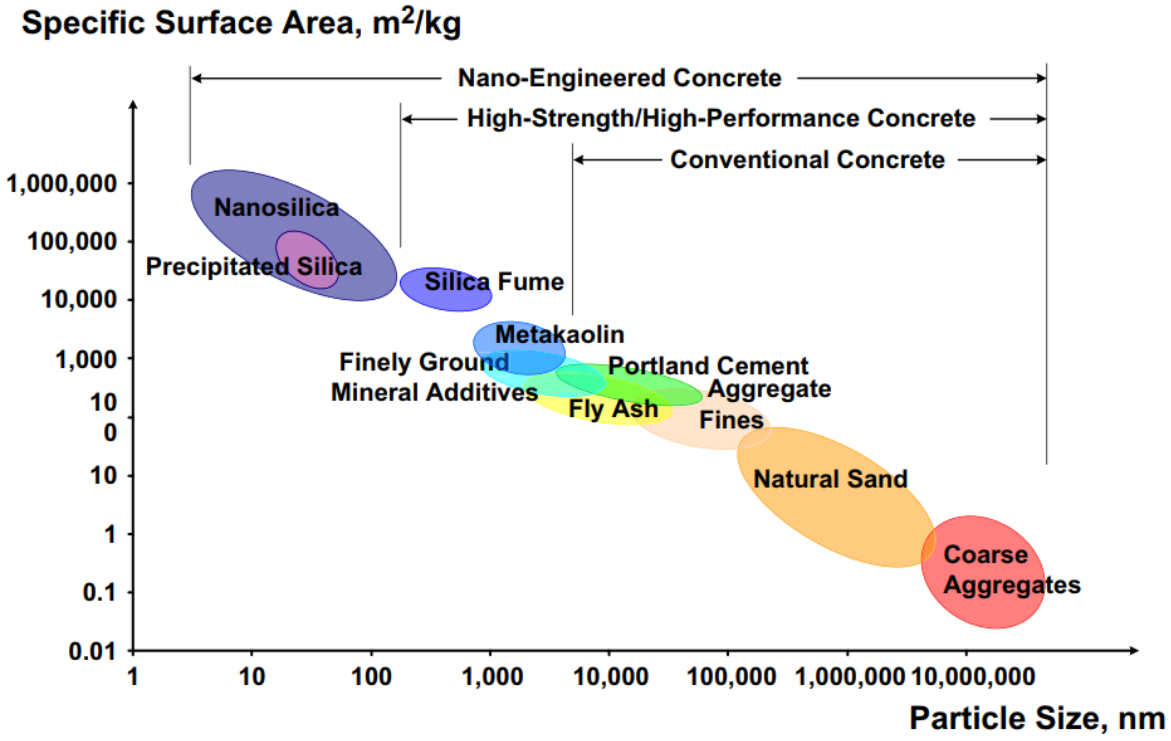

Figure 2.1: Particle size and specific surface area related to concrete materials. Adopted from[77].

Nano-engineering, or nanomodification, of cement is a quickly emerging field[77]. Synthesis

and assembly of materials in the nanometer scale range offer the possibility for the development of new cement additives such as novel superplasticizers, nanoparticles, or nanoreinforcements. Methodologies for hybridization and grafting of molecules allow for the direct manipulation of the fundamental structure of cement phases[70]. These techniques can be used effectively in a bottom-up approach to control concrete properties, performance, and degradation processes for a superior concrete and to provide the material with new functions and smart properties not currently available[70]. Engineering concrete at the nanoscale can take place in one or more of three locations[77]: in the solid phases, in the liquid phase, and at interfaces, including liquid–solid and solid–solid interfaces.

While nano-engineering of cement-based materials is seen as having tremendous potential, nonetheless, several challenges will need to be solved to realize its full potential, including the proper dispersion of the nanoscale additives, scale-up of laboratory results and implementation on larger scale, and a lowering of the cost benefit ratio. The goal of this work is to explore the effect of the addition of graphene to concrete and cement and to analyse the consequent nanomodifications to the hydration crystals of cement.

CONCRETE

Concrete is a composite material made of sand (fine) and stones (coarse) (aggregates), glued together by the chemical reaction between cement and water. This section will explore the microelement composition of Ordinary Portland Cement (OPC) which is used for this research, and the chemical transformation that it undergoes when water molecules are introduced.

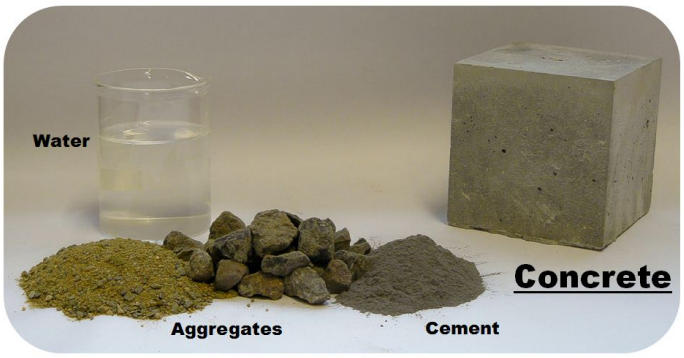

Figure 2.2: Concrete constituents – water fine and coarse aggregates, cement and a cube sample used for standard strength testing, adopted from[1].

Whilst this reaction, technically known as hydration reaction, is fairly straightforward, it produces very large group of various fibrous crystals. Richardson[68;67] summarized them in 5 general groups, and also identified more than 70 different variations of these crystals. Fig.2.2 shows the concrete constituents and a hardened concrete sample in cube form. When OPC reacts with water, it transforms from powder to gel, then to solid, which allows it to glue the fine and coarse aggregate to form concrete. There is common misunderstanding that the mechanical properties of OPC can be directly translated to concrete, this assumption is scientifically wrong for multiple reasons which will be discussed below. The mechanical behaviour, and more importantly the formation and propagation of cracks in OPC, are much different in concrete due to the slipping of planes between cement and aggregates, as well as the air voids, entrapped during mixing and setting[57]. Therefore, even though very similar tests are performed to study the common fracture properties of OPC and concrete, the fundamental mechanical behaviour is different and should be considered separately.

Chemical reactions of Portland Cement and its unhydrated constituents

Portland cement is prepared by igniting a mixture of raw materials, one of which is mainly composed of calcium carbonate an the other of aluminum silicates. The most typical materials are limestone and clay, both of which naturally occur in a great number of varieties[43]. The process of cement manufacture consists in the incorporation of the raw materials to form a homogeneous mixture, the burning of the mix in a kiln to form a clinker, and the grinding of the clinker with the addition of a small proportion of gypsum to a fine powder[43]. Two processes, known as the dry and wet processes according as to whether the raw materials are ground and mixed in wet/dry condition, are used. The difference between them lies in the nature of the materials mixed initially, but ultimately the last stage where the cement is burn is the same. This burning happens in a rotary kiln at 1300-1500∘ which is a long cylinder rotating on its axis and inclined so that the materials fed in at the upper end travel slowly to the lower end[43]. Upon burning, the water is driven off as steam and then as the raw materials descend down the kiln, they undergo a series of reactions, forming granular masses known as clinker. The final step in cement production is cooling down and adding gypsum to control the setting.

The compounds present in cements are formed by the interaction during burning of the lime, silica, alumina and ferric oxide which are the bulk constituents, together with various minor components such as magnesia and alkalis[43]. First, the major individual components are discussed, followed by the compounds that form between them. **Calcium Oxide** (CaO) or lime, is an essential component of all cements and is derived from the decomposition of calcium carbonate ($CaCO_3$). **Calcium hydroxide** ($Ca(OH)_2$) is the product of lime hydration within the kiln. **Magnesium oxide** (MgO) is also present in small quantities[43]. **Silicon dioxide** or silica, is the most abundant of all minerals and is a component of the vast group of silicates and clays. Various combinations are present in the cement clinker and all react with water to produce calcium silicate

hydrates which are mainly responsible for the strength and properties of concrete. Another two important minerals are **Aluminum oxide** and **Ferric oxide**.

The afore mentioned minerals form compounds which are quite famous in the community. Upon reaction with water they undergo physical transformation from powder to gel to solid, which will be discussed later in the chapter. Their initial composition is presented below:

Table 2.1: Main Compounds of unhydrated Portland Cement[54].

Name of compound	*Oxide composition*	*Abbreviation*
Tricalcium silicate	$3CaO.SiO_2$	C_3S
Dicalcium silicate	$2CaO.SiO_2$	C_2S
Tricalcium aluminate	$3CaO.Al_2O_3$	C_3A
Tetracalcium aluminoferrite	$4CaO.Al_2O_3.Fe_2O_3$	C_4AF

There are few other minor compounds such as MgO, TiO_2, Mn_2O_3, K_2O and Na_2O and they account for just a few percent of the total mass. The K_2O and Na_2O are referred to as *alkalis* and can affect the strength and durability of concrete because of the famous alkali-silica reaction (ASR).

Hydration mechanisms of Portland Cement

The reactions by virtue of which unhydrated cement becomes a bonding agent happen when water is added to the concrete mixture and comes in contact with cement crystals. In the presence of water, the silicates and aluminates listed in Table 2.1 grow and evolve with time, they change shape and progressively form a firm and hard mass, commonly referred to as hydrated cement paste. There are two ways for the afore mentioned reaction to happen – true hydration and hydrolysis. In almost all cases though hydration reaction is used for either. Both C_3S and C_2S

are equally important for cement hardening and they are the main contributors for strength and durability. The complete hydration of each compound will be presented in the following section.

The process of complete cement hydration takes considerable amount of time because the crystals have relatively low solubility in water[54]. When the water comes in immediate contact with the unhydrated cement it forms colloidal grains which grow in size over time. However, there are numerous particles left without any contact with water at first and it then becomes hard for them to cross the surrounding envelope in order to hydrate. One possible way for achieving this is that the dissolved silicates precipitate as an outer layer or alternatively, they bond with already hydrated particles after saturation has been reached[54]. Either way, the hydration process is slowed down and even after long periods of time there remains an appreciable amount of unhydrated cement[54]. For example, according to some studies cement crystals have been found to have hydrated to a depth of only 4 μmm after 28 days of hydrations and 8 μmm after an year.

Generally, all various compounds in cement are intermixed during the hydration process. The main hydrates can be classified as calcium silicate hydrates, which form the calcium-silicate-hydrate gel (C-S-H gel) and tricalcium aluminate hydrate. The tetracalcium aluminoferitte (C_4AF) probably hydrates into tricalcium aluminate and an amorphous phase $CaO.Fe_2O_3$[54]. This hydration process, despite the type of compound, can be studied by various methods which is not the in the scope of this research work. Studies have shown that the rates of hydration of C_3S and C_2S in a pure state differ, as shown in Fig.2.3 :

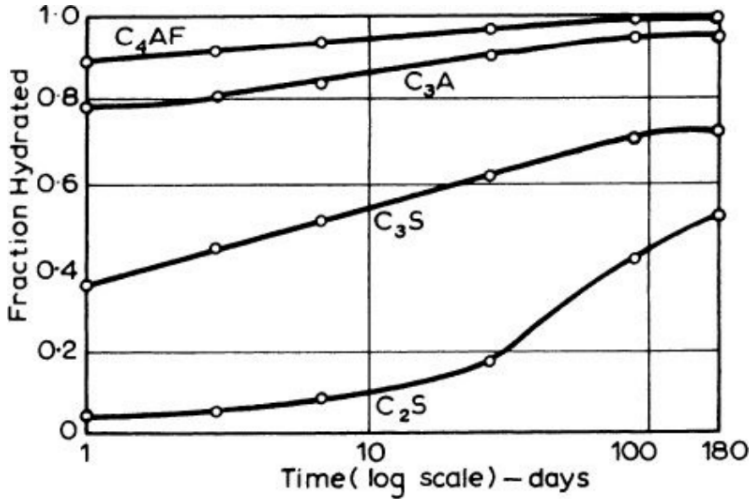

Figure 2.3: Evolution of hydration of the main compounds of cement, adopted from[54].

Fig.2.3 shows that the aluminoferrites hydrate quicker than silicates, which implies that they are responsible for setting properties of concrete, while the C_2S and C_3S contribute to the overall strength and ductility. When hydration takes place C_3S undergoes hydrolysis, producing calcium silicate of lower basicity[54] – $C_3S_2H_3$ and releases lime ($Ca(OH)_2$). The problem of lime leaching, or 'bleeding', is serious for concrete long-term durability because when the lime is being washed away it leaves numerous pores and empty air spaces, which obviously has a negative impact on the mechanical performance of the material. Not all calcium silicates hydrate fully – some C_3S and C_2S remain impure. These are called *alite* and *belite* respectively and are a product of trapped oxygen in the clinker during cement manufacturing[54].

Now lets discuss the chemical reactions that happen during hydration in more detail. Broadly speaking, when water comes in contact with cement compounds, they react and cement crystals change shape and size. Firstly, the tricalcium aluminate (C_3A) reacts with gypsum in a exothermic reaction to produce ettringite:

$$C_3A + 3CSH_2 + 26H \rightarrow C_6AS_3H_{32} + \Delta H$$

The ettringite crystals do not contribute to the mechanical strength and thus to the gluing properties of cement paste. Once all gypsum is used, the ettringite becomes unstable and reacts with tricalcium aluminate to for monosulfate aluminate crystals:

$$2C_3A + 3C_6AS_3H_{32} + 22H \rightarrow 3C_4ASH_{18}$$

The C_3S and C_2S react with water to produce numerous calcium silicate hydrates, lime and heat:

$$2C_3S + 6H \rightarrow C_3S_2H_3 + 3CH + \Delta H$$

C_3S_2H is used as a short-hand notation for a large group of chemical elements, comprising the calcium silicate hydrates family. Richardson[68;67] did an extensive analysis of the nature of hydration products in cement pastes and concluded that there are more than 60 different phases of C-S-H gel. It is beyond the scope of this research to analyse the Ca:Si ratio, responsible for crystal variations, but further work can investigate the relationship between graphene and tobermorite, jaffeite and jennite crystals[68], as they are the major groups (weight-based %).

The important conclusion form this section is to show cement compounds and their chemical transformation upon reacting with water. Their growth and interlocking contribute to the mechanical properties of all cement-based materials. It is worth noting that at this stage of research it is almost impossible to provide a certain proof of graphene-cement chemical bond. Any work which claims[76;58;31;73;18] that has evidence for this bond clearly has not fully studied the C-S-H gel family of crystals. The alternative in providing evidence for the graphene reinforcement is

through extensive statistical study of the core mechanical properties of concrete.

Capillary pores and degree of porosity

It can be noted that at any stage of hydration the capillary pores represent that part of the gross volume which has not been filled by the products of hydration. Consequently the capillary porosity of the paste depends both on the water/cement ratio of the mix and on the degree of hydration[54] and its volume is decreased with the progress of hydration. According to studies[54] the size of the pores rarely exceed $1\mu m$ and majority being less than $200nm$ in area. They vary in shape and form an interconnected system randomly distributed throughout the cement paste. The interconnected capillary pores are responsible for the permeability of the haredned cement paste and for its vulnerability to cycles of freezing and thawing[54].

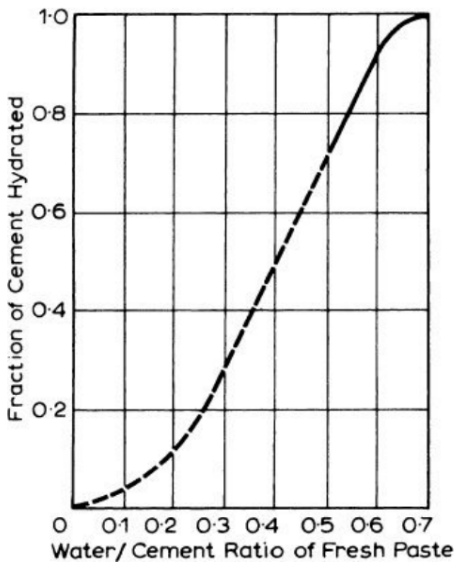

Figure 2.4: Relationship between the potential volume of capillary pores, expressed as fraction of hydrated cement, and the increasing water/cement ratio, adopted from[54].

It is of great importance for this research work to get a better understanding of the capillary pores within the hydrated cement matrix. This is because the main hypothesis is that

the addition of graphene dispersions decreases the gross % of empty space within the composite cement/concrete paste and this leads to overall increase in mechanical strength. Following the explanation from the previous section, it can be seen that at any stage of hydration there are multiple cement grains which are not yet fully hydrated and therefore empty space in between is left. This naturally occurring phenomena, or capillary porosity, is directly responsible for mechanical properties and fracture mechanisms of cement-based composites It has been studied that there is linear dependence between the fraction of hydrated cement and water/cement ratio[54]. This relationship is shown on Fig.2.4 and might seem intuitive, but should not be underestimated.

The greater the water/cement ratio is, the sloppier the concrete mix becomes and this is unfavourable for industrial purposes. So the challenge arises – one needs to find a way to maximise the cement hydration whilst keeping the water/cement ratio as low as possible. Plasticisers are widely used in practice as a solution to this and other problems during concrete setting and hardening[6]. Generally their chemical structure is based on nonionic surfactants, carbohydrates and lignosulphonates[6]. They can improve not only workability but also reduce segregation and bleeding. However, there are serious consequences if proportions are not kept strict. Yet this is another reason why introducing nanomaterials to the chemical composition of cement can be beneficial – it can exclude the addition of admixtures and accelerators[13;90].

The composite structure of Concrete and it's mechanical behaviour

Strength of concrete is commonly considered its most valuable property, although, in many practical cases, other characteristics, such as durability and permeability, may in fact be more important[54]. Nevertheless, strength usually gives an overall picture of the quality of concrete because strength is directly related to the structure of the hydrated cement paste. Moreover, the strength of concrete is almost invariably a vital element of structural design and is specified for compliance purposes[54]. In engineering practice, the strength of concrete at a given age and cured in water at

a prescribed temperature is assumed to depend primarily on two factors only: the water/cement ratio and the degree of compaction. The influence of air voids on strength was discussed earlier in this chapter, and at this stage fully-compacted concrete only is considered: for mix proportioning purposes, this is taken to mean that the hardened concrete contains about 1 per cent of air voids. When concrete is fully compacted, its strength is taken to be inversely proportional to the water/ cement ratio[54]. The Duff Abrams's law states that[54] strength to be equal to:

$$f_c = \frac{K_1}{K_2^{w/c}}$$

where w/c represents the water/cement ratio of the mix (originally taken by volume), and K1 and K2 are empirical constants. The general form of the strength versus water/cement ratio curve is shown in Fig.2.5.

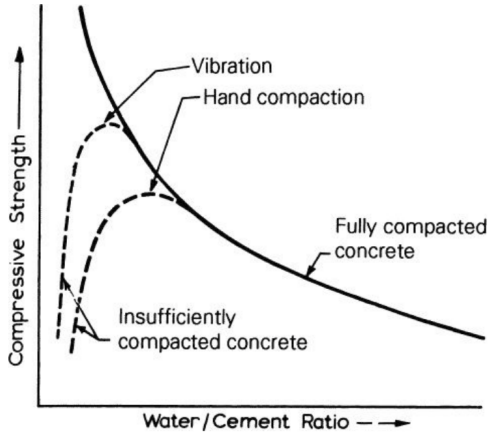

Figure 2.5: The relation between strength and water/cement ratio of concrete, adopted from[54].

Abrams' rule, although established independently, is similar to a general rule formulated by René Féret in 1896 in that they both relate strength of concrete to the volumes of water and cement. Féret's rule was in the form[54]:

$$f_c = K \left(\frac{c}{c + w + a} \right)^2$$

where f_c is the strength of concrete, c, w and a are the absolute volumetric proportions of cement, water, and air, respectively, and K is a constant. The water/cement ratio and the degree of compaction both affect the volume of voids in concrete, and this is why the volume of air in concrete is included in Féret's expression[54]. The relation between strength and volume of voids is important to the graphene reinforcement analysis as discussed earlier this chapter. Fig2.5 shows that the range of the validity of the water/cement ratio rule is limited. At very low values of the water/ cement ratio, the curve ceases to be followed when full compaction is no longer possible; the actual position of the point of departure depends on the means of compaction available[54]. It seems also that mixes with a very low water/cement ratio and an extremely high cement content exhibit retrogression of strength when large-size aggregate is used[54]. This behaviour may be due to stresses induced by shrinkage during hardening, whose restraint by aggregate particles causes cracking of the cement paste or a loss of the cement–aggregate bond[54]. Following this discusison and analysis of the importance of the w/c ratio the following 4 parameters were taken into account prior to preparing the experimental procedure:

1. Ratio of cement to mixing water

2. Ratio of cement to aggregate

3. Grading, surface texture, shape, strength, and stiffness of aggregate particles

4. Maximum size of the aggregate

GRAPHENE

Structure

In 2004 Novoselov and Geim introduced[55] for the first time experimental proof of the idea behind decomposing bulk graphite into thin layers. They used the scotch tape exfoliation method, which demonstrates that after multiple repeatable steps, one can reduce the structure of graphite to few-layer graphene flake. The schematics on Fig.2.6i and Fig.2.6ii illustrate this method. The graphite powder is composed of hundreds of identical layers of carbon atoms arranged in a hexagonal, honeycomb lattice, which are vertically stacked. The layers are easily separated due to the weak Van der Waals forces holding the carbon atoms in the Z-plane. Fig.2.6iii. shows the schematic of a single layer graphene. It can be defined as a single layer of carbon atoms held together by strong covalent bonds[39]. The multifunctionalities of one graphene layer include high thermal conductivity (in the order of $5000 W/mK$), high electron mobility (250,000 $\frac{cm^2}{V}$) and large surface area ($2630 \frac{m^2}{g}$). However, the intrinsic mechanical properties are most important for applications with composites. The sp^2 hybrid bonding of carbon atoms is responsible for very high elastic modulus (0.5-1 TPa)[85] and tensile strength (130 GPa)[90].

The two-dimensional structure, however, endows this material with inherent advantages over other more widely studied carbon allotrope such as carbon nanotubes (CNTs) and graphite. The 2D structure of graphene yields a higher specific surface area than either CNTs or graphite[90] thereby providing more area to interact with the matrix material, whether the interaction entails transfer of electrons, phonons or mechanical stresses. These properties are very attractive for the application of graphene as reinforcement for materials with any kind of matrix, regardless of its type polymer, ceramic, cement-based or other composite[90].

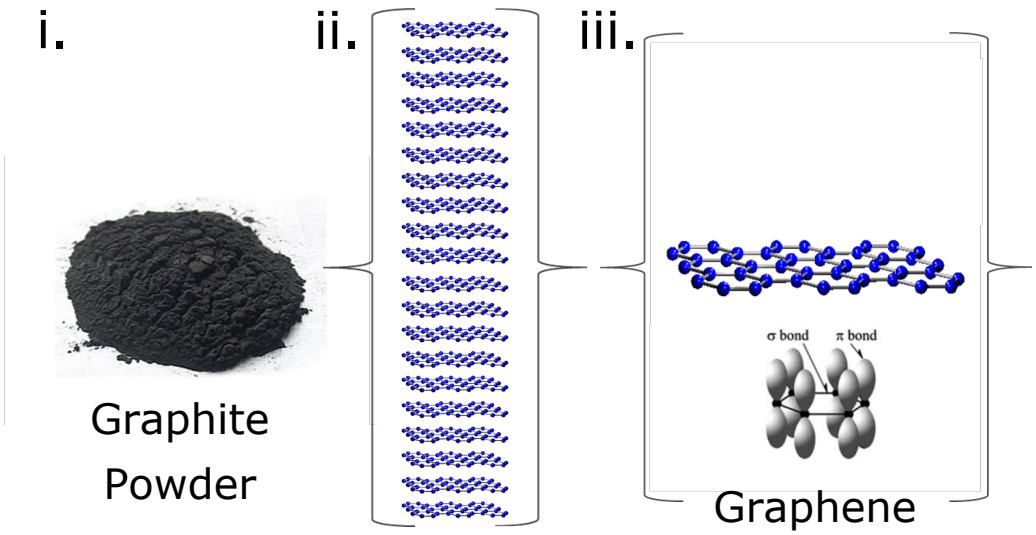

Figure 2.6: (**i.**) Photograph of standard graphite powder, supplied by Sigma Aldrich[4]. (**ii.**) Schematic presenting multilayered structure of graphite. Identical layers of carbon atoms stacked on top of each other and held together by Van der Waals forces. (**iii.**) Single atomic layer of carbon atoms, organised in hexagonal lattice. The black and white schematic introduces the σ and π bonds, adopted from[81].

The 2D structure of graphene is especially suitable for use in polymer and cement-based composites where processing techniques often employ turbulent and high speed mixing. The reported strength and ability to retain initial length after strain are result of the strong in-plane σ bonds which hold the atoms together, whilst the perpendicular π orbitals connect two layers in the Z-plane. These bonds are indicated on the black and white schematic on Fig.2.6iii. Also, the flat morphology of graphene is more defined to survive high pressure processing than the tubular structure of CNTs that makes them susceptible to buckling and fracture. Not surprisingly it was concluded that it is the strongest[39] among all other nanomaterials in the two dimensional materials group, including transition metal-dichalcogenides (TMDs, e.g., MoS_2), hexagonal boron-nitride (h-BN), and black phosphorous or phosphorene[20].

Mechanical properties of single layer graphene

The phase-transformation of cementitious hydration crystals is a time-dependent process which involves physical growth and mechanical interlocking, as it will be discussed in details later on this chapter. Therefore it is very important for a nanomaterial to have very strong intrinsic modulus of elasticity, in order to bridge the gaps between cement crystals and contribute to their overall strength. It has been demonstrated that graphene has very high tensile strength[39]. Lee and Hone *et al* used nanoindentation in atomic force microscopy (AFM) and demonstrated that when the force-displacement behaviour is interpreted within a framework of nonlinear elastic stress-strain response, it yields second- and third-order elastic stiffnesses of 350 N/m and -690 N/m respectively[39]. They stretched and deposited a monolayer graphene flake over many circular wells which formed a series of free-standing membranes. Then, the AFM used in this study probed the centre of each film as illustrated on Fig.2.7a. The tip of the AFM applied cyclic force on the atomic sheet to record data for the elastic properties (Fig.2.7b.) and then second experiment was performed until complete failure. The breaking strength was found to be 42 N/m which corresponds to a Young's modulus of 1 $\pm$ 0.1 TPa as shown on Fig.2.7c. , which therefore made graphene the strongest material ever measured. Later on in 2012 J. Lee *et. al* demonstrated that the Youngs Modulus of single graphene layer actually extends to 2.4 $\pm$ 0.4 TPa[32] and 2.0 $\pm$ 0.5 TPa for bilayer. The group measured strain induced by pressurised graphene balloons and estimated it from the G band using Raman Spectroscopy. The resulting numerical values were then compared to computational simulation and agreement was achieved[32]. M.L. Blees *et. al*[50] show that when the ratio between in-plane stiffness and out-of-plane bending stiffness is very high, the samples tested are more subjective to bending and crumpling than to stretch and shear[50].

Another important paper for this thesis is the work by G. Lopez-Pollin *et al* which reports a systematic study on the elastic modulus and fracture energy of graphene sheets, relating these

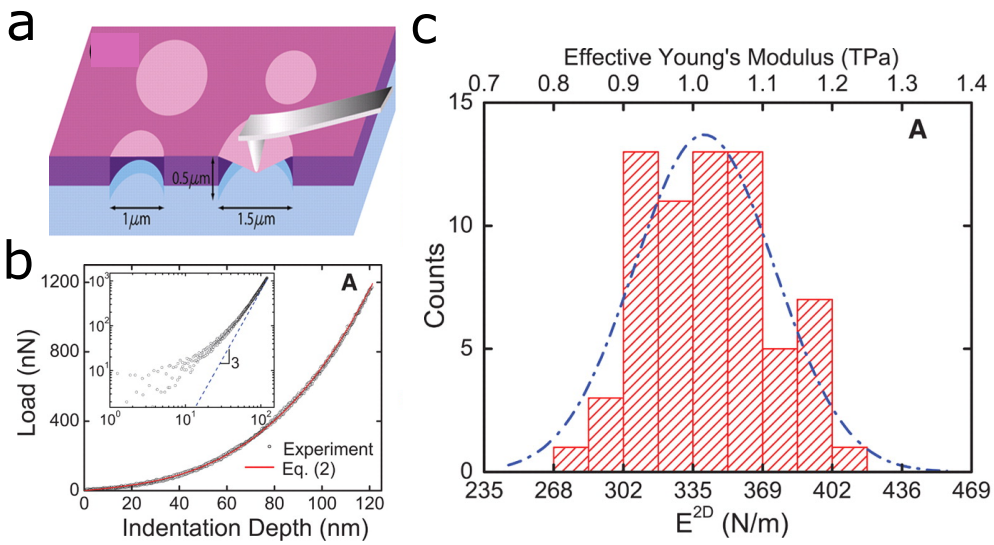

Figure 2.7: (**a**) Illustration of the nanoindentation setup in a suspended monolayer graphene membrane. (**b**) Loading/unloading curve with increasing indentation depth. (**c**) Histogram of elastic stiffness, adopted from[39].

properties to lattice defects. They show that both mechanical properties degrade as the defect density increases, which suggests that the quality of graphene, despite the method of exfoliation, should not introduce any basal plane defects because this will have a direct consequence on the growth of cement crystals.

Methods for graphene exfoliation

A lot of work has been dedicated to finding new ways of exfoliating graphene from graphite, since its first synthesis in 2004[55]. Each method is optimised for various purposes – quality of monolayer, scalability and quantity, oxidation, reduction of other functional groups etc. Selected publications which pioneered chemical vapour deposition (CVD)[14], electrochemical exfoliation[65], chemical reduction of graphene oxide[60], bottom up synthesis[34] and liquid-phase exfoliation[48;49;62].

Irrespective of the matrix material, one of the major factors driving the rapid pace of research on graphene reinforced structural composites is the availability of bulk quantities of high-quality

graphene. Its synthesis processes can be divided into two broad categories: (i) bottom up approaches such as chemical vapour deposition (CVD) processes and thermal epitaxial growth, and (ii) top down approaches including mechanical and chemical exfoliation of graphite. The vast majority of studies on graphene structural composites have utilised graphene synthesised by chemical or thermal exfoliation. Researchers have used different kind of CVD processes, namely thermal and plasma, to synthesise single to multilayer graphene (MLG). The thickness of graphene produced by these synthesis methods is a function of substrate type, cooling rate, gas flow rate, and other operating conditions; whereas the size of individual defect-free graphene islands depends primarily on the crystallographic orientation and grain size of the substrate material. CVD method generally produces graphene with very high purity, few (<10) layers, and near perfect structure and crystallographic orientation[80;10;52] High-purity MLG with larger lateral dimensions can be produced by utilising thermal epitaxial growth which utilises high temperatures (1250–1450°C[85]) to induce desorption of Si atoms in SiC, which effectively yields a hexagonal graphene structure[80].

Graphenic materials, containing between 10 and 100 layers, are most commonly utilised for structural composites. These graphenic materials have been referred to by number of names and the most widely accepted (technically correct) is graphene/graphite nanoplatelets (GNPs)[12]. These materials are synthesised by either mechanical exfoliation or chemical methods[61;17;36;74].

Mechanical exfoliation is the method used by Novoselov *et al.*[55] to isolate a single layer of graphene. The mechanical exfoliation process can be adopted through suitable automation to produce large quantities of very thin and chemically pure graphene structures. The crystallographic purity of the starting graphite structure ensures that the graphenic material produced retains high crystallinity. There are different types of chemical exfoliation methods, with the most common one being the exfoliation of graphene oxide (GO) and subsequent reduction to graphene. However, the reduction is often found to be incomplete and hence this product is more commonly known as reduced graphene oxide (rGO).

An easy and scalable approach for graphene preparation is the liquid-phase exfoliation of chemically functionalised graphite, such as graphite oxide or graphite intercalated compounds, which allows the separation of the bulk material into individual atomically thin layers in a liquid medium to produce graphene suspensions. However, there are several issues associated with the films deposited from such suspensions, especially those comprising graphene oxide (GO): they are insulating and need to be converted into reduced graphene oxide (rGO) through harsh chemical or thermal processes,which creates defects in the crystallographic structure of graphene, leading to poor electronic performance. Alternatively, pristine graphite can be directly exfoliated by various techniques such as ball or three-roll milling, sonication, and high-shear mixing to obtain graphene suspensions. Such suspensions are stabilised by using organic solvents, or surfactants to prevent reaggregation of the graphene flakes. In particular, graphite exfoliation by high-shear mixing leads to a significant improvement in the quality of graphene, when compared with other exfoliation methods, and allows the production of more than 100 litres per hour of defect-free graphene water-based suspension.

Researchers have also tried to directly exfoliate graphite chemically via dispersal in an organic liquid solvent. The large organic liquid molecules are forced between the layers of graphite via ultrasonication; this intercalation process promotes the exfoliation of graphene layers. Removing these large molecules from the graphene structure, however, remains a challenge[45]. These synthesis routes also do not have significant control over the size, layer content and crystallographic purity of the product. Their large scale industrial viability, however, makes them attractive options as compared to mechanical exfoliation methods that are ideally suited for small batch processes.

The advantages and the drawbacks of each method have been summarized in a recent progress article by Raccichini *et al.*[65]. The authors also evaluated different graphene production methods in terms of the most important aspects of the graphene produced (quality and purity) and of each method (scalability, cost and yield). Their results are presented in Fig2.8 and it is clear

that each method presents different characteristics in terms of the output[65]. For example, the reduction of graphene oxide which is used extensively in the literature exhibits very high yield and possibilities for scalability; however the quality and purity of the material produced is quite low. Moreover, some liquid-phase exfoliation processes have both very high yield[62], produce high quality graphene, and can be readily scaled up.

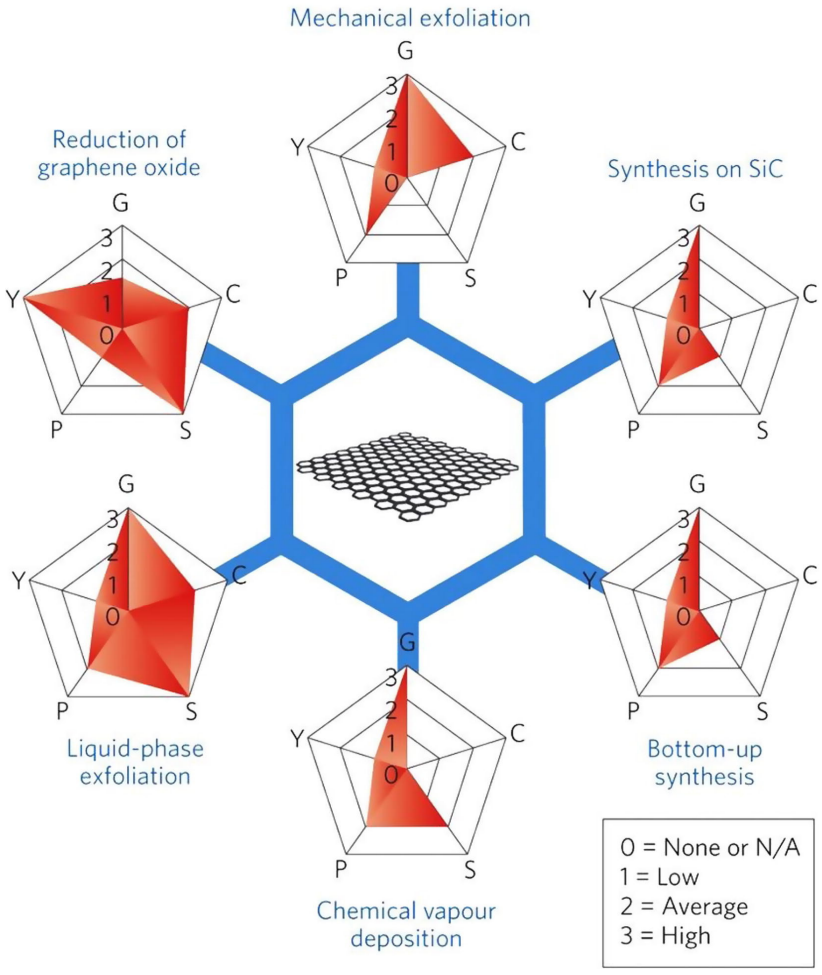

Figure 2.8: The key characteristics of the most common graphene production methods in a scale of 0–3; (G) refers to the graphene quality, (C) refers to the cost of production (low value corresponds to high cost of production), (S) refers to the scalability, (P) refers to the purity and (Y) refers to the yield of each preparation route, adopted from[65].

This thesis is mostly interested in the liquid-phase exfoliation of graphene. There are two methods – (i) using sonication principles[48] and (ii) high-shear turbulent mixing[62]. Both methods share the same mechanism – graphite powder is introduced to aqueous environment and dispersed with the help of stabilising agent, in this case the surfactant sodium cholate. Method (i) uses first principles of sonication waves to break apart the bulk structure of graphite whilst (ii) uses high-shear turbulent forces to achieve the same. In both cases the surfactant, which will be further discussed in Chapter 3, bridges the hydrophobic carbon atoms with water molecules, allowing the graphene sheets to float freely without restacking. The liquid exfoliation method turns out to be particularly useful for applications in composite materials, due to its scalability (more than $100L/h$) and yield of high-quality graphene. This method of mechanical exfoliation in water does not introduce any defects to the sheets, which preserves their intrinsic properties, as it will be demonstrated in later chapters.

3

EXPERIMENTAL PROCEDURE

INTRODUCTION

This chapter presents experimental details of the thesis. It will be divided in two - the first section will discuss preparation and characterisation of Functionalised graphene (FG) and Industrial Grade 3 graphene (IG) flakes using the liquid phase exfoliation method and the thin film transfer technique. This will include both ultrasonication and high-shear blending. This will be followed by introducing Raman Spectroscopy as a tool for assessing the number of layers and level of defects in thin graphene films. Next, the Scanning Electron Microscopy section shows the image analysis technique used for estimating size and area of various graphene flakes.

The second and third sections in this chapter will present the preparation of all concrete samples – cubes, beams, cement prisms and cubes for electrical conductivity properties as well as X-Ray Diffractometer measurements. They will also show the experimental apparatuses used in concrete testing and cement conductivity properties. All sections include one representative data measurement obtained from preliminary results to illustrate the output of each machine used for testing.

LIQUID-PHASE EXFOLIATION OF GRAPHENE

Ultrasonication and High-shear Blending

Ultrasonication

While much interesting work has been carried out on micromechanically cleaved graphene, for many applications it is necessary to develop high-yield, high throughput processing methods. Pioneering work in this area has been carried out by Ruoff *et al*, who have demonstrated large-scale exfoliation of graphene oxide (GO). This material is prepared by acid-treating graphite and consists of graphene sheets decorated with epoxides, carboxyl, and hydroxyl groups. GO is highly exfoliated and very stable when dispersed in aqueous environments. Such dispersions are very useful as they facilitate both materials processing and fundamental characterization.

However, GO is not ideal and suffers from some important drawbacks. Because of the presence of oxides, GO is a poor electrical conductor. While the oxides can be removed by reduction,5,11,12 this adds yet another step in the processing procedure. A bigger problem is that reduction cannot remove the many structural defects introduced by the oxidation process. These defects disrupt the band structure.

In order to address these issues and avoid using GO, this work focused on a method which produces pristine graphene from graphite, using the surfactant sodium cholate as stabiliser. Surfactant exfoliation is of particular importance as it can be achieved in aqueous environments. In order to gain full advantage from dispersions of pristine graphene using surfactants, it will be critical to increase the maximum concentration obtainable while maintaining the quality of the graphene flakes.

Fig.3.1a shows a schematic of ultrasonication bath used for graphene exfoliation. The black arrows represent the sonic waves, emitted from both sides, while in the cylinder in the middle is

a glass beaker full of water. Various concentrations of graphite powder (GP) and sodium cholate powder (SCP) were left in the beaker for $24h$ of constant sonication.

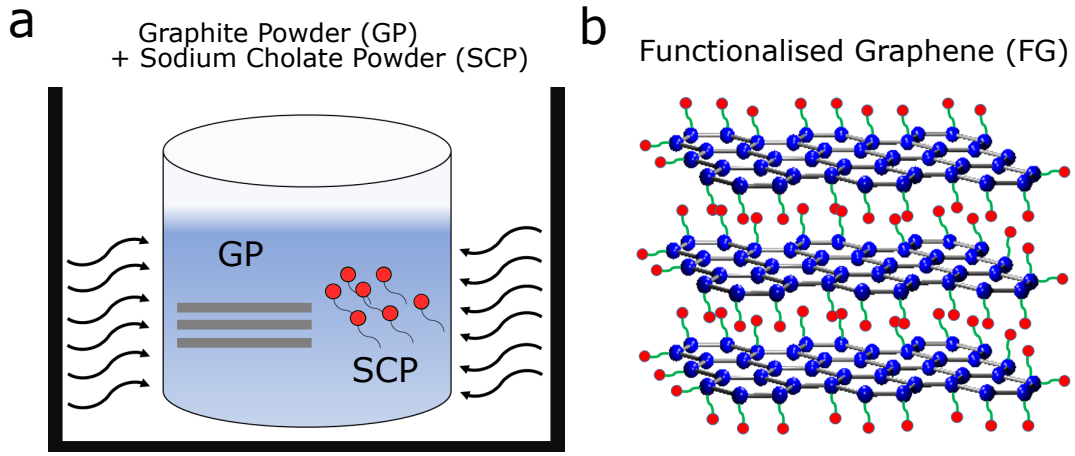

Figure 3.1: (**a.**) Schematic of a beaker, placed inside a sonication bath. The beaker contains graphite powder, sodium cholate and tap water. The black arrows indicate the sonication waves used for breaking down the graphite layers. (**b.**) Schematic of surfactant-stabilised graphene dispersion, also referred to as Functionalised graphene (FG). The hydrophobic tails of the surfactant are attached to the carbon atoms and the hydrophilic head attached to the water molecules.

The schematic on Fig.3.1b shows the final result – GP is broken down into thin graphene layers, which are surrounded by SCP molecules. The hydrophobic tail of SCP attaches to the carbon atoms whilst the hydrophilic head to the water molecules. Interestingly, the analysis in Chapter 4 shows that the SCP does not show any representative peaks in the raman spectra analysis. Another analysis shows that it does not introduce any basal plane or edge defects to the graphene sheet, so therefore SCP functionilisation should not be compared to oxidation or intercalation with ferric chloride.

Fig.3.2a shows a photograph of a beaker after $24h$ of sonication. The grey color that dominates the liquid suggests the uniform, high-yield dispersion of Functionalised graphene (FG) flakes. The black sediment at the bottom however, is a sign of much left over material which needs further processing with centrifugation machine. Fig.3.2 compares water-based FG which has

not been centrifuged (red) and one that has been centrifuged for $1h$ at $5000rpm$ (blue). This comparison shows that the ultrasonication method is useful for obtaining high-quality few-layer FG suspensions, however it is not very suitable for concrete mixing due to multiple steps involved and the inability to scale it up quickly and effectively.

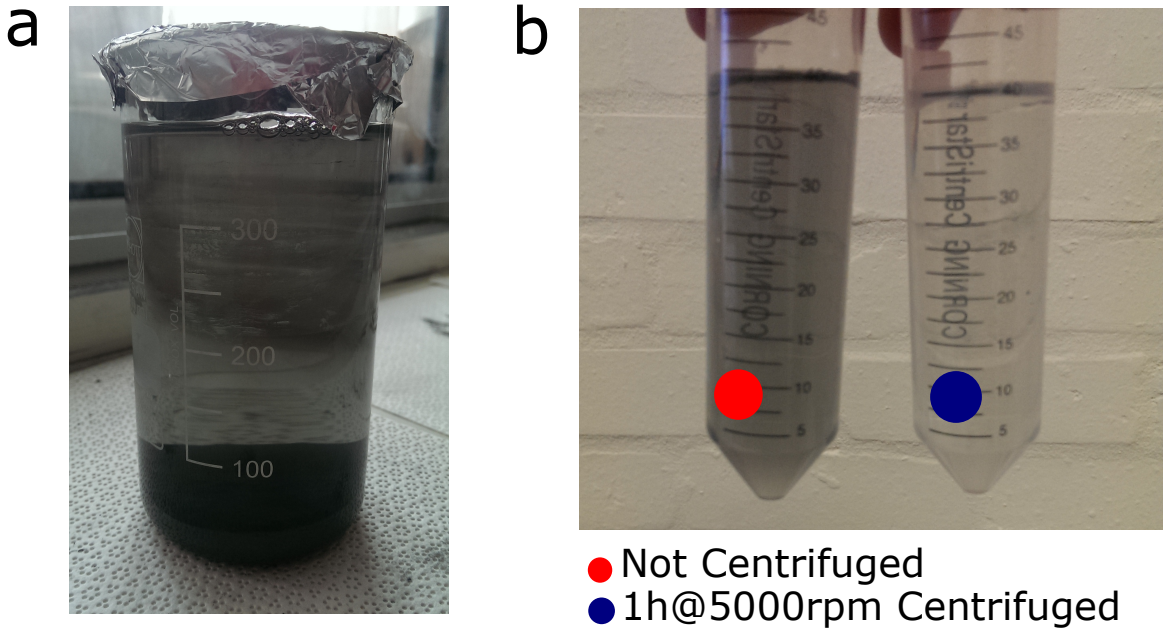

Figure 3.2: (**a.**) Photograph of FG solution produced from $24h$ of sonication. It is sealed to limit evaporation due to heating and it is evident that the exfoliation process is far from perfect – containing sediment on the bottom. Photograph (**b.**) shows the effect of centrifugation on the transparency of a solution.

High-shear blending of Functionalised Graphene

After the successful demonstration of surfactant-stabilised FG dispersions using the sonication method, this work focused on new method for achieving the same high-yield, defect-free graphene. The high-shear blending process using laboratory mixer L5M[62] was introduced by Paton*et al*[62] and allows large scalability, without additional centrifugation. Being able to produce large volumes (up to few L/h) made this method suitable for concrete mixing. The L5M mixer (blender) is shown

on Fig.3.3a with the main component – the rotor head, shown on the inset, where the exfolation mechanism happens.

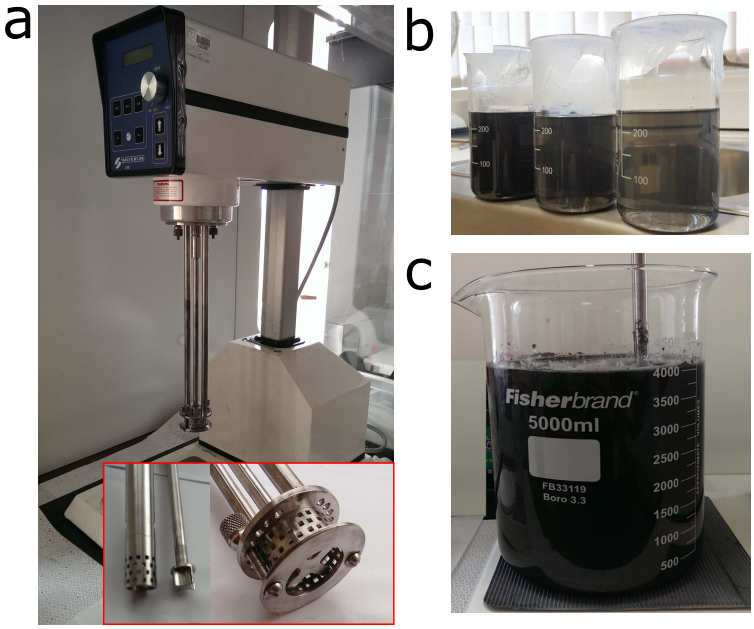

Figure 3.3: (**a.**) Photograph of the L5M blender used for high-shear exfoliation of FG and IG suspensions. The inset shows the two rotor heads – they have identical exfoliation mechanisms but are used for different volumes of production.(**b.**)Photograph of 3 FG concentrations showing the importance of the initial GP input. (**c.**) Photograph of $4L$ of solution being mixed. The color of the solution depends on the initial input of GP/IG powder.

Fig.3.3b shows a typical FG solution in three different concentrations of graphene suspensions. They differ in the initial input of graphite powder and as it can be clearly seen, this has great effect on the degree of exfoliation. Detailed analysis was performed on studying the effect of time and speed (the only two controlled variables in this process) on the number of layers and nature of defects in the graphene flakes, which can be found in Chapter 4. Fig.3.3c shows a schematic of exfoliation mechanism – the bulky graphite powder or industrial graphene are being sucked into the rotor head where the blade is rotating against the circular wall at very high speed, thus separating the weakly bonded graphite layers into thinner and thinner flakes. Fig.3.3c shows a

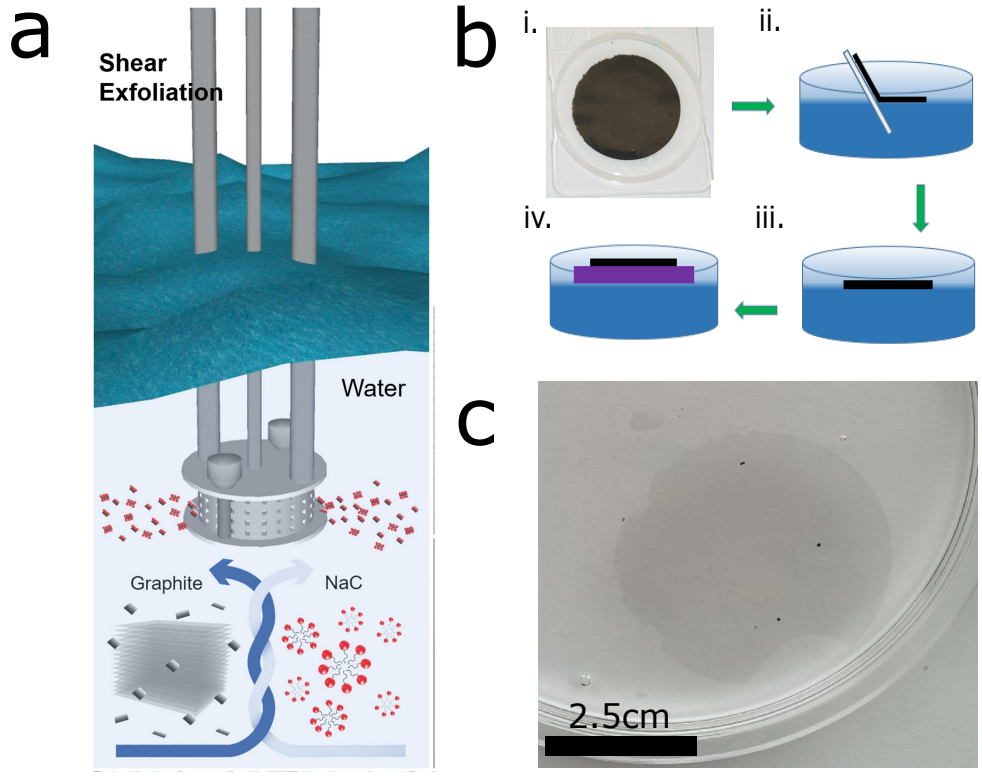

Figure 3.4: (**a.**) Schematic illustrating the mechanism of exfoliation – the graphite/industrial graphene is sucked between the rotating blade and head shaft, where turbulent forces break down the layers into few-layer graphene. (**b.**) Schematic of the 4-step 'fishing' transfer method (**i.**) $100mL$ of solution filtrated on filter paper (**ii.**) The thin film is detached back in water (**iii.**) Thin film is floating freely on the surface (**iv.**) Parts of this continuous thin film are taken out with SiO_2 substrate. (**c.**) Photograph of continuous graphene film ($5cm$ in diameter) on water surface.

beaker with $4L$ of solution with the rotor head submerged, which was often prepared and used for 4 concrete samples.

In order to characterise the quality and quantity of FG layers in the suspensions, exfoliated material was transferred from the water onto SiO_2 substrate. Fig.3.4b shows the 4 steps involved – firstly, $100mL$ of solution were filtrated on $0.025\mu m$ Millipore paper as shown on Fig.3.4b)i. and then after the thin film was dried, was detached from the filter paper and left floating on the surface of water (ii and iii). A photograph of floating thin film is shown on Fig.3.4c. The last

step in the transfer technique was to 'scoop out' the thin film using SiO_2 as a base, as shown on Fig.3.4b)iv. The FG flakes were ready for characterisation and analysis.

High-shear blending of Industrial Graphene

Industrial Grade 3 graphene (IG) powder was bought from online supplier with the following characteristics: purity 97%, X&Y Dimensions: $>2\mu m$, Average thickness: 8-15nm, Specific Surface Area: 500-700 m^2/g. The purpose was to blend the IG powder in a similar fashion like FG using the L5M blender, but without the addition of SCP. This resulted in a cheaper and more industrially scalable final product. In order to characterise the IG dispersions, the same transfer technique was used to deposit a thin film onto SiO_2 substrate. Fig.3.5a and Fig.3.5b show the thin IG film floating in water and then Fig.3.5c is a photograph of the IG on the substrate. Contrary to some feedback that carbon is hydrophobic and can not float freely in water, these IG dispersions were stable in aqueous solution both in time and quality. Chapter 4 presents a detailed study on the number of layers per IG flake.

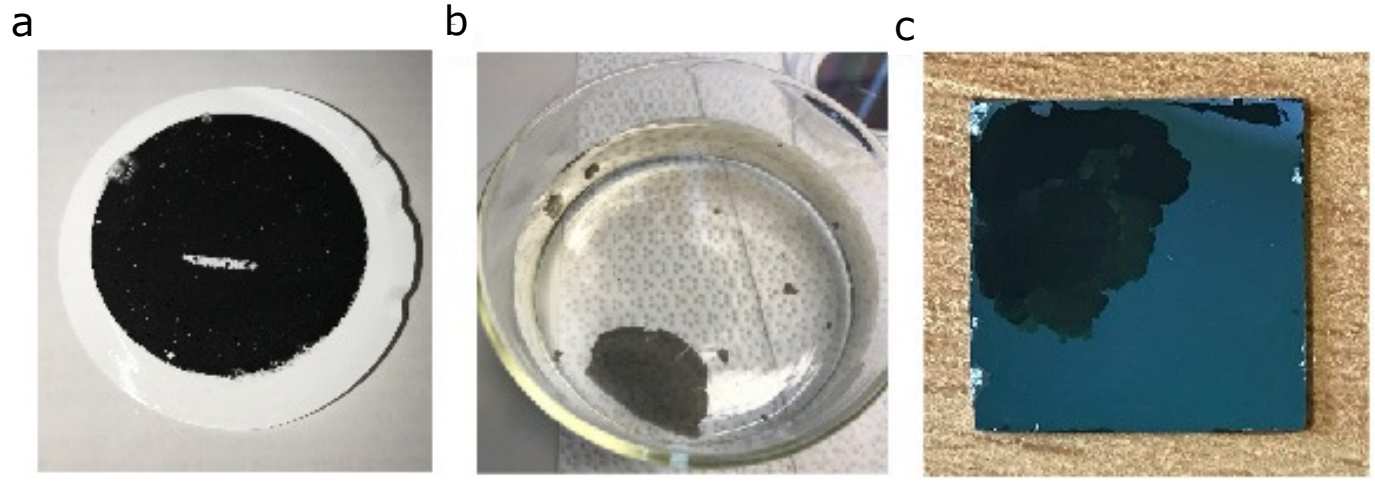

Figure 3.5: (**a.**) Photograph of $100ml$ of IG solution filtrated on a Millipore filter paper. (**b.**) The thin IG film floating on the surface of DI water. (**c.**) Photograph of the same film on SiO_2 substrate, ready for Raman characterisation.

Raman Spectroscropy of Graphene flakes

An ideal characterization tool for studying graphene flakes should be fast and non-destructive, offer high resolution, give structural and electronic information, and be applicable at both laboratory and mass-production scales. Raman spectroscopy fulfils all these requirements. The Raman spectrum[24] of graphite was first recorded more than 40 years ago and Raman spectroscopy became one of the most popular techniques for the characterization of disordered and amorphous carbons, fullerenes, nanotubes, diamonds, carbon chains and polyconjugated molecules[24]. Raman techniques are particularly useful for graphene because the absence of a bandgap makes all wavelengths of incident radiation resonant, thus the Raman spectrum contains information about both atomic structure and electronic properties.

The understanding of Raman processes in graphite and related materials has been studied for a long time by various researchers. The reason is the richness of phenomena combined with the wealth of experimental information that must be consistently arranged[24] Raman scattering is the inelastic scattering of photons by phonons. A photon impinges on a sample and due to it's fast changing electric field, only electrons respond to the excitation. Raman scattering happens when the photon can lose part of its energy in the interaction process, thus exiting the sample with a lower energy[24]. Since the excited sample has to return to a stationary state, the energy loss must correspond to a phonon energy[24]. If the incoming photon finds the sample in an excited vibrational state, and after the interaction the system returns to its ground level, the photon can leave the crystal with an increased energy[24]. The vast majority of Raman spectra in literature plots the intensity of the scattered light as a function of the difference between incident and scattered photon energy, the so called "Raman shift".[24]

Raman spectroscopy was the main tool used for quantifying the graphene suspensions used for concrete reinforcement. This laser system shines light onto the sample and collects the scattered

light, due to change in energy (interaction with molecular vibrations). The collected information, in the form of vibrations of atoms, gives information about the chemical composition and structure of the material observed. For this work, $532nm$ laser was used to scan thin graphene films, deposited on SiO_2 substrate.

Fig.3.6a shows two micrographs comparing the quality of exfoliation and film continuity. Fig.3.6a)i shows a drop-casted flake obtained after $24h$ of ultrasonication and centrifugation for $1h$ at 5000 rpm speed. Fig.3.6b)ii. shows micrograph of a continuous thin film obtained from high-shear blending and then transferred using the method from Fig.3.4b. There is clear visible difference in the quality between the ultrasonication and high-shear blending methods – the second method produces much larger volume of few-layer graphene flakes.

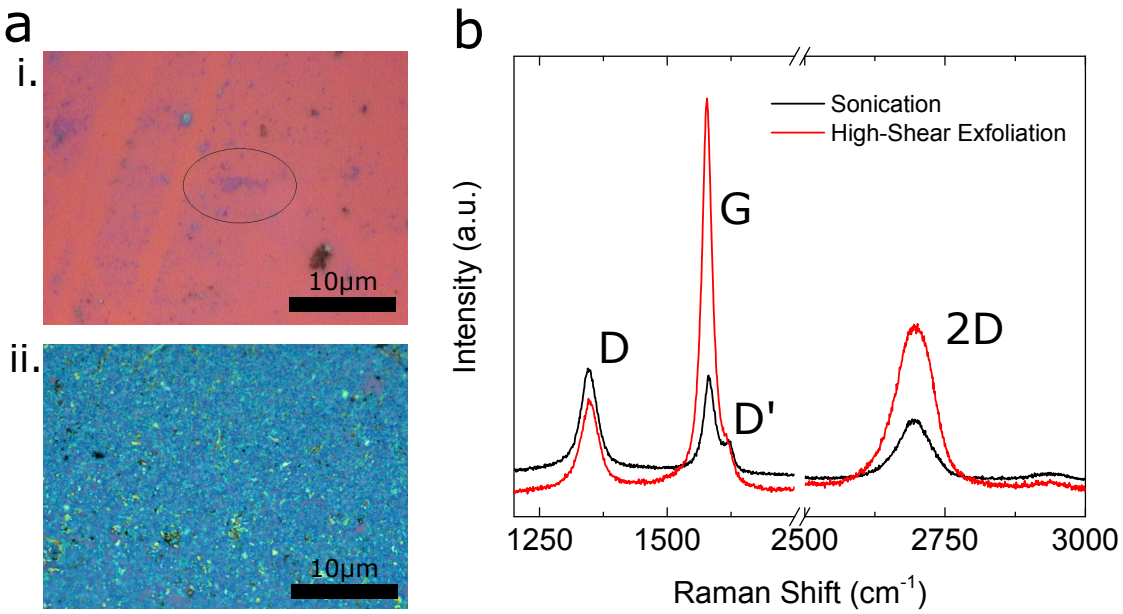

Figure 3.6: (**a.**) Micrographs taken with the same resolution showing (**i.**) drop-casted graphene flake produced from sonication and (**ii.**) thin continuous graphene film produced from high-shear blending (**b.**) Representative Raman Spectras of graphene produced from both sonication and high-shear mixing methods.

Fig.3.6b shows the corresponding Raman Spectras for both exfoliation methods. The spectrum

focuses on 4 important peaks – the D at $\sim$1300(cm^{-1}), G at $\sim$1650(cm^{-1}), D$\prime$ at $\sim$1680(cm^{-1}) and the 2D peak at $\sim$2700(cm^{-1}). In-depth analysis of various graphene spectras and peak ratios is presented in Chapter 4 to further understand the number of layers per flake and assess the quality of defects.

SEM Images of Graphene Flakes

Scanning Electron Microscope (SEM) uses a focused beam of high-energy electrons to generate a variety of signals at the surface of solid specimens. The signals that derive from electron-sample interactions reveal information about the sample including external morphology and orientation of materials making up the sample. Accelerated electrons in an SEM carry significant amounts of kinetic energy, and this energy is dissipated as a variety of signals produced by electron-sample interactions when the incident electrons are decelerated in the solid sample. These signals include secondary electrons (that produce SEM images), backscattered electrons (BSE), diffracted backscattered electrons, visible light and heat. Secondary and backscattered electrons are commonly used for imaging samples: secondary electrons are most valuable for showing morphology and topography on samples and backscattered electrons are most valuable for illustrating contrasts in composition in multiphase samples. Data are collected over a selected area of the surface of the graphene sample, and a 2-dimensional image is generated that displays spatial variations in these properties.

SEM was used to study the area of a few-layer graphene flake. The same deposited film from Fig3.6 was used and scanned to obtain micrographical information. Fig.3.7a shows a magnification of the thin graphene film, containing flakes with various shapes and sizes. In order to quantify them, many flakes were highlighted in green, as shown on Fig.3.7b, and computer image analysis was performed to calculate the number of pixels and consequently, the area size. Results show that the graphene flakes vary from 0.07 μm^2 to 1.06 μm^2 in size.

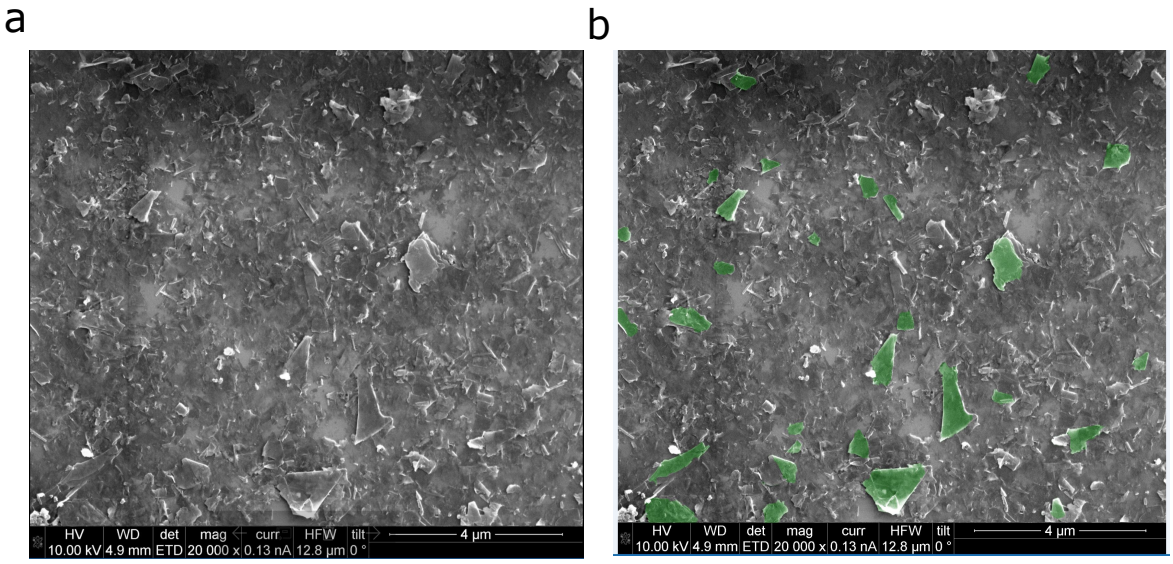

Figure 3.7: (**a**.) SEM Micrograph showing the nature of graphene flakes exfoliated using high-shear mixing method. (**b.**) Selected flakes are highlighted in green colour using computer software and then image analysis was performed to determine the average area per flake.

CONCRETE SAMPLES PREPARATION

Preparation and testing of all concrete samples followed BS EN 12390-1:2012[?] which are the British and European standards for concrete construction materials. Cubes were used for the compressive strength and modulus experiments, beams were used for the flexural strength and modulus and notched beams for the nonlinear fracture mechanics analysis.

Cubes and Beams

This work compares standard concrete (SC) prepared with tap water to various reinforced concrete groups, using different graphene types and concentrations. All experimental groups followed the same preparation, curing and testing procedures. Fig.3.8 shows the steps in concrete mixing – i) raw materials used to mix with graphene solution, ii) the mixer and the vibrating machine, iii) fresh concrete poured in $100\times100\times100mm$ steel moulds. The samples were left for 24h to harden,

then demoulded and left in water to cure for various time periods as shown in iv). 24h prior testing the samples were left to dry (20° room temperature) as shown in v). Lastly, Fig.3.8vi. is a photograph of the compressive testing apparatus which applies constant force of 1000 N/s until specimen complete failure. Vertical displacement transducer is placed at the back of the bottom plate to measure real-time deformation, used for elastic and plastic strain calculations.

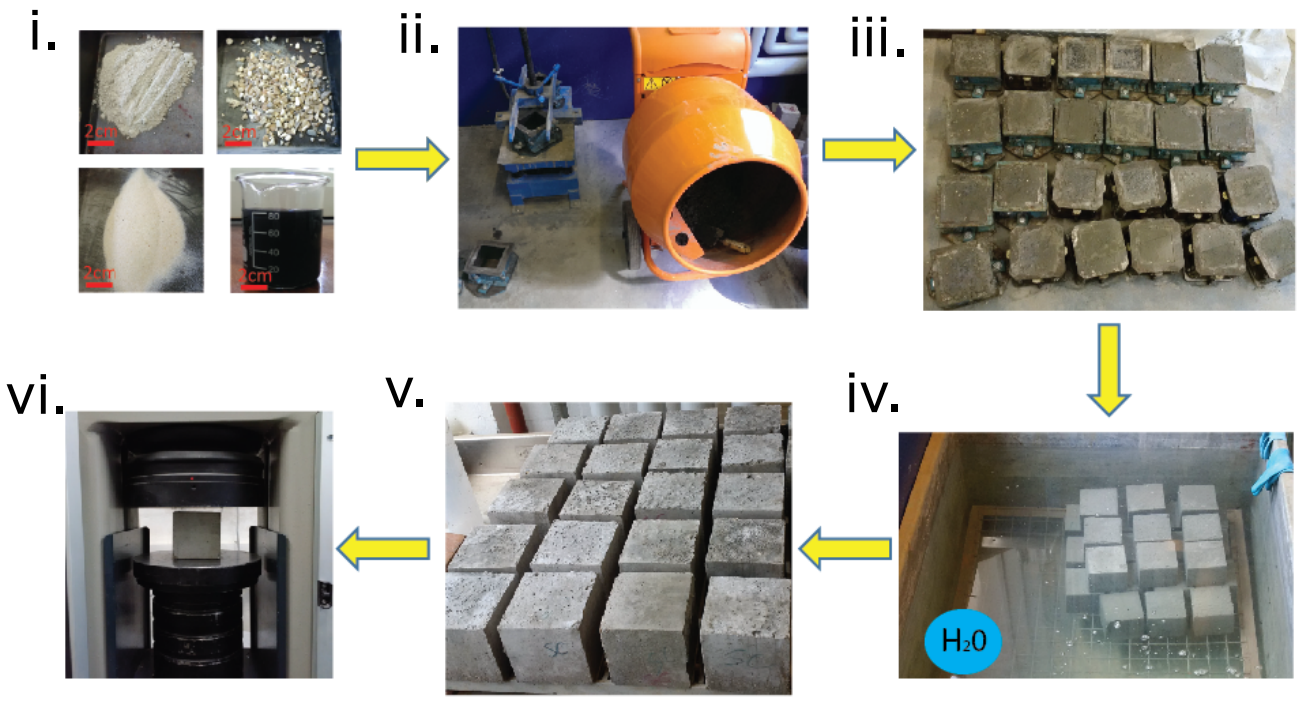

Figure 3.8: Sequence of steps for concrete preparation: (**i.**) Cement, sand, aggregate and water/graphene solution. (**ii.**) Cube moulds, vibrating machine and concrete mixer. (**iii.**) Photograph of freshly poured concrete in cube moulds. (**iv.**) Photograph of cubes left in water tank to cure. (**v.**) Photograph of samples left for $24h$ to dry in room temperature. (**vi.**) Photograph of the standard compressive loading apparatus.

The concrete beams used for 3 point bending (flexural) tests were composed of the same materials shown in Fig.3.8i, keeping the w/c ratio 0.5 and cement-sand-aggregate to 1:2:3. The schematic shown on Fig.3.9 gives details about the geometry of a single beam – profile sides $a =$

$b = 100\ mm$ and overall length L of 400 mm. The span between the bottom supporting rollers is 360 mm and the top roller is located at midspan. The force applied by the testing machine is from the top, as indicated with an arrow. The vertical displacement transducer was placed on top of the roller to collect the midspan deflection as accurately as possible.

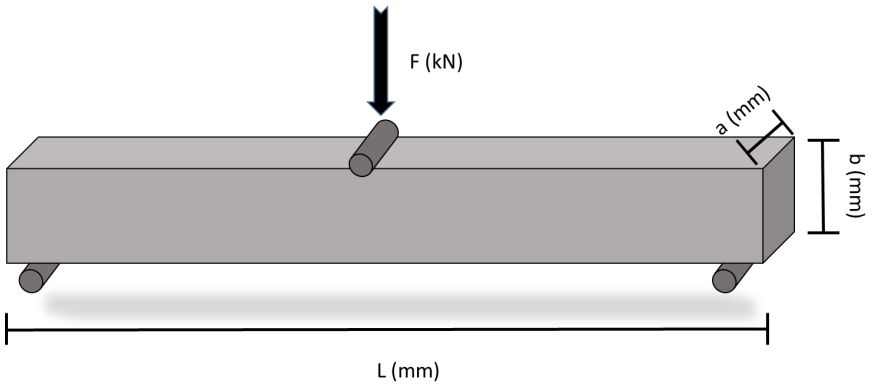

Figure 3.9: (**a.**) Schematic of a concrete beam used for three-point bending test, indicating the location of force applied as well as dimensions ($\mathbf{a} = \mathbf{b} = 100mm$, $\mathbf{L} = 400mm$).

CEMENT AND CONCRETE SAMPLES FOR ELECTRICAL AND THERMAL CONDUCTIVITY PROPERTIES

This section presents details about the samples used for electrical and thermal conductivity measurements. For these experiments, cement prisms and concrete cubes were prepared according to BS EN 12390-1:2012. Pre-cut copper (mesh) electrodes dimensions of $3{\times}6mm$ and 8×8mm respectively were inserted while pouring into moulds. The cement prisms were prepared with cement powder and water/graphene solutions (having 0.5 w/c ratio). No sand or aggregate was added in order to study the electrical conductivity of cement only. One prism has length L of $150mm$ and a square side with side a of $40mm$. The two pairs of electrodes were positioned at equal distance from the edge of the sample as shown on Fig.3.10a. The outer two were offset by 20 mm and the inner – at 40 mm.

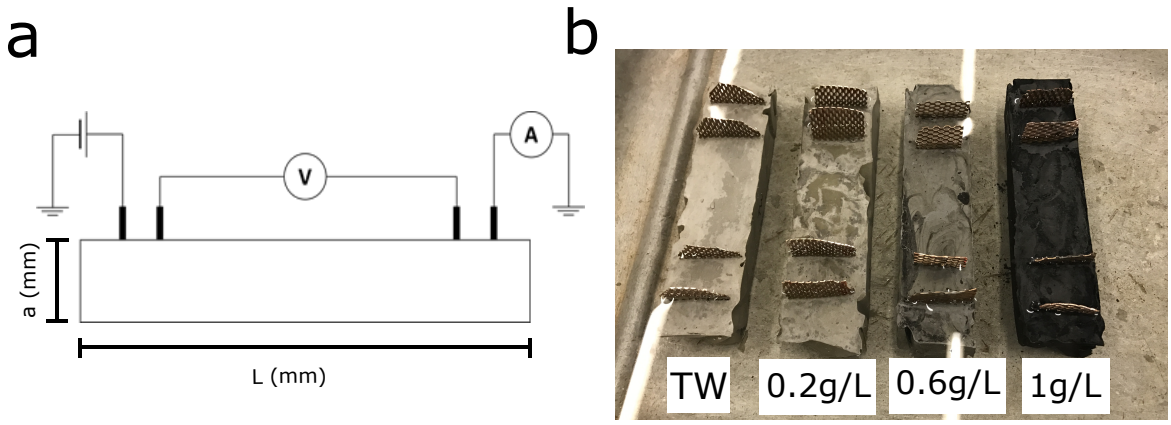

Figure 3.10: (**a.**) Schematic of a cement prism with dimensions, including 4 copper electrodes. (**b.**) Photograph of cement prisms with tap water and various graphene concentrations in increasing order.

The photograph on Fig.3.10b shows representative samples used in the experiment – normal cement (TW) and three graphene reinforced samples with increasing concentration.

The concrete cubes for this experiment used the same materials and followed the same preparation procedure as discussed earlier in this chapter. The new addition were the 4 copper electrodes spaced out at equal intervals from the edge of the cube – the outer ones were at $20mm$ and the inner at $40mm$ distance. Fig.3.11a shows a schematic of cubes with the electrodes and Fig.3.11b is a photograph of the samples. Their differ in increasing graphene concentration, similarly to prisms in Fig.3.10b.

X-Ray Diffraction of Cement powder

In order to quantify the microstructural changes in the cement crystals, due to graphene reinforcement, XRD was used to collect data. Background work and theory on this type of study[35] states that a crystalline material can be formed of only one crystalline or more crystalline phases. Such phase is defined by a certain system (monoclinic, rhombic, tetragonal, hexagonal, cubic), by a certain elementary cell and by its parameters[35]. In crystallography, the planes and families of

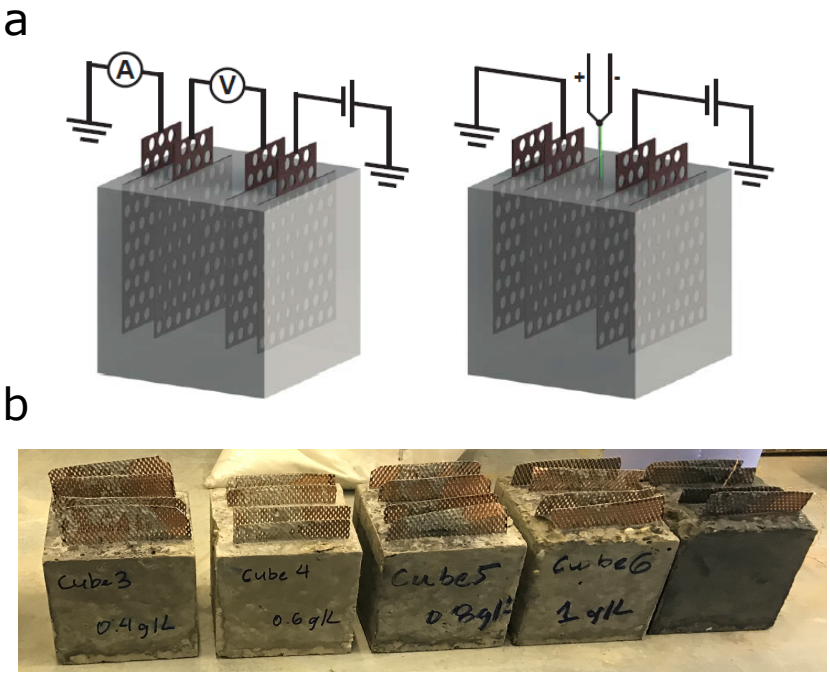

Figure 3.11: (**a.**) Schematic of concrete cubes used for electrical conductivity and heat transport measurements. The second cube shows a thermocouple inserted between the inner two electrodes. (**b.**) Photograph of cubes containing various graphene concentrations in increasing order from left to right.

atomic planes are noted with the hep of Miller's indices (h k l), fielded by the intersection of the atomic planes with axes x, y, z.

X-rays are electromagnetic waves, similar to light, but with a much shorter wave length (λ=0.2-200). Diffraction is a physical phenomenon that consists of electromagnetic waves avoiding obstacles when their size compares to the wavelength[35]. This phenomenon can be used to analyse materials as the atomic planes in a material are at comparable distances to the X-ray wavelength. When a monochromatic beam of X-rays falls on a crystal, the spherical waves emitted will cause the atoms, subject to this light, to constantly interact with each other. A destructive interference will be present in all space, except for some directions, called diffraction directions[35]. In a periodic display of atoms (crystalline state), the various parallel planes are situated at a distance d. The

constructive interference of the waves occurs, that is diffraction peaks are reached for a given wavelength λ only if Bragg's law is observed[35]:

$$2dsin\theta = n\lambda$$

where n is constant, d is the inter-atomic distance and θ is Bragg's diffraction angle. This process is visually represented in Fig.3.12a.

X-rays diffraction is produced as a reflection at well defined angles. Each crystalline phase has its own diffraction spectra. For the current XRD system a Bragg–Brentano arrangement (the specimen is rotated by the diffraction angle theta while the detector is turned by the angle 2θ, as shown on Fig.3.12b.:

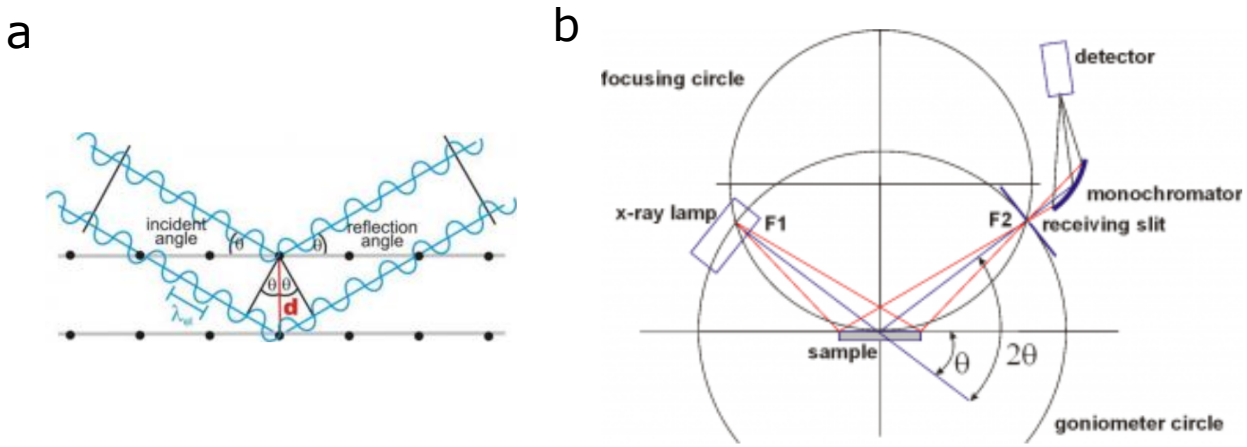

Figure 3.12: (**a.**) Schematic representation of Bragg's law. (**b.**) X-Ray Diffractometer basic working principle.

The diffractometer collects data in pulses/seconds and represents is as radiation intensity in the forms of peaks, measured in 2θ angles. It gives valuable information about the material's structure, mainly in determining the crystalline structure of the crystals which includes texture, size and internal stresses as well as qualitative and quantitative analysis of the crystalline phases[35].

Part II

Graphene-Concrete Composites

4

RAMAN SPECTROSCOPY OF GRAPHENE SUSPENSIONS

INTRODUCTION

Owing to its ultrathin, two-dimensional nature and its extraordinary mechanical, transport and electrical conductivity properties graphene has attracted much attention in the scientific community. In the years to come, graphene will find many commercial applications, ranging in the huge spectrum between printed electronics, conductive coatings all the way to the construction and aerospace industries. It will be used as a low-cost electrode material in applications such as solar cells, batteries or sensors as well as protective coating on aeroplane wings or enhancing the chemical reactions of structural materials on the nanoscale level, aiming to improve range of properties. In order to explore the aforementioned opportunities, graphene has to be taken out of the lab and manufactured on large scale.

Previous in-depth work towards achieving this goal, carried out by M. Lotya *et al*[49], showed the successful separation of graphite layers in aqueous environment and more importantly – the work presented a technique to prevent re agglomeration of graphene layers. However, to progress from

the laboratory state-of-the-art research to commercial applications, it was necessary to develop method for producing large quantities of high-quality, water-stabilized graphene. After examining and studying the literature on the topic[49;62;79;29;92] it was concluded that high-shear mixing exfoliation outperformed ultra-sonication mainly by scalability which was the crucial factor for the overall success of this research work. The high-shear mixing was different to sonication because to separate the graphite layers, unlike ultrasonic pulses, which were very time consuming (typical exfoliation took between $24h$ and $48h$) it used high-shear turbulent forces principles. The industrial blender L5M[62] used for high-shear exfoliation of graphene used a rotor blade which rotated at speeds up to $8000rpm$ which was fast enough to create surface tension sufficient to break the weak Van-Der-Vaals forces holding graphite layers together. Even the smallest graphene solutions (in the range between 50-$100mL$) contained vas amount of defect-free flakes with various shapes and sizes which was perfect for concrete reinforcement.

In order to quantify the newly developed method[62] for large scale exfoliation of unoxidised, water-stabilised graphene suspensions, Raman Spectroscopy was used as the main tool for obtaining the number of layers per flake and assessing the nature and level of defects. The results presented below are based on FG and IG graphene flakes transferred from thin filter paper onto SiO_2 substrate, using the 'fishing method' described in Chapter 3. The purpose of this chapter is to show the huge systematic study performed on various water-stabilized graphene concentrations and outline the logic behind choosing the right parameters, suitable for later concrete reinforcement.

EXPERIMENTAL DETAILS

The experiment I carried out to exfoliate the graphene suspensions and optimise the solutions had to be tailored to my final goal – incorporating it into concrete mixing. Therefore, my efforts

emphasised on overall cost of preparation, time, quality and scalability. This method is not particularly useful for preparing electronic devices or coating fibres and textiles simply because it was using tap water (instead of purified/deionised) and the final product was not centrifuged. I had to demonstrate a method which aimed at direct industrial concrete application and therefore excluded decanting of the graphite sediment (if any, because most of the optimised ratios were carefully calculated so that they can minimise the initial graphite input).

The first step in obtaining a correct formula for graphene solutions preparation was to investigate the effect of various parameters in the exfoliation process. These parameters included both the L5M blender time and speed functions as well as the initial input quantities of graphite powder (GP) and the surfactant sodium cholate powder (SCP). Wei *et al*[92] suggested using ethanol (solvent) but the quantity of graphene produced using this method was not satisfactory, therefore results from surfactant-stabilised graphene dispersions exfoliation are presented only. Fig.4.1 shows a systematic study which compares the effect of the afore mentioned parameters on the quantity and quality of graphene by examining the Raman spectra of various samples. As discussed in Chapter 2, each of the four peaks in one spectra reveals information about the number of layers per flake and the nature of defects.

The same input ratio of GP/SCP was used and only the L5M blender functions were changed to get better understanding of the exfoliation mechanism. Generally, each speed in the range I selected (3000 - 8000 rpm) produced graphene flakes, but due to the optimisation I presented the range between 4000rpm and 7000rpm only. The reason for this is that for speeds below 4000rpm there was too much unexfoliated graphite at the bottom of the solution and for those above 6500-7000rpm there was foam produced, due to the addition of the surfactant (which molecular structure is that of a commercial detergent), both of which were unfavourable for mixing with concrete.

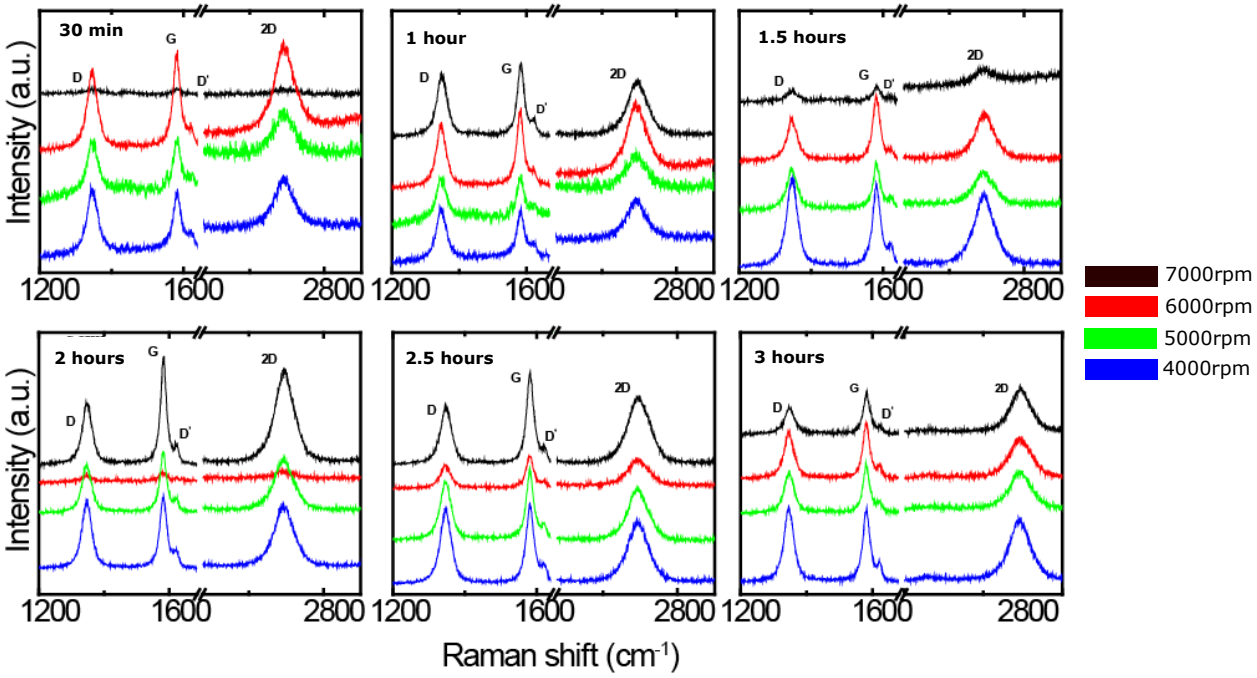

Figure 4.1: (**a.**) Panel of 6 plots showing the influence of time and speed of blending on the Raman Spectra of graphene dispersions. (**b.**) 2 panel plot showing the ratios of I_G/I_{2D} and I_G/I_D as functions of 5000 *rpm* blending speed and 2 *h* blending time.

The panel of graphs in Fig.4.1a plots all spectras for 4 different speeds and 6 time intervals. As it can be seen almost all of them contain the D, G D*′*, and 2D peaks, characterising a typical graphene atomic structure. More information on the relationship between the peaks is to be presented later in this Chapter. The ratios of I_G/I_{2D} and I_G/I_D were extracted and analysed separately. Overall the best ratios, in terms of low I_G/I_D ratio and high I_G/I_{2D} one, were found to be – 5000 *rpm* blending speed and 2 *h* blending time as shown in Fig.4.2.

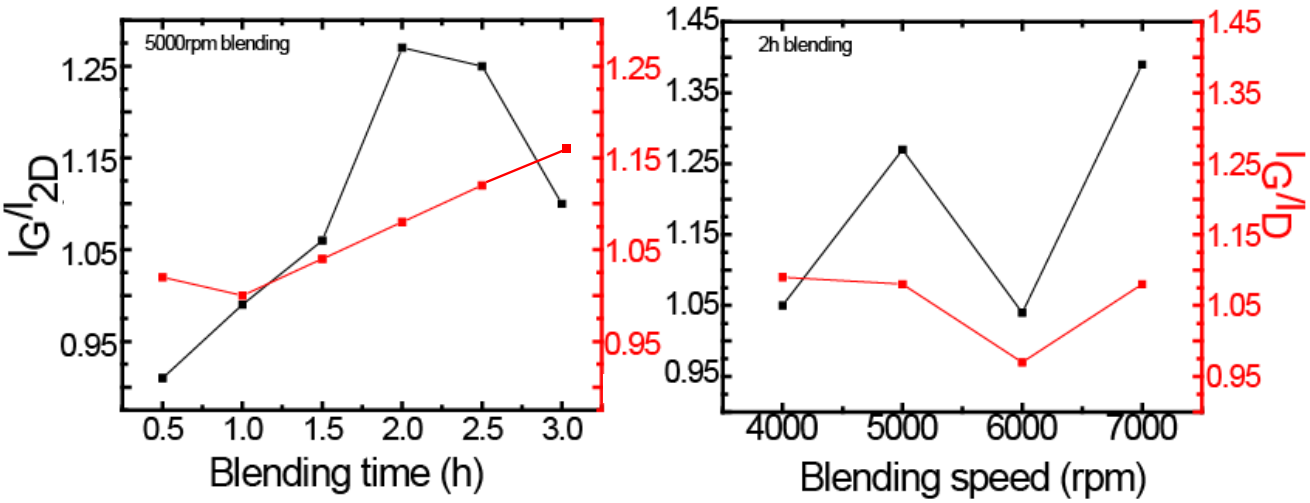

Figure 4.2: (**a.**) Panel of 6 plots showing the influence of time and speed of blending on the Raman Spectra of graphene dispersions. (**b.**) 2 panel plot showing the ratios of I_G/I_{2D} and I_G/I_D as functions of 5000 *rpm* blending speed and 2 *h* blending time.

Again, defining 'best' in this case is tailored to the final goal of incorporating the solutions into concrete mixing so when choosing these two parameters I had to take this into consideration too. For other purposes, such as spray-coating on fibres and textiles for example, higher blending speeds and longer time are recommended. The literature[62] has shown that there is linear dependence between increasing the latter two and flakes' size. The experiments in this thesis were carried out on non-centrifuged samples which imposes differences on the final FG or IG graphene concentration (C_g). Centrifugation of samples decants the large, multi-layer graphene flakes and only thin suspensions are left for the Raman study.

After the optimal time and speed of blending were identified, the next step was to test various input concentrations of graphite and sodium cholate. Table4.1 presents various initial concentrations and as the literature[62] suggested, the first one was used for initial experiments. Following these trials, graphene suspensions were mixed with concrete and the results from preliminary me-

chanical tests showed that this C_g is too high – there was graphite sediment left and for reasons explained in next chapters, this was unfavourable for long term strength and durability. The input concentrations for solution processing were then halved few times as summarised in Table4.1. After more in-depth analysis, presented in the next section of this chapter, the initial C_g was identified and the resulting concrete samples were labelled as Ultra Thin Graphite (UTGr).

Table 4.1: Input parameters for production of a sample Functionalised Graphene Solution with various final concentrations.

Input	Blending Parameters	Output
50 mg/mL Graphite & 10 mg/mL Sodium Cholate	2 h @ 5000 rpm	2.35 g/L FG
25 mg/mL Graphite & 5 mg/mL Sodium Cholate	2 h @ 5000 rpm	0.92 g/L FG
12.5 mg/mL Graphite & 2.5 mg/mL Sodium Cholate	2 h @ 5000 rpm	0.59 g/L FG
6.25 mg/mL Graphite & 1.25 mg/mL Sodium Cholate	2 h @ 5000 rpm	0.25 g/L FG
4 g/L Industrial Graphene	2 h @ 5000 rpm	0.7 g/L IG

After analysing results from concrete mechanical testing, the best performing samples were reinforced with 0.59 g/L graphene (FG) and I chose to further investigate this particular ratio. The last material listed in 4.1 is the industrial graphene (IG), purchased from CheapTubes.com[?] . Fig.4.3a shows a single Raman spectra of IG and Fig.4.3b is a representative example of the technique used to estimate the number of layers per flake. This technique is explained in details in the following section of this Chapter.

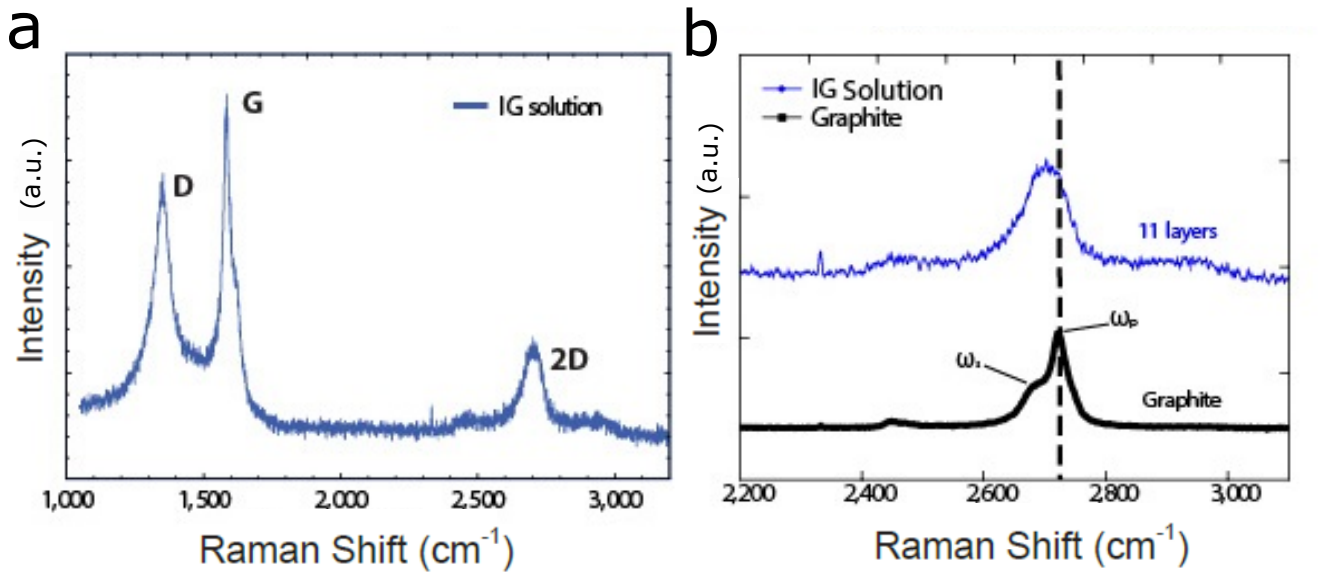

Figure 4.3: (**a.**) Typical Raman Spectra of IG suspensions produced from high-shear exfoliation. (**b.**) Plot studying the number of layers of IG suspensions when compared to standard graphite.

The next section of this chapter presents our study and characterisation of UTGr, FG and IG graphene solutions, all of which were used later for concrete reinforcement.

RAMAN STUDIES ON FUNCTIONALISED AND INDUSTRIAL GRAPHENE

Estimating the number of layers

After identifying the ultimate parameters for high-shear exfoliation of graphene, suitable for the purposes of this research, the attention was turned towards studying carefully the number of layers in the dispersions and consequently, their quality. This was needed due to the presence of the *D* peak in almost all spectras presented in Fig.4.1 and Fig.4.3. Ferrari *et. al*[24] was the first to estimate the number of layers by fitting the 2D peak of the Raman Spectrum and measuring the full width at half-maximum. Their work paved the way for further studying the graphene flake's thickness, number of monolayers and defects. Paton *et. al*[62] expanded Ferrari's work and combined Atomic

Force Microscopy (AFM) data with Raman spectroscopy measurements to optimise the estimation of layers. In the supplementary information of their paper[62] they provided a detailed explanation of the afore mentioned relationship. Fig.4.4 shows a surfactant-stabilised graphene flake, produced from high-shear mixing, through AFM and Raman Spectroscopy measurements:

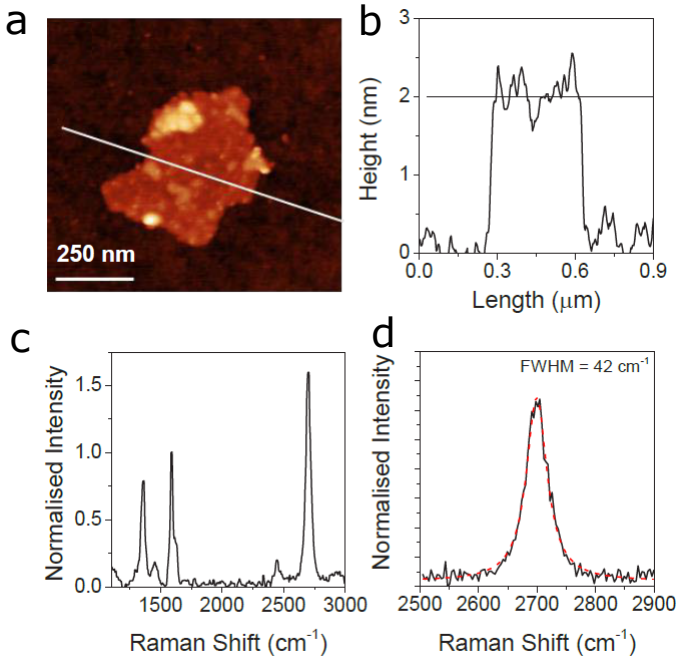

Figure 4.4: (**a.**) AFM image of a suspected monolayer graphene sheet (**b.**) corresponding height histogram displaying a height of close to 2 *nm*, (**c.**) and (**d.**) Raman spectrum (532 *nm* excitation) of the flake in (**a.**) evidencing its monolayered nature, adapted from[62].

This work continued and further analysed other works[42;89] reporting Raman Spectroscopy used as tool for estimating the number of layers of graphene flakes. They concluded that there is quantitative relationship between the spectras of graphene nanosheets and the graphite used for exfoliation. I have referred to their conclusions and analysed the graphene that I produced for this research work.

Prior to their incorporation in concrete I characterised graphene (FG and IG) and ultra-thin

graphite (UTGr) materials by fabricating thin films, as shown in Chapter 3. To this end the dispersion was filtered through a mixed cellulose hydrophilic Millipore(R) membrane with 0.025 μm pore size. Raman spectroscopy was performed on representative areas of 20x20 μm^2 and used to study the number of layers and the nature of defects in the continuous film. Fig.4.5a focuses on the range between 2500cm^{-1} and 3000cm^{-1}, where the 2D peak is found. Firstly, the graphite peak, located at 2724cm^{-1}, served as a comparison for all other 3 spectras. The 2D peak was defined as ψ_p and a the smaller shoulder to the left, found at -30cm^{-1} units away, was defined as ψ_s. To estimate the number of layers, I used the ratio of the intensities of the graphite and graphene 2D peaks:

$$M = \frac{\frac{\psi_{p,G'ene}}{\psi_{s,G'ene}}}{\frac{\psi_{p,G'ite}}{\psi_{s,G'ite}}}$$

and substituted it in the empirical formula[62]:

$$N = 10^{0.84M+0.45M^2} \tag{4.1}$$

where N is the number of layers per flake. I found that a typical FG graphene dispersion is composed of 4 - 7 monolayers, with the majority being 6. This calculation is confirmed by the Raman map, as shown on Fig.4.5b. The panel presents maps for thin continuous films of UTGr, IG and FG respectively and the estimated number of layers per flake throughout the entire dispersion. The UTGr holds its name from the 'bulky' structure – containing between 20 and 25 monolayers per flake, while the IG and FG span between 4 and 14. The uniformity of dispersion is clear, with one predominant colour on each of the maps. This confirms the very high yield of the liquid exfoliation method using the high-shear blending technique.

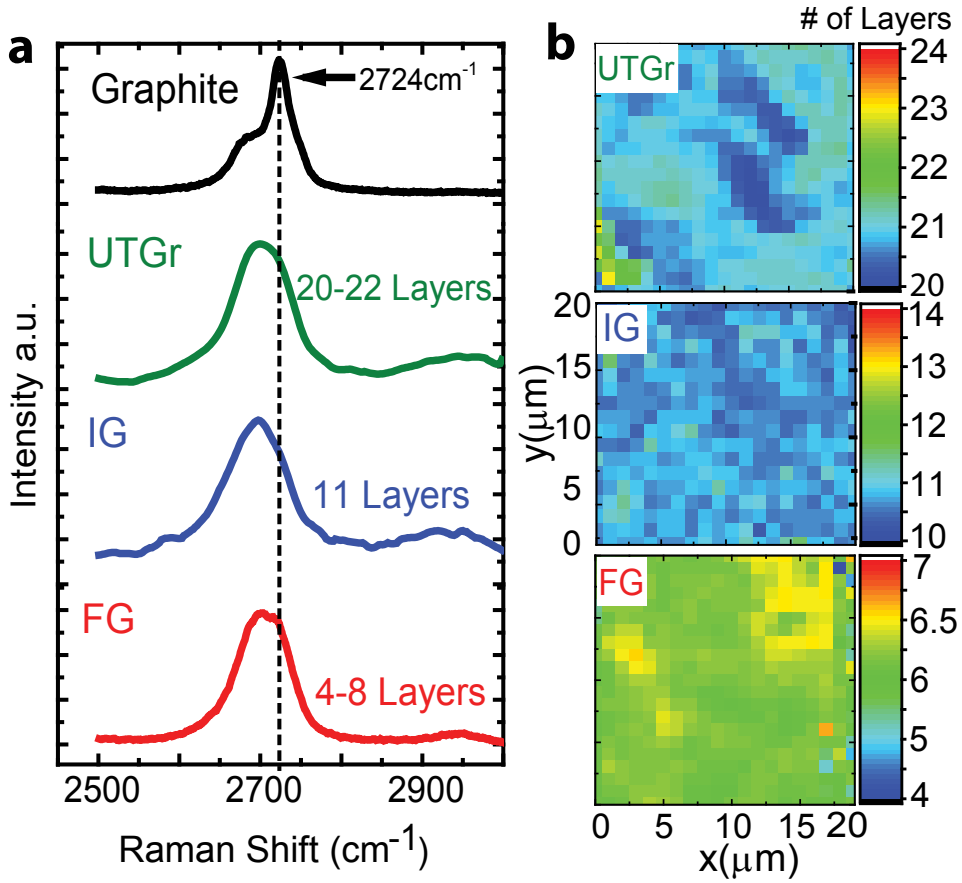

Figure 4.5: (**a.**) Comparison of the 2D peak position of graphite and different thicknesses of graphene flakes. (**b.**) Raman map of the number of layers across the continuous film, showing UTGr, IG and FG respectively.

Nature of defects

To get an overall quantified conclusion of the liquid-phase exfoliation demonstrated in this chapter, it is very important to asses the nature and level of defects, which are always present on the surfactant-stabilised graphene dispersions. Different types of defects – being sp^3, vacancy or edge(boundary) can directly affect either the mechanical or electrical conductive properties of graphene. To assess the level of defects I measured the D peak (around 1340cm^{-1}), the G peak (around 1600cm^{-1}) and *D′* peak which is visible as a small shoulder on the right side of G. The

intensity ratio of D and G peaks (I_D/I_G) which is one of the parameters used to quantify the defects in graphene varies between the three different types of graphene. I studied the range of intensity ratios for UTGr, IG and FG and performed computational analysis which plotted all the intensities from 400 Raman spectras in a map, as shown on the panel of Fig.4.6a.

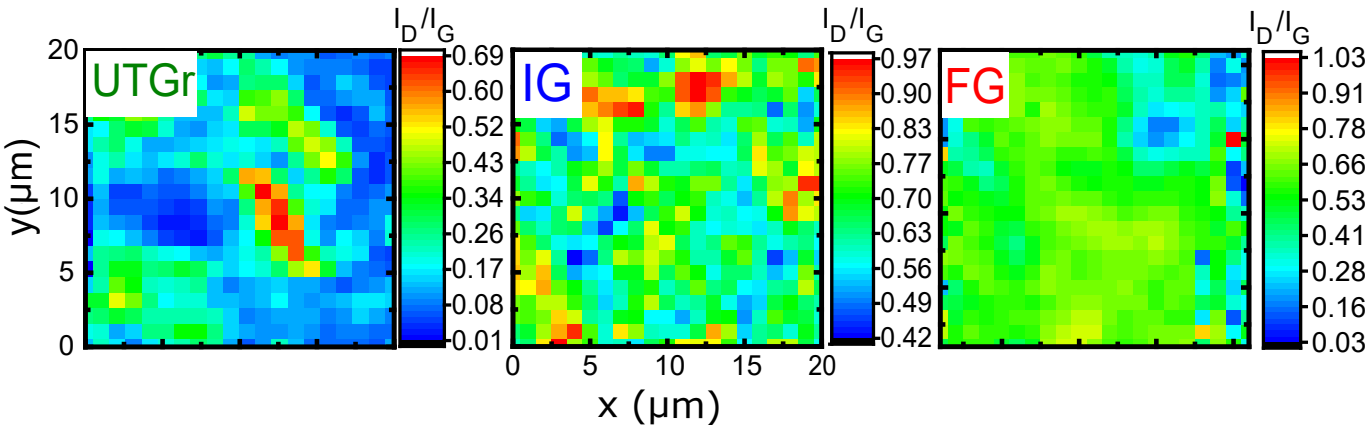

Figure 4.6: (**a.**) Maps showing the I_D/I_G ratios of a uniform area of the continuous graphene film for each of the three types deposited on SiO_2 substrates.

The I_D/I_G ratio for all 3 types of graphene vary between 0.01 and 1. For UTGr, more than half of the continuous film is close to 0.1, which is normal since there are many layers per flake and the G peak is quite tall when compared to the D. The IG film shows a mixture of I_D/I_G ratios, with 0.7 as predominant. The scattered results are due to the lower quality of this commercial graphene source, when compared to the one I produced from graphite powder. Finally, the FG has the best uniformity, consisting with more than 80% of $I_D/I_G = 0.53$. I selected one representative scan of each map corresponding to the intensity ratio with highest occurrence (0.08 for UTGr, 0.7 for IG and 0.53 for FG) and plotted the single scan, focusing on D, G and D' peaks as shown on Fig.4.7b. This indicates defects present everywhere along the area of the dispersion and its necessary to study what particular type are they.

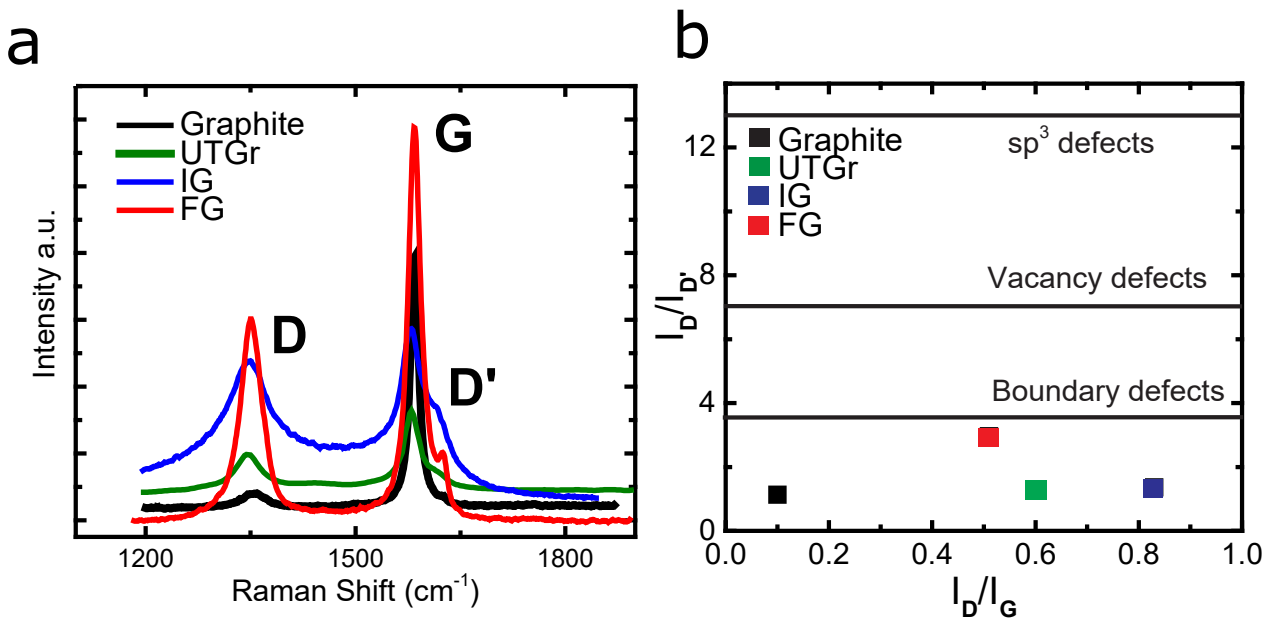

Figure 4.7: (**b.**) One spectrum of each graphene type showing the G, D and D′ peaks in comparison with bulk graphite. (**c.**) Plot of the $I_D/I_{D'}$ ratios corresponding to the four I_D/I_G ratios from H showing that there are no defects introduced to the basal plane of the graphene dispersions.

In order to do this, the relationship (ratio) between $I_D/I_{D'}$ was taken into account as well, as suggested in literature[21]. It was found that a ratio between I_D/I_G and $I_D/I_{D'}$ around 14 corresponds to sp^3 defects, whereas $I_D/I_{D'}$ of 7 and 3.5 correspond to vacancy and boundary defects, respectively[21]. As shown in Fig.4.7c, the $I_D/I_{D'}$ of ≈ 2.39 found in our graphene films demonstrates that for the whole range of I_D/I_G the level of defects is always below the benchmark for boundary defects. This means that the high-shear mixing does not introduce any defects to the basal plane of any of the three UTGr, IG and FG types of graphene. This is very important for preserving the mechanical strength of the graphene sheets and their ability to retain initial size after strain, both of which are crucial for mixing it with concrete.

CONCLUSIONS

In conclusion, this chapter presents my work on liquid-phase exfoliation of graphene, using high-shear mixing of graphite and sodium cholate. It also showed results obtained on industrial graphene exfoliated using the same technique. This is an important chapter of my thesis because it was the stepping stone for the overall research. Through systematic investigation of the initial parameters of blending process and input materials, I optimised the solution processing in a suitable way for mixing it with concrete. Then, I prepared separate small representative samples of thin continuous film on $Si0_2$ in order to use Raman spectroscopy as an effective tool of estimating the number of layers per flake and quantifying the nature of defects, imposed due to the high-shear blending process. My results, focusing on the 2D peak, showed that the graphene exfoliated, ranged between 4 and 18 layers for both IG and FG, with the majority being either 6 or 10 respectively. The ratios of intensities I_D/I_G and $I_D/I_{D'}$ revealed that the high-shear exfoliation did not introduce any basal plane defects on the graphene dispersions, thus preserving the important mechanical properties. After having this solid and in-depth confirmation of the type of graphene, produced with the high-shear exfoliation, it was time to turn my attention to concrete preparation, mixing and testing which was the main aim of this research work.

5

MECHANICAL PROPERTIES OF GRAPHENE REINFORCED CONCRETE

INTRODUCTION

The increasing global population has definitely contributed to the rapid growth of new cities. Megalopolises on the other hand, have huge demand of design and constructing taller commercial properties, beautiful sky scrapers and more durable bridges. The creativity of architects has been backed up by research and innovations in various structural materials, the combination of which allowed the construction of remarkable buildings such as the Millau Viaduct in France (world's highest bridge)[51], the One World Trade Center in New York (Western Hemisphere's tallest skyscraper)[87] or the Tokyo Skytree (world's tallest tower)[87]. Civil and structural engineering science has reached new limits due to powerful computational software, which allows professionals to reduce the time for calculations and improve the structural stability of various buildings. The well-known combination between steel and concrete has been the most used type of reinforcement worldwide, literally found in each and every building that is designed for higher number of storeys. It's indisputable workability and effectiveness has proven over the decades, but there are few major

areas for improvement.

Among the urgent necessity for structural health monitoring, improving of fire-proof and water-proof (isolating) materials, the civil engineering community has to decrease the global carbon emissions due to cement manufacturing, which to current date account for more the 5% of global CO_2. This research work aims to provide a solution to the latter problem, thus to create a novel construction material which will help to decrease the green house gases and contribute to a more environmentally friendly construction industry.

Concrete is by far the most used construction material worldwide. To meet the never-ending demand for construction, leading manufacturers like China are producing up to 2 billion metric tons of cement annually. This is increasingly worrying in terms of contributions to the global climate change and therefore the research community of concrete and cement materials is currently focussing on various strategies that can slow it down. The core of my research work, presented in this chapter, aims to explore the fundamental mechanical properties of concrete, reinforced with graphene, and to prove that the application of nanomaterials to the construction industry is industrially scalable and not *in situ*. Out of the many other fascinating improvements that graphene introduces to concrete (presented in later chapters), the one which will have the biggest impact is the fact that by improving its compressive and flexural strength, we can use less volume of material to achieve the same architectural standards and engineering calculations, which will therefore lead to decrease in global cement production.

EXPERIMENTAL DETAILS

The European and British standards for construction demand that composite materials like concrete should be tested for their mechanical properties prior to being used at construction sites. This is done according to the Eurocode 2 standards, mentioned in Chapter 3. This process is

essential because it reveals important information about the quality of the mix, the workability and durability. The most important characteristic property of concrete is its compressive strength, followed by flexural one and modulus of elasticity. The first is tested via getting an estimate of few cube samples with dimensions $10\times10\times10cm$ and the second by rectangular beams with varying length-depth ratio, usually 1:4. The modulus of elasticity (E_c) for both properties is extracted from the experimental data. The standards require data from 7 and 28 days of concrete curing, named as early and late age strength respectively. In addition, I've performed experiments on several testing days in between the required range in order to obtain better understanding of the evolution of the hydration reaction.

This chapter presents results from compressive strength tests on cubes and from flexural one on beams, following the preparation procedures described in Chapter 3. The experiments were performed in the Concrete Testing laboratories, Harrison Building room 136 with apparatus supplied by Controls group. The compressive tests used $1000N/s$ constant loading speed while the three-point bending tests – $100N/s$. All cubes were slightly polished on both sides facing the plates to avoid noise in the displacement recordings. The beams were positioned on the rollers so that there is equal distance from both sides to each roller, making the span distance (S) $360mm$. The main goal of all the experiments is to compare the reference testing group(TW), which uses normal tap water, to various graphene reinforcements – various C_g dispersed in solutions and used for concrete mixing.

COMPRESSIVE STRENGTH RESULTS

As discussed earlier, the compressive strength f_c and modulus of elasticity E_c are arguably the most important mechanical properties of concrete for engineering design calculations. Values for f_c and E_c are used in worldwide standards to design the dimensions of structural elements like

beams, slabs, columns or pavements. In order to make accurate general conclusions on graphene's reinforcement, it is very important to test multiple cube samples and provide statistical evidence of any reoccurring differences and mechanical improvements.

Fig. 5.1 is a representative example of a typical curves extracted from compressive strength testing for concrete cubes cured for 7 days and produced using the three different types of concrete: reinforced with IG, FG and UTGr as well as the reference concrete, mixed with tap water. It plots the evolution of calculated compressive strength as a function of increasing vertical displacement, or, in this case it is shown as compressive strain in %. The stress–strain curve can be divided into two main sections – the ascending branch (from 0 to maximum strength) and the descending branch (from maximum strength to the failure point). The first half of the ascending branch is approximately a straight line and corresponds to the elastic region. This segment is labelled as $0.5f_c$, with f_c being the maximum strength of the cube. In this region the deformations due to compressive loading are reversible and mainly caused by slipping between bulk aggregates and cement crystals. The slope of this section gives the Young's modulus (E_c) of the material, which is a measure of its stiffness. As it can be seen from Fig. 5.1 graphene reinforcement results in a steeper elastic region compared to standard concrete, indicating a stiffer material with stronger bonds between cement and aggregates.

The green line on Fig.5.1 shows that there is a benchmark for the amount of graphene used – if the quantity is too much, the cement crystals are hampered from proper bonding and hydration is reversed.

After getting an overall idea of how exactly does the compressive strength testing work, the next step was to study the evolution of both f_c and E_c as a function of time. The reason for this is thoroughly explained in Chapter 2, but to refresh the reader's knowledge, it is briefly outlined here. The hydration reaction between cement and water essentially is transformation of fibrous cement crystals upon their reaction with water molecules. They evolve and grow up to the point

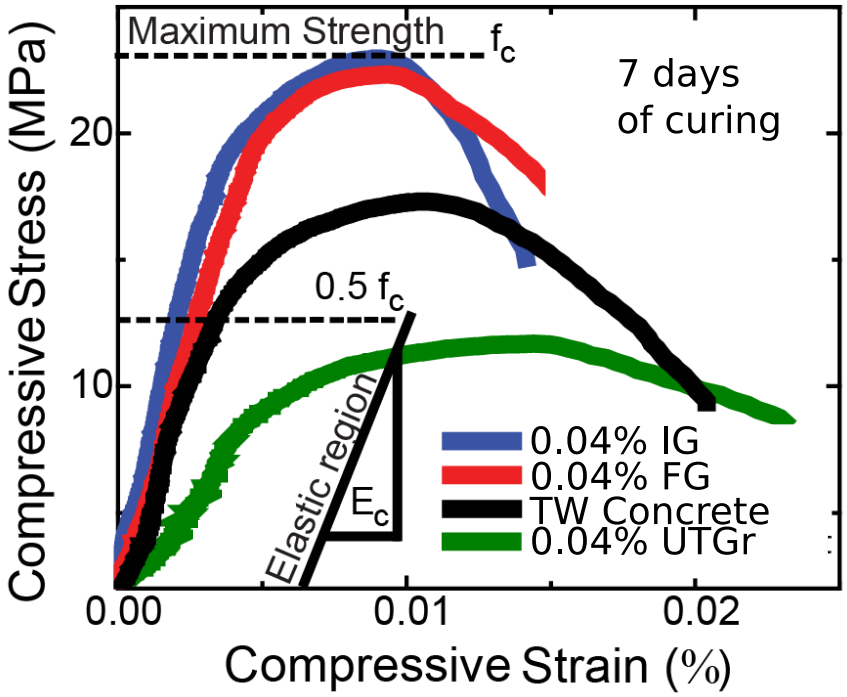

Figure 5.1: Typical stress–strain curve of concrete cube measured under compressive loading, comparing standard concrete, mixed iwth tap water, with graphene (IG and FG) and graphite (UTGr) reinforcements. Data plotted for samples after 7 days of curing.

of mechanical interlocking. This process evolutes with time and it is the most important factor in shaping all of the concrete's properties and long-term durability. In addition, attention has to be paid to the total % of air voids left in between the interlocking of crystals, because during external constant loading they become the first point of interplanar failing, which leads to dislocations and deformations. To better understand this theory and study it in practice, I performed tests on cubes after intervals of 7 days.

Fig. 5.2a shows the extracted values for E_c as a function of curing time. We observed that for early age concrete samples (i.e. after 7 days of curing) both FG and IG reinforced concrete have higher E_c than standard concrete – 30.7% and 35.8% increase respectively whereas graphite

reinforcement leaves the E_c unchanged. Furthermore, the values measured for later age concrete (i.e. after 28 days of curing) are very similar both in number and percentage increase to the values observed after 7 days of curing. This suggests that durability of the concrete remains stable over time, making it suitable for industrial applications.

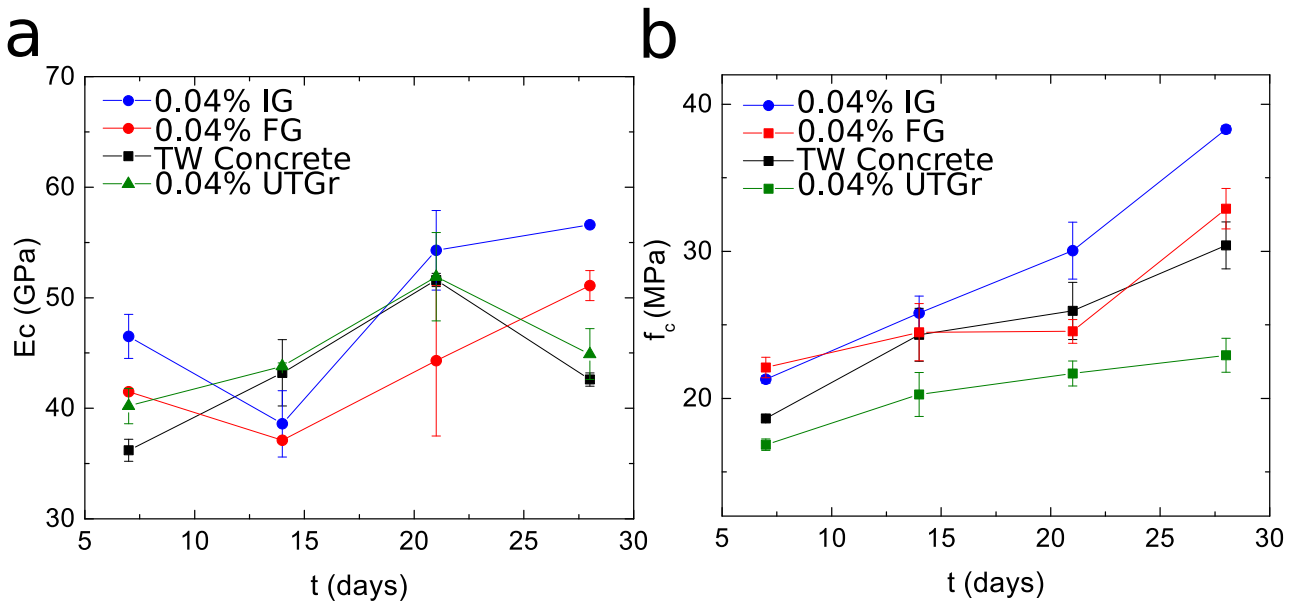

Figure 5.2: (**a.**) The evolution of compressive Young's Modulus (E_c) as a function of time, comparing standard concrete to all three types of graphene reinforcement. (**b.**) The evolution of Compressive Strength (f_c) as a function of time, with the same comparison as in (**a.**), all data points are an average of 4 cubes.

Upon increasing the stress above the elastic region, a gradual decrease in the slope of the stress–strain curve is observed. This is the plastic deformation region where the bonds between cement and aggregates still undergo a period of strain hardening, but with non-reversible changes. These effects are due to the viscous flow of hydrated cement paste in concrete, as well as to the propagation and growth of initial micro-cracks[28]. Also in this region we observe a similar behaviour to the elastic one, where graphene reinforced concrete is stiffer than standard concrete. When the stress is increased closer to the peak point on the stress–strain curve, internal cracks speed

their propagation, and the specimen is about to fail. In Fig. 5.2b it is evident that f_c of graphene reinforced concrete has higher values than standard concrete whereas graphite reinforcement lowers the f_c of standard concrete. Fig. 5.2b is a plot of f_c as a function of curing time, where each data point is an average of 3 cubes. 7 days after curing an 18.6% increase in strength is observed for FG reinforcement and 14.3% increase with IG reinforcement, compared to the standard concrete.

The results presented above provide a clear and strong evidence that the addition of graphene has a positive impact on the hydration reaction and does indeed increase the compressive strength of normal concrete. To further investigate how f_c evolves with varying concentration of graphene a systematic study of the stress-strain curve for a wide range of graphene concentrations was performed. Fig.5.3 shows a range of concentration from 0 (TW) up to 0.25%L, indicating that there is a threshold of increased f_c at around 0.05%.

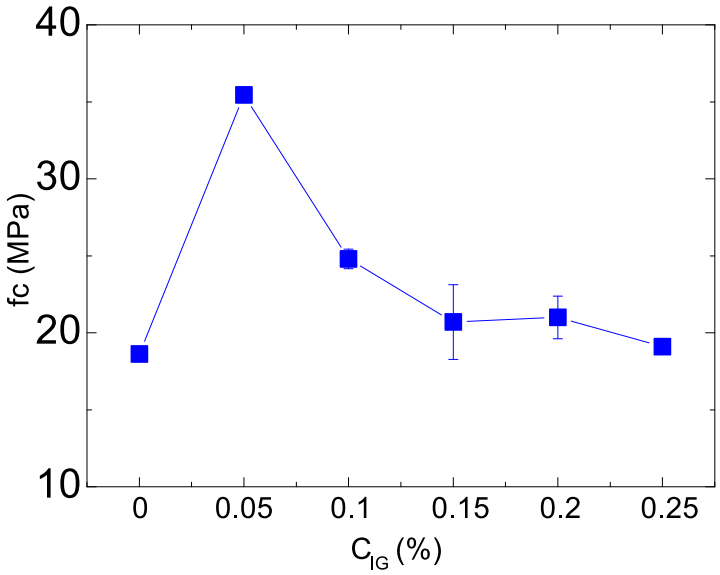

Figure 5.3: Investigation of IG concentrations, ranging from 0 to 0.25% as a volume of cement weight, and their amount of reinforcement to the f_c of concrete.

The next step was to further narrow down the range and find the optimal graphene concentration. Fig.5.4 plots the range between 0 and 0.05%, showing that the best performance with a

146% increase in compressive strength is with the addition of 0.04% of IG solution (graphene as a fraction volume of cement).

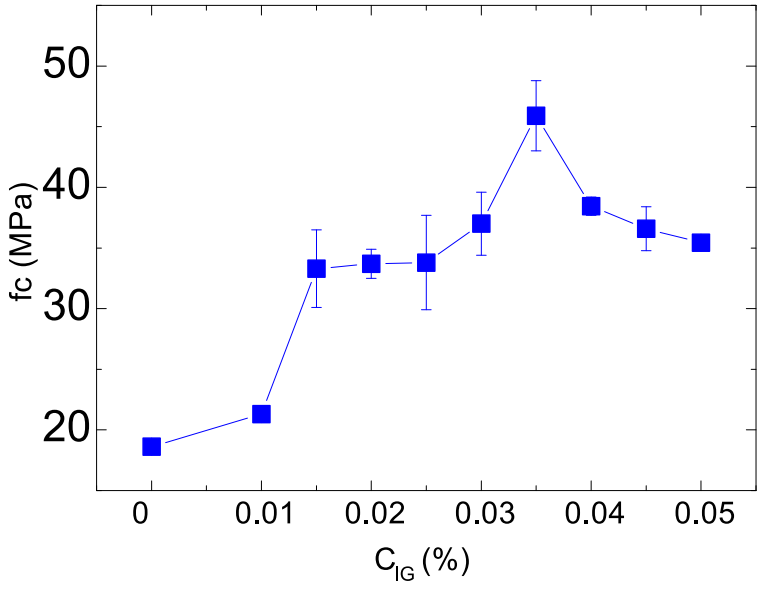

Figure 5.4: Investigation of the narrowed range of IG concentrations on the f_c of concrete, plotted as volume of cement.

These studies demonstrate that reinforcing concrete with graphene, has significant impact on increasing the early age compressive strength of concrete. With increasing the curing time to 14, 21 and 28 days, the strength of all the samples continues to increase, with graphene reinforced concrete remaining stronger than standard concrete. In particular the testing performed after 28 days of curing reveals that reinforcement with IG results in about 26% stronger concrete than the standard concrete, demonstrating the possibility of later age reinforcement of concrete with graphene.

Another study was performed to better understand the relationship between f_c and lateral size of graphene flakes. Since the number of layers for IG and FG were clearly identified with the Raman spectroscopy it was made clear that having between 4-8 layers is not sufficient whilst the optimal is 10-15 layers per flake. For the lateral size study, two new graphene powders were

provided from Graphene Supermarket (GS) and US Research Nanomaterials (RN). For clarity, FG has lateral size of about $1\mu m$, IG about $2\mu m$, RN and GS have $5\mu m$ and $8\mu m$ respectively. Fig.5.5 shows the relationship between f_c and the increasing lateral size of graphene dispersions, showing that IG is the optimal.

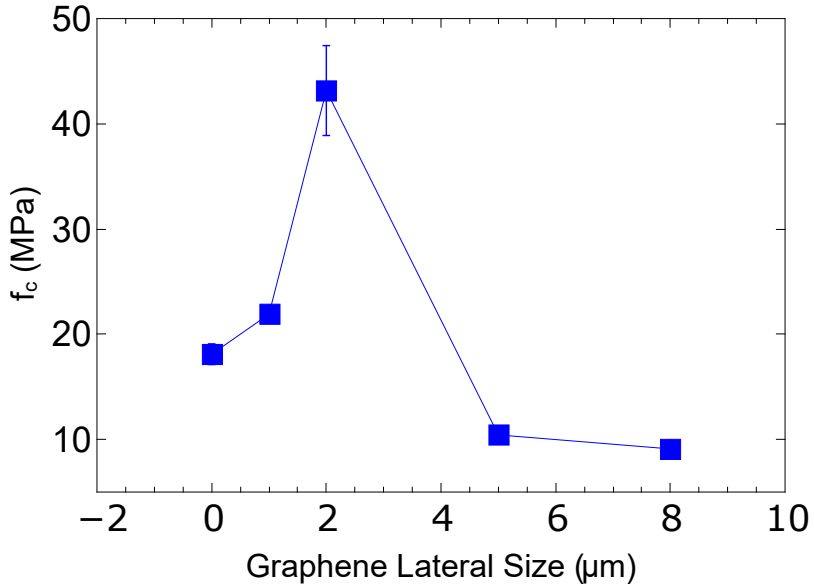

Figure 5.5: Investigation of the effect of lateral size of graphene dispersions on the f_c of concrete.

To further confirm that graphene reinforces concrete, statistical studies were performed by preparing and testing more than 150 concrete cubes. This included batches of 20 samples for each of the 3 experimental groups (Standard Concrete, $0.59g/L$ FG and $0.7g/L$ IG), all of which tested for compressive strength after 7 days and 28 days of curing. Fig. 5.6a and 5.6b show the statistical study of E_c, whereas Fig. 5.6c and 5.6d show the study of f_c, after curing for 7 and 28 days respectively. These studies confirm the measurements reported in Fig. 5.2a and 5.2b and support the conclusion that incorporation of graphene into the concrete matrix increases the compressive strength of both the early and later age concrete.

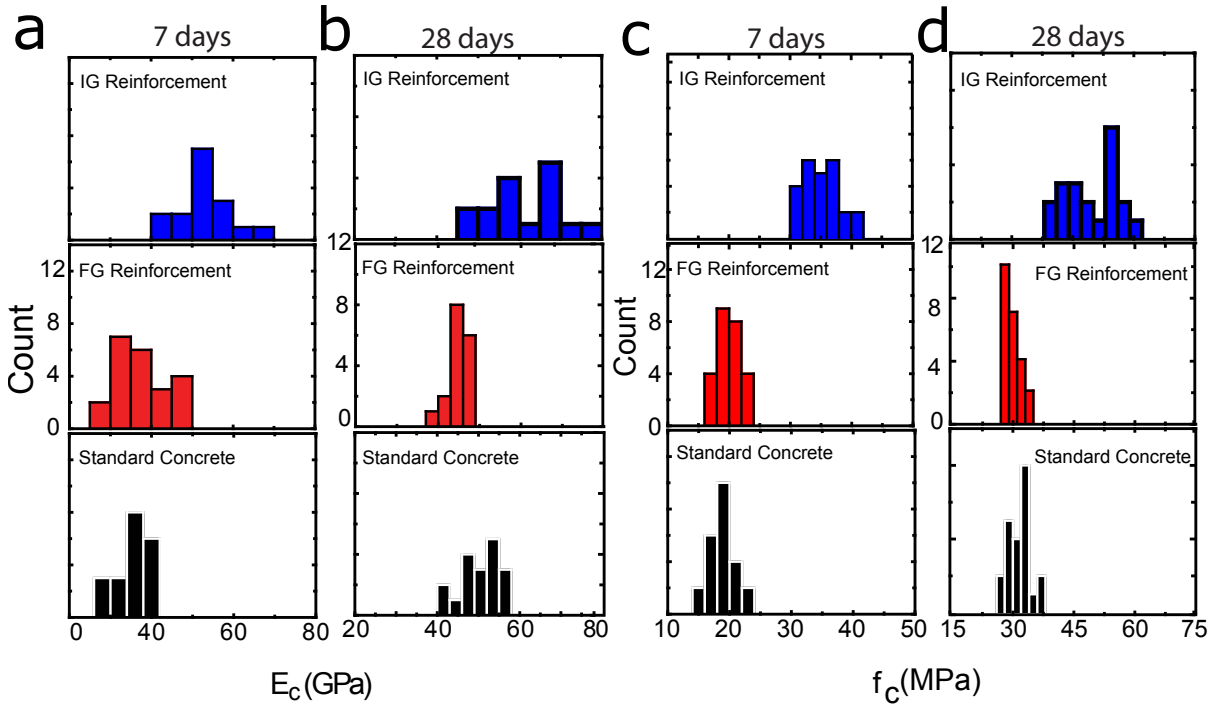

Figure 5.6: (**a.**) Statistical study on Young's modulus of the material (E_c) after 7 days and (**b.**) after 28 days of 0.7 g/L IG, FG and standard concrete experimental groups. (**c.**) The same statistical study of the compressive strength (f_c) after 7 days and (**d.**) after 28 days.

CYCLIC LOADING ANALYSIS

Upon proving statistically that graphene does have a huge impact on the compressive strength of concrete, the next step to was to investigate the long-term durability of the material. A common way to perform these measurements is via cyclic loading compression tests, which apply cyclic pressure on a sample within a given range. The purpose of this experiment is to investigate the internal dislocations, revealed by measuring the change in vertical displacement, and to observe any crack formation, if any. It is important to understand if this novel reinforcement ensures concrete's long-term serviceability because the construction material has to withstand dynamic loading for long periods of time.

For this experiment I chose to perform cyclic loading compression tests, measuring the stress–strain curve for 5 loops of loading and unloading up to 60% of the f_c. This particular range covers the elastic portion of the stress–strain curve (also known as the $F-\delta$ curve, and for this notation the difference between displacement and strain is ignored due to scaling factor of 10, related to the sample's dimensions) and is very important because during this phase the concrete experiences reversible deformations. Fig. 5.7a is a plot $(F-\delta)$ focusing on the maximum vertical displacement, measured directly from the mechanical strain gauge apparatus, of one sample after each cycle loading. Again, the main purpose is to compare concrete mixed with tap water to graphene reinforced one.

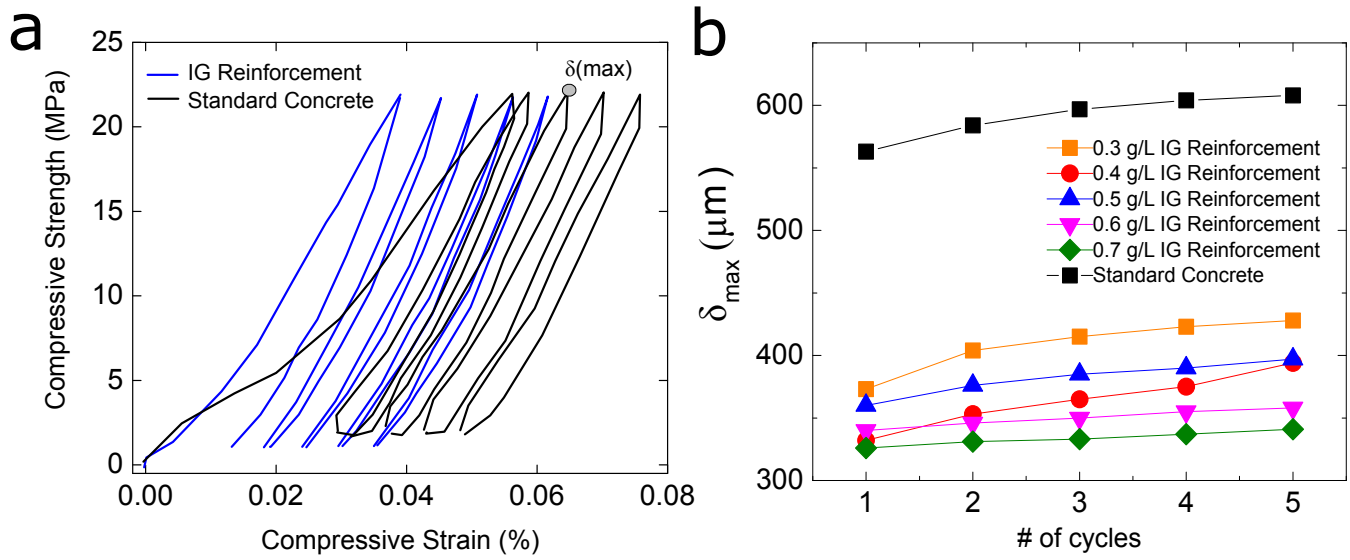

Figure 5.7: (**a.**) Measurement showing typical stress—-strain relationship of cycling loading compressive tests on a concrete cube. The loops have been spaced out by $\Delta(100\mu m)$ for better reading and the maximum displacement (δ_{max}) of each loop has been highlighted in red. (**b.**) Comparison of the maximum displacement under compressive cycling loading for reinforced cubes with increasing graphene concentration.

Fig. 5.7a shows that even after multiple loading-unloading patterns the graphene reinforced samples do not experience as much internal deformation as standard concrete. The loops have

been spaced out by a constant value for visual simplicity. As shown in Fig. 5.7b, the overall δ_{max} of the concrete decreases with increasing the concentration of graphene indicating stronger molecular bonds as concrete is being progressively reinforced.

Next, I focused on the first loop of the $F - \delta$ plot to study the maximum plastic strain ϵ_{pl}. The method derived by Mander et al[33] was used to calculate ϵ_{pl} – it lies on the secant line of the unloading curve (the black line) of the loop, as shown on Fig. 5.8a.

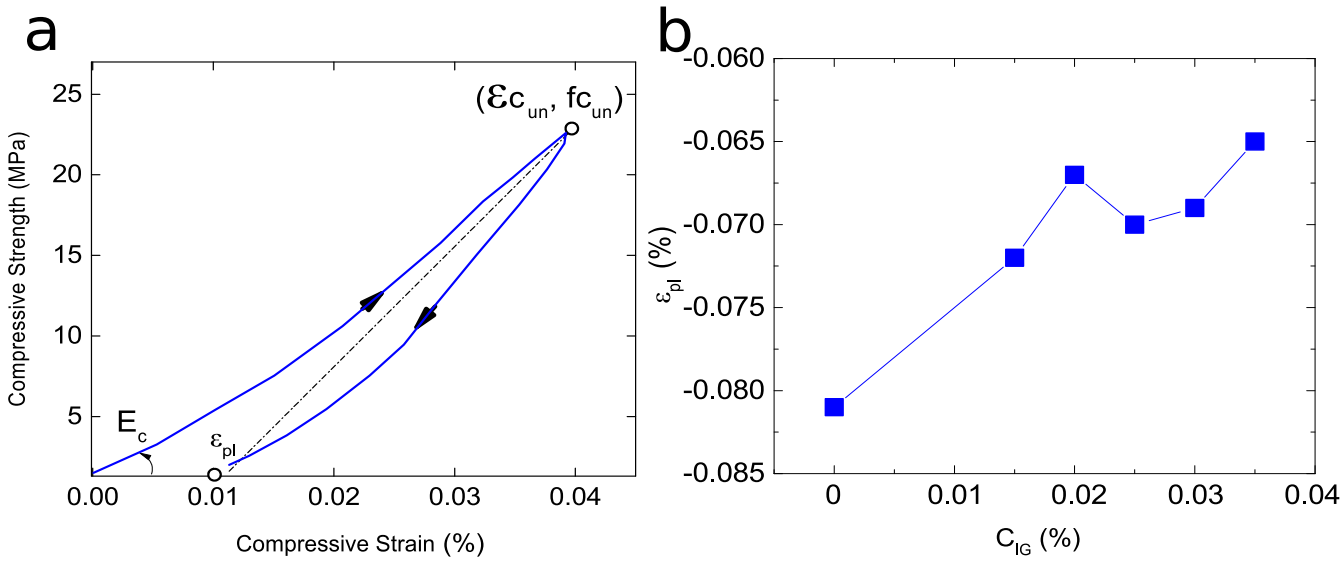

Figure 5.8: (**a.**) The first loop of the cyclic loading measurement is extracted to study the unloading curve. The maximum plastic strain is calculated from the secant line of the unloading curve. (**b.**) The evolution of the plastic strain as a function of increased graphene concentration in the reinforced concrete samples.

The plastic strain indicates the residual deformation when the applied stresses are removed. As it can be seen from Fig. 5.8b, for the whole range of graphene concentrations the reinforcement helps to decrease the ϵ_{pl} when compared to standard concrete (i.e. C_{IG}=0) which is in agreement with overall increase in f_c and E_c.

FLEXURAL STRENGTH

After having established that graphene reinforcement increases the compressive strength of concrete, next in line to study is the second most important mechanical property of concrete – flexural strength (f_{cr}) and the corresponding flexural modulus (E_{cr}). As discussed in Chapter 3, beams were prepared for standard concrete and for different IG concentrations, then tested after 7 and after 28 days of curing. Fig. 5.9 shows a typical stress–strain curve obtained from three point bending tests, where the mid-span deflection δ is measured using displacement transducer in order to give better understanding of E_{cr}.

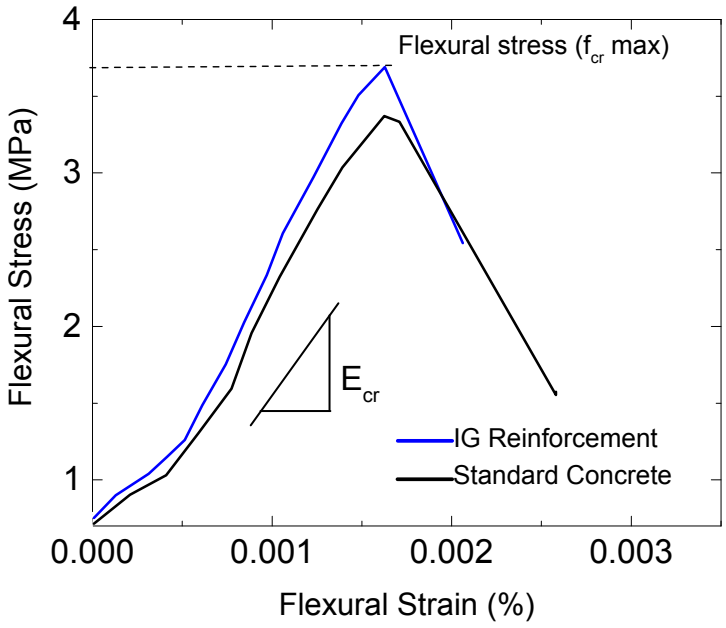

Figure 5.9: (**a.**) Typical stress-—strain curve under flexural loading showing the maximum flexural stress and strain f_{cr} of both the standard concrete and the graphene reinforced one (IG)

The maximum f_{cr}, under a load in a three-point bending test, is calculated using the following the equation:

$$f_{cr} = \frac{3FL}{2bd^2} \tag{5.1}$$

using the maximum force applied, found at the top of the $F - \delta$ curve, which then leads to complete irreversible deformation, similarly to compressive strength tests. Similarly to the compressive modulus of elasticity the flexural one is also dependent on the slope of the tangent line of the first 50% of the $F - \delta$ curve, however it includes the second moment of area too. From basic beam theory the mid-span deflection ω_0 is given by:

$$\omega_0 = \frac{PL^3}{48E_{cr}I} \tag{5.2}$$

where L is the distance between the two outter supports, P is the load applied at the middle of the beam, and I is the second moment of area defined by:

$$I = \frac{a^3b}{12} \tag{5.3}$$

having a and b the cross-sectional dimensions of the beam. E_{cr} can then be readily calculated using the slope of the stress-strain curve and measured displacement:

$$E_{cr} = \frac{dPL^3}{d\omega_0 48I} \tag{5.4}$$

Fig. 5.10a and 5.10b show the E_{cr} and f_{cr} of standard concrete and IG reinforced concrete beams after 7 days of curing. Clearly as the graphene concentration is increased both properties are improved, showing maximum increase with IG concentration of 0.03% – 21.8% and 18.6% for E_{cr} and f_{cr} respectively. 28 days after specimen curing the mechanical improvement is still present with 78.5% increase in E_{cr} and 79% for f_{cr} as shown on Fig. 5.10c and 5.10d for the same IG

concentration. This massive increase in flexural modulus and strength are in agreement with the increase of maximum f_c and decrease of compressive δ_{max} shown in previous figures.

DISCUSSION ON INCREASED f_c AND f_{cr}

The observed strengthening of concrete by incorporation of graphene can be interpreted in terms of the modification of cement hydration reaction. To understand the details of our discussion, it is important to recall some basic aspects of this reaction and relevant properties of graphene. Upon reacting with water molecules, the cement micro-crystalline powder undergoes physical transformations to fibrous crystals containing mainly calcium silicates, alumino-ferrites and calcium hydroxide ($Ca(OH)_2$). More than 40 variations of silicate crystals have been reported to occur in the composition of cement[68]and they form the calcium silicate hydrate (C-S-H) gel, which is one of the main elements responsible for the mechanical properties of concrete. Graphene monolayers and few-layers have large specific surface area and high Young's modulus (E around 2 TPa[44]). As it has already been demonstrated, graphene interacts with various elements forming the vast elements C-S-H groups[68] and alters the morphology of the hydration crystals[73]. In particular, due to the high surface energy of graphene, C-S-H particles bond to graphene and act as nucleation sites, promoting the growth of C-S-H gels along the graphene flakes. This process leads to an increase in the bond strength of cement[23].

As we have demonstrated in Fig. 3, the defects found in my graphene materials are only due to boundaries of the flakes. Therefore the defect–free basal plane of my graphene material forms an ideal platform for the growth of C-S-H crystals with higher degree of crystallinity than the crystals occurring in standard concrete. The degree of crystallinity is one of the most important physical parameters responsible for the mechanical properties of a material and determines various parameters, such as the Young's modulus and strength. Furthermore, combining C-S-H which has

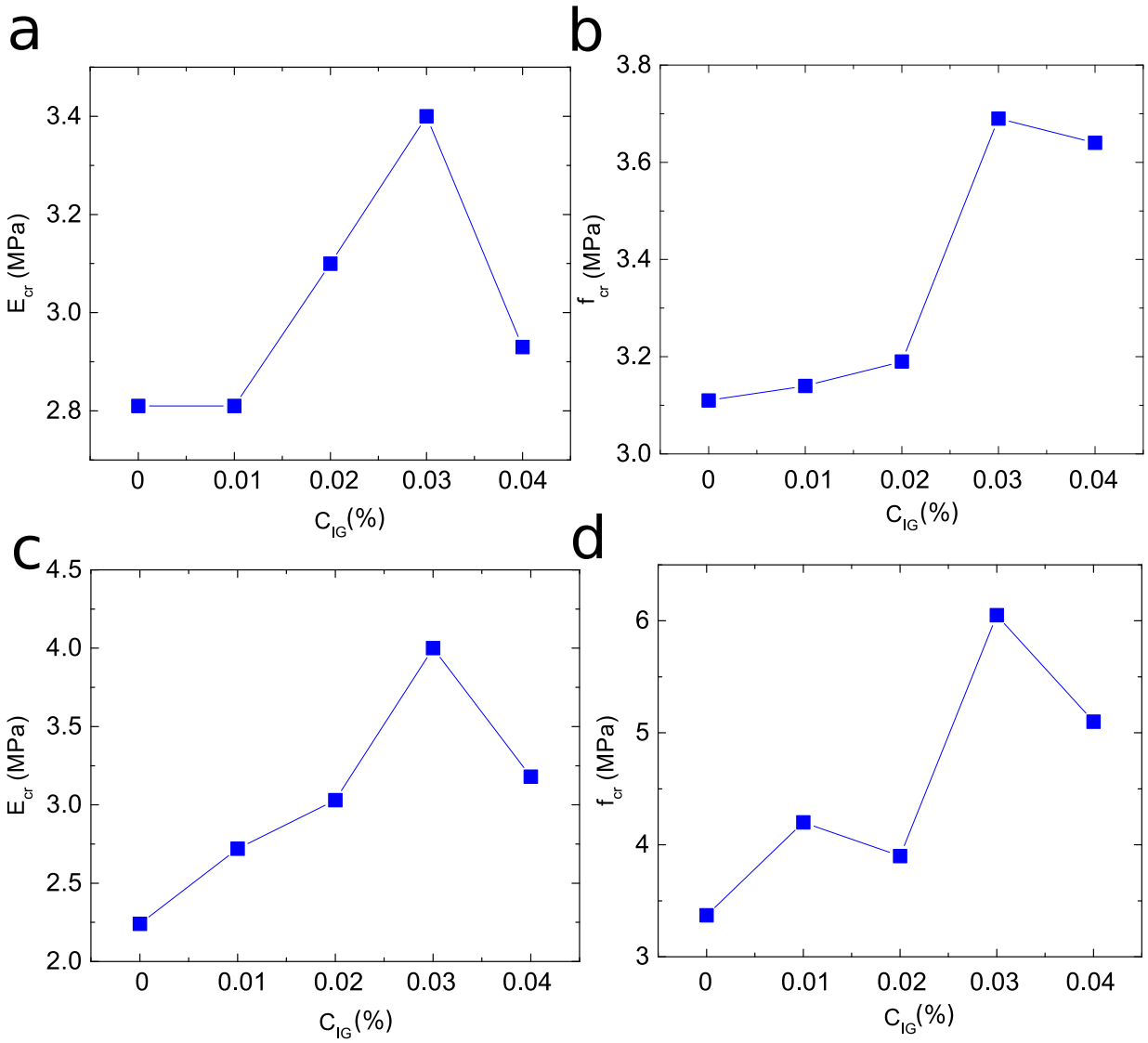

Figure 5.10: (**a.**) Evolution of early age flexural modulus (E_{cr}) with increasing graphene concentration C_{IG} in IG reinforced concrete. (**b.**) Evolution of late age flexural modulus (E_{cr}) with increasing graphene concentration C_{IG} in IG reinforced concrete. (**c.**) Evolution of early age flexural strength f_{cr} with increasing graphene concentration C_{IG} in IG reinforced concrete. (**d.**) Evolution of late age flexural strength f_{cr} with increasing graphene concentration C_{IG} in IG reinforced concrete.

an E of 23.8 GPa[78] with graphene (E of 2 TPa) would lead to a considerable increase in the E_c and E_{cr} of the composite material. Therefore, it is strongly implied that the possible formation of C-S-H crystals along the graphene flakes with high degree of crystallinity combined with the high Young's modulus of graphene could lead to a stiffer graphene–C-S-H composite material than C-S-H alone, as observed experimentally.

Another factor which determines the compressive strength of concrete is the degree of porosity, which results in empty voids within the cement paste due to unhydrated crystals or leaching of $Ca(OH)_2$. $Ca(OH)_2$ crystals tend to form on a nano-scale level and due to their high solubility, leach out when concrete is exposed to fresh water. This process increases the porosity of concrete and therefore, decreases its strength. We believe that graphene reinforcement could also have an effect on decreasing the degree of porosity. Indeed previous studies have shown that the microstructure of cement paste is finer and denser with the inclusion of graphene oxide sheets, resulting in an enhancement of its strength and durability[59].

CONCLUSIONS

In conclusion I investigated the evolution of both compressive and flexural strength, with their corresponding modulus of elasticity. The purpose of this research to was compare normal concrete to graphene reinforced one. I found that graphene increases all of the parameters – f_c, E_c, f_{cr} and E_{cr} both in the early and late stages of hydration. Firstly, I performed a statistical analysis of compressive strength and modulus to confirm the reinforcement and argue against any comments saying that average of 3 samples in the $f_c - time$ (Fig.5.2b) relationship is not enough to derive conclusions. Then I studied the long-term durability of the reinforced concrete, as well as its plastic modulus during unloading of pressure. In all experimental data it is clear that graphene enhances the bonding between cement crystals, improves their mechanical interlocking and this all

results in a stiffer matrix able to withstand significantly larger loadings. Secondly, I studied the effect of graphene on the flexural strength and modulus and showed that there is a upper threshold of C_{IG} which may hamper the reinforcement. The results presented in this chapter provide clear evidence that graphene improves the fundamental properties of concrete, opening novel avenues for fighting against global warming by decreasing the cement production and CO_2 emissions.

6

NONLINEAR FRACTURE MECHANICS ANALYSIS OF NOTCHED CONCRETE BEAMS

INTRODUCTION

In the last Chapter I presented an in-depth analysis of the two most fundamental properties of concrete – its compressive and flexural strengths, as a result of the incorporation of graphene. There are many more research areas and industrial applications of concrete and its allotropes. In this chapter I focus on another very important aspect of evaluating the novel construction material, thus, studying its nonlinear, quasi-brittle fracture mechanics and the formation of cracks due to constantly increased loading.

The study of fracture mechanics in composite brittle materials is quite complex and interesting, as compared to fracture in pure brittle atomic matrices like glass, because the applied loading on a matrix composed of various elements, glued together, accumulates and stores internal energy for a time period. This energy, most commonly referred to as fracture energy (G_f), reveals how strong

a material is – how likely is it to withstand internal dislocations, deformation, the consequential crack propagation and eventual complete failure. The interesting aspect of the fracture mechanics science, applied to concrete particularly, is the complexity of internal dislocations and slipping of planes, formed due the hydration of cement. One cannot predict or make direct observations of these dislocations and micro-crack propagations, that is why a computational analysis is needed. I I performed such analysis for the work in this chapter, which was particularly challenging. The aim of the work presented below is to compare tap water to graphene reinforced concrete, similarly to previous chapters, by evaluating a range of properties and parameters using software calculations.

The two important properties – long term durability and crack resistance of concrete, are investigated by applying two fundamental approaches of nonlinear fracture mechanics principles (NFMP). In this chapter I study and evaluate numerically the energy required to propagate a crack (G_f), its critical length (a_c) and the consequent stress intensity at the fracture process zone (FPZ), which is defined as the area at the tip of a crack. This analysis reveals important information about the material's ability to resist loading, ductility behaviour and crack formation within the internal composite matrix both in the elastic and plastic regions of the stress-elongation curve (F-δ). The first NFMP approach is based on the fictitious crack model (FCM) developed by Hillerborg[69] within the boundary element method, which focuses on the fracture energy (G_f) and characteristic length (l_{ch}) of brittleness[63]. The second approach of NFMP is based on the modified linear elastic fracture mechanics (LEFM) and focuses on estimating the critical stress intensity factor (K^e_{IC}) and on the combination between stable and unstable fracture energies, more commonly known as double–G fracture parameters. All of these calculated values reveal information and by studying them carefully one can predict the energy release rates during concrete loading.

EXPERIMENTAL DETAILS

For the experimental work in this chapter I prepared graphene solutions (IG) using industrial graphene powder, as described in earlier chapter. The tested samples were notched beams. All concrete batches had 1:2:3 ratio of cement, sand and coarse aggregate and w/c ratio of 0.5. No dispersing agents or other chemical additives were used. The batches were mixed for $10mins$ in a standard concrete mixer, cast in $100\times100\times400mm$ steel moulds and shaken for $10mins$ on vibration machine to avoid air entrapment. A notch was created at the midspan with plastic plate, creating a notch-to-depth ratio of $a_0/a = 4$. The ratio was kept the same for all experimental groups. The samples were cured in water for 7 and 28 days respectively, then dried at room temperature (20°) for $24h$ prior to flexural tests. Fig. 6.1a shows the schematic of notched beam where L is the length of beam ($400mm$), S is the span between supports ($360mm$), F is applied force ($100N/s$), a is beam depth ($100mm$), b is beam width ($100mm$) and a_0 is notch depth ($25mm$). Flexural strength (f_{cr}) and flexural modulus (E_c) were obtained from 3-point bending tests on concrete specimens with dimensions $100\times100\times400mm$. Fig. 6.1b shows a photograph of a beam after failure under 3-point bending test.

In order to determine fracture parameters of normal and reinforced concrete, two series of tests were performed on notched beams. Standard vertical displacement transducer (VDT) was used to record the deflection at mid span of the beam. Standard 3-point bending apparatus, provided by Controls group, was used to perform all experiments with constant loading speed of $100N/s$. Compressive strength (f_c) and compressive modulus of elasticity E_c were determined by tests on cubes with dimensions $100\times100\times100mm$ as per BS EN 12390. All values presented in Table 6.1 and 6.2 are an average of three tested samples. Split tensile strength (f_{ct}) was calculated based on experimental results from tests on cylinders with length of $150mm$ and diameter $100mm$.

Fig.6.1c shows representative data of one sample tested both for standard and reinforced

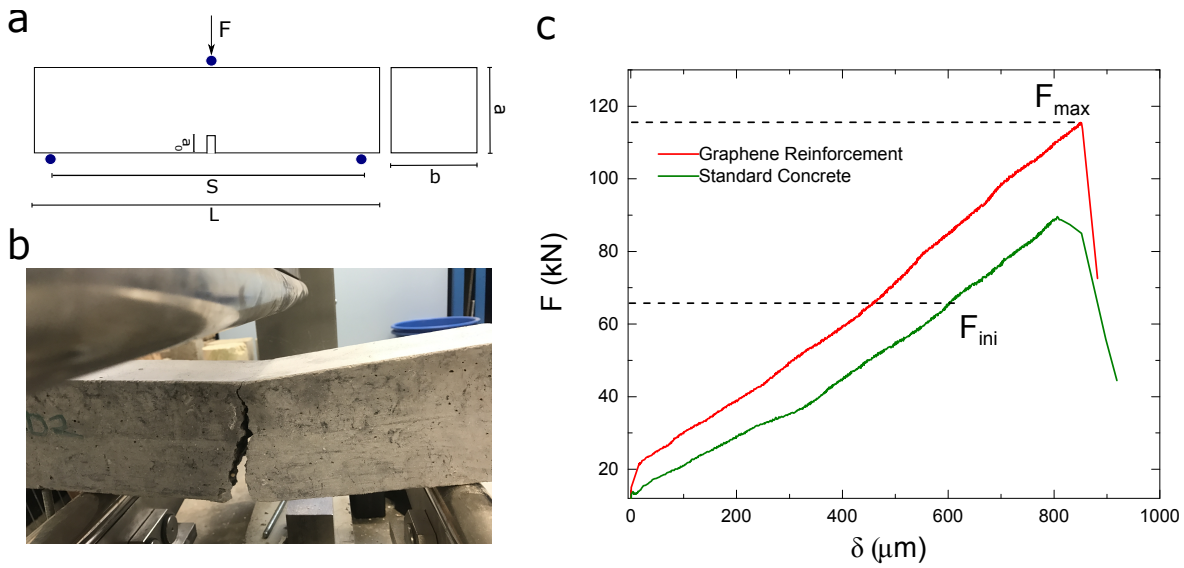

Figure 6.1: a) Schematic of concrete notched beam used for testing. b) Notched beam after failure under three point bending test. c) Force-displacement (F-δ) curve showing results from flexural testing and comparing representative samples of GRC to SC experimental groups.

concrete after 7 days of curing. F_{max} and F_{ini} are shown as the maximum force applied and 60% of its value, respectively. They are both used in calculating parameters throughout this chapter. The modulus of elasticity is calculated as the slope of the line up to 60% portion of the elastic region of the curve, similarly to calculations from Chapter 5. As it can be seen clearly, the incorporation of graphene dispersions increases the flexural strength of a concrete beam significantly. Consequently, all of the fracture parameters are also enhanced, as shown later in this chapter.

Prior to the analysis of both methods, the data used for calculations is presented below. Table 6.1 shows data for samples tested after 7 days of hydration and similarly Table 6.2 shows data for specimens left to cure in water for 28 days. The convention of parameters for both tables is the same – Graphene (g/L) is the amount of graphene in solutions, $f_c(MPa)$ is the compressive strength, $E_c(GPa)$ is the compressive modulus, f_t (MPa) is the tensile strength, $f_{ct}(MPa)$ is the split tensile strength, $F_{max}(N)$ is the maximum force applied on the beam during flexural tests.

Table 6.1: Values used for analysis of results after 7 days of sample hydration.

C_{IG} (g/L)	$f_c(MPa)$	$E_c(GPa)$	f_t (MPa)	$f_{ct}(MPa)$	$F_{max}(N)$
0	18.63	36.2	3.11	2.66	5185
0.2	21.3	46.5	3.14	2.36	5234
0.4	33.7	56.17	3.19	2.95	5312
0.6	37	56.68	3.69	3.95	6150
0.8	38.1	65.7	3.64	3.46	6074

Table 6.2: Values used for analysis of results after 28 days of sample hydration.

C_{IG} (g/L)	$f_c(MPa)$	$E_c(GPa)$	f_t (MPa)	$f_{ct}(MPa)$	$F_{max}(N)$
0	30.4	42.6	3.37	3.8	5619
0.2	38.3	56.6	4.2	4.19	6898
0.4	47.6	51	3.9	3.86	6513
0.6	51.5	60	6.05	4.9	10080
0.8	45	44	5.1	4.61	8475

RESULTS FROM THE FICTITIOUS CRACK METHOD

Based on the fictitious crack model by Hillerborg[69], which examines the formation of crack surfaces and the corresponding fracture process zone (FPZ) at the tip of the initial length of the crack, fracture energy calculations use data from the force–displacement (F-δ) curve of typical 3-point bending test. An example curves of both SC and GRC are shown on Fig. 6.1c. From the F-δ curve in Fig. 6.1c, G_f can be calculated using the following equation[63]:

$$G_f = \left[\int_0^{\delta_{max}} F(\delta) d\delta + mg(\delta_{max}/2) \right] / \left[(d - a_0) b \right]$$

where $\int_0^{\delta_{max}} \mathrm{F}(\delta)$ is the area under the curve, m is weight of the beam, g = 9.81 m/s^2 – mg is a correction for the energy supplied by the weight of the beam, d is depth of the beam, a_0 is notch length and b is the beam width.

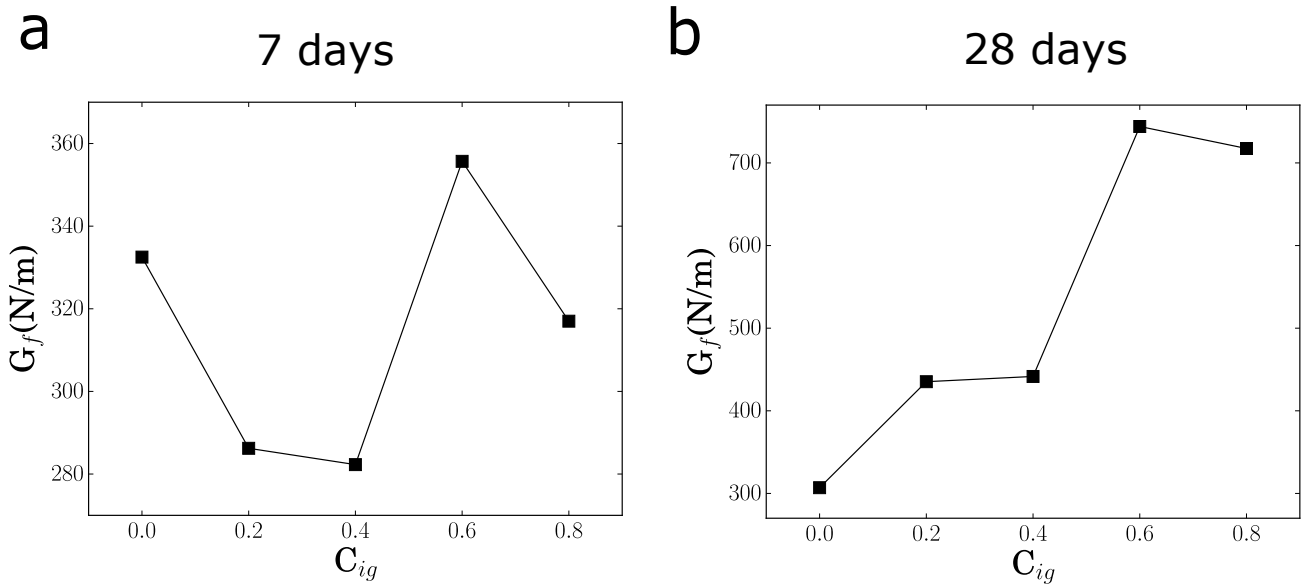

Figure 6.2: (**a.**) The Fracture Energy G_f dependency as a function of increasing graphene concentration after 7 days of sample curing and similarly (**b.**) after 28 days.

As mentioned before, G_f of concrete is the energy required to create a crack per unit length. The experiments were performed after 7 and 28 days of curing to better understand the long-term durability and of the material and hydration effect on G_f. First, the early-age (7 days) results show that even though the graphene reinforcement increases the compressive strength significantly it does not have an immediate effect on G_f. Fig. 6.2a shows the evolution of G_f as a function of increasing graphene concentration and the values for G_f are similar to the standard concrete sample, ranging from 280 up to $360 N/m$. The bonds within the internal matrix, more specifically

the FPZ, have not yet been affected by the graphene incorporation. Small concentrations of graphene have not yet enhanced enough the nucleation sites of the cement hydration crystals to resist plane slipping under tensile loading. An increase in G_f is noticed when ratio of $0.6g/L$ is used. A significant difference in the values of G_f is observed on samples hydrated for 28 days. Fig. 6.2b shows a linear increase of G_f with increasing graphene concentration. The fracture energy of standard concrete is $307N/m$ while the addition of $0.8g/L$ of graphene increases it by 134% up to $720N/m$. The huge increase of G_f indicates that the internal mechanical interlocking of cement crystals is strengthened by the incorporation of graphene flakes. Furthermore, the increase in G_f suggests that % of air voids and microcracks ahead of the FPZ is also decreased due to nano-modification of the hydration reaction at its early stages. The internal bonds between cement and aggregates are clearly much stronger when reinforced with graphene since the FPZ needs much more energy to form a crack.

The l_{ch}, which is the second important parameter investigated by the FCM is expressed as:

$$l_{ch} = \frac{G_f E_c}{f_t^2}$$

This parameter calculated with the FCM and again, values of SC are compared to GRC after 7 and 28 days of specimen hydration. Fig. 6.3a shows that the l_{ch} for SC is increased from $1244mm$ to $1572mm$, showing 26% increase with graphene reinforcement at the early stage of the hydration process. For late-stage curing this difference is tripled – Fig. 6.3b shows 79% increase in ductility with the addition of $0.8g/L$ of graphene. The results from Fig. 6.3 indicate decreased brittleness of graphene reinforced concrete, thus having longer durability during structural vibrations and cycling loading.

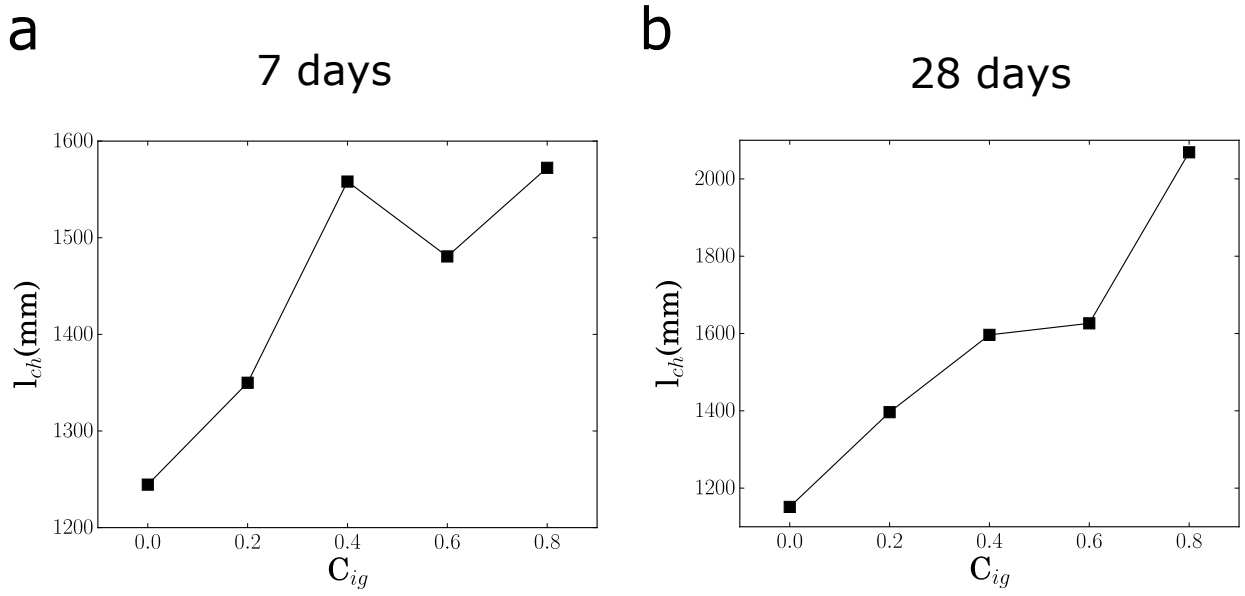

Figure 6.3: (**a.**) The critical crack length l_{ch} dependency as a function of increasing graphene concentration after 7 days of sample curing and similarly (**b.**) after 28 days.

RESULTS FROM THE EFFECTIVE CRACK METHOD

The main purpose of evaluating the propagation of cracks in concrete fracture using ECM is to calculate values for the critical crack length a_c and then for K^e_{IC}. These parameters are very important for evaluating structural design because the fracture in real concrete structures sets in when K^e_{IC} becomes critical. K^e_{IC} is dependent on the nominal tensile stress, a_c and a geometrical factor, as discussed earlier. Fig. 6.4 presents the calculated values for K^e_{IC}, comparing SC to various graphene reinforcements both at 7 and 28 days after curing. Both Fig. 6.4a and b show that the critical stress intensity factor increases linearly with increasing graphene concentration. Similarly to the values for G_f the significant improvement is seen at late stage hydration where K^e_{IC} increases by 79%, from $0.54 MPam^{\frac{1}{2}}$ for normal concrete to $0.98 MPam^{\frac{1}{2}}$ for $0.8 g/L$ graphene

reinforcement. This remarkable improvement shows that by nano-modifying cement, concrete's critical point of failure can be greatly extended. This is in agreement with the more ductile behaviour concluded from calculations in Fig. 6.3.

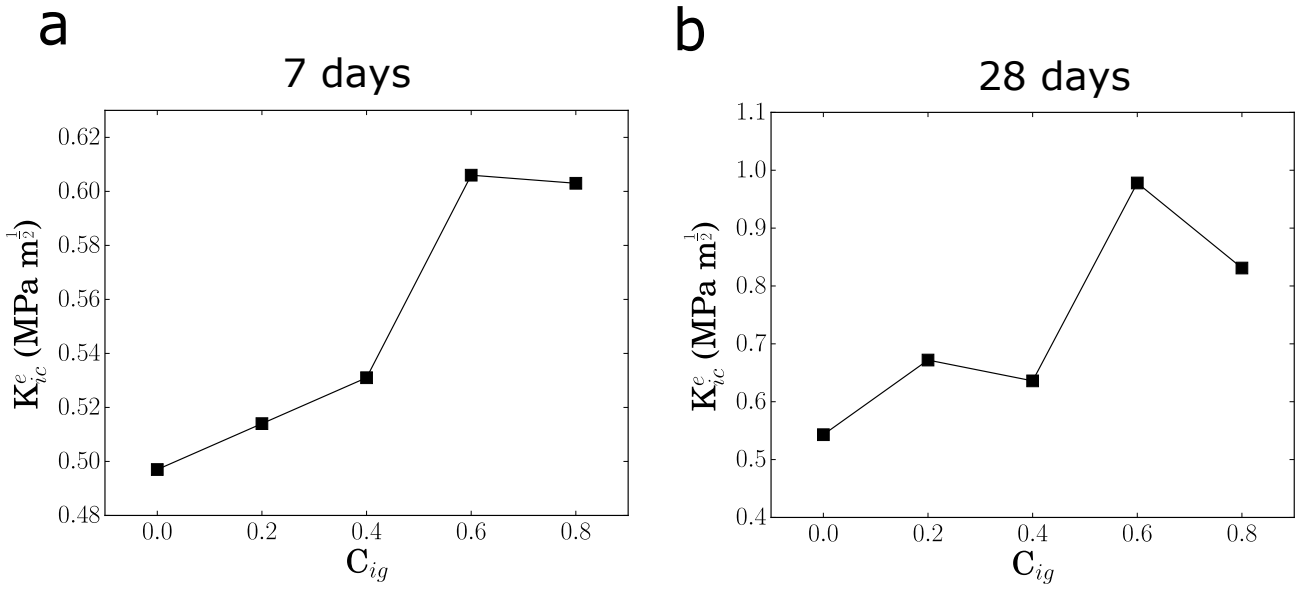

Figure 6.4: (**a.**) The K^e_{ic} dependency as a function of increasing graphene concentration after 7 days of sample curing and similarly (**b.**) after 28 days.

OBTAINING THE DOUBLE-G FRACTURE PARAMETERS

The double-G fracture parameter (DGFM) model by Xu and Zhang[86] analyses the crack propagation in concrete beam specimens under tensile loading, based on the energy release rate approach and includes the ductility properties. So far we have analysed fracture energy, level of brittleness and critical stress intensity factor for both SC and GRC, now this section will analyse the unstable fracture energy G^{un}_{IC} and the corresponding K^{un}_{IC}. Samples, as in previous analysis, were tested

both after 7 and 28 days of hydration. Fig. 6.5a presents data for G_{IC}^{un} after 7 days of hydration. Similarly to the results of Fig. 6.5 the unstable fracture energy for both SC and GRC samples is relatively similar, of $6.5N/m$ and $6N/m$ respectively. The K_{IC}^{un} values are mainly dependant on the E_c of the material and that is why we see almost linear increase in values, going from $15.5kNm^{-\frac{3}{2}}$ for standard concrete up to $18.5kNm^{-\frac{3}{2}}$ for $0.8g/L$ reinforcement. Fig. 6.5b shows the same relationship for both parameters after 28 days of hydration. The G_{IC}^{un} increases by 124% from $5N/m$ for standard concrete to $11.2N/m$ for graphene reinforced one. The K_{IC}^{un} values also show almost double increase, from $16.7kNm^{-\frac{3}{2}}$ to $29.94kNm^{-\frac{3}{2}}$ totalling of 79%. These results indicate that the graphene reinforcement leads to stronger mechanical bonding between the cement hydration crystals. This can be confirmed by the larger amount of energy required to cause failure in the FPZ at the tip of the crack and increased overall fracture toughness. The results for G_{IC}^{ini} and K_{IC}^{ini} are not plotted since they depend on the F_{ini} which is proportional to F_{max}.

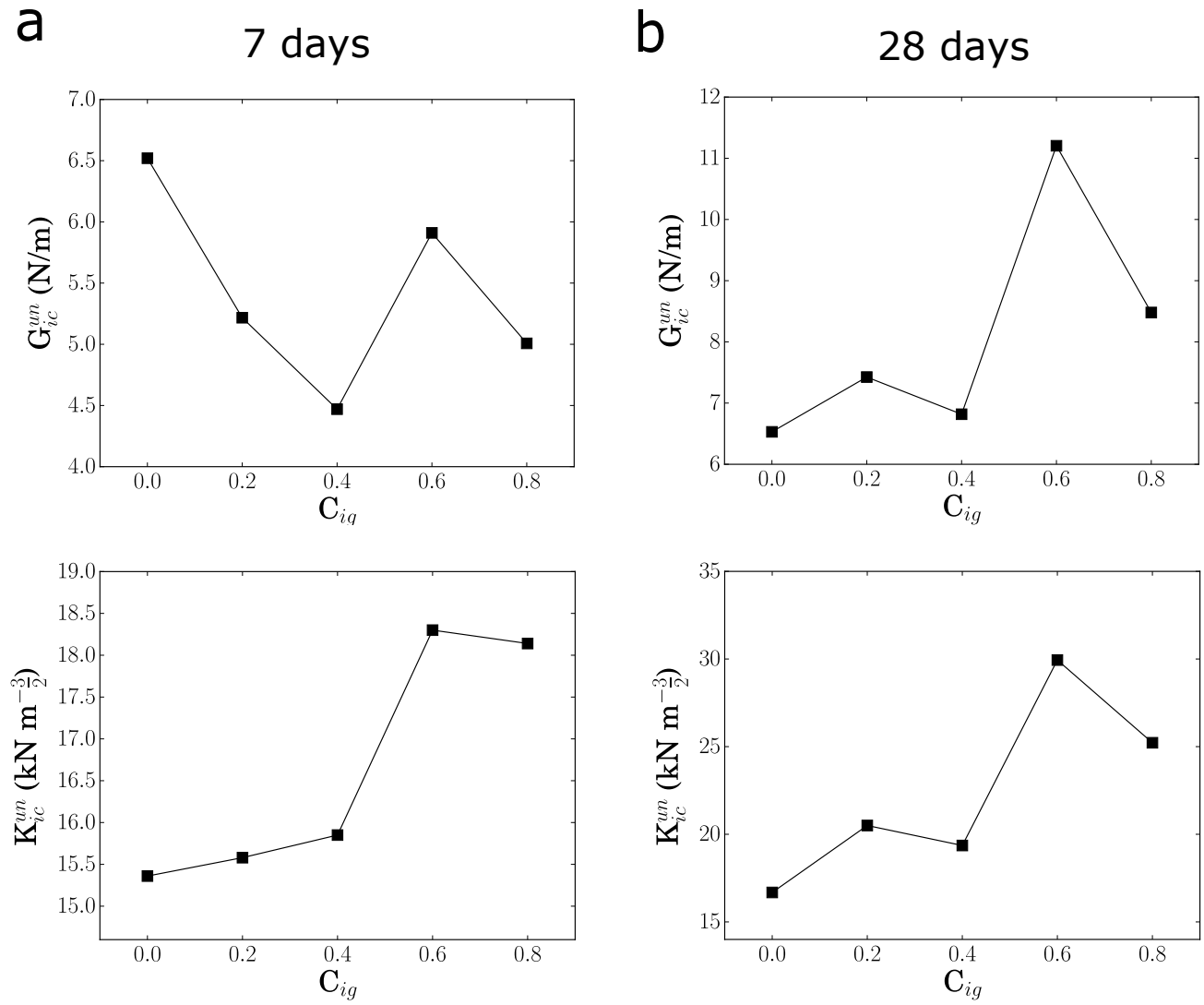

Figure 6.5: (**a.**) Results for Double fracture parameters G and K after 7 days of curing and similarly in (**b.**) after 28 days.

CONCLUSION

The novel results presented above clearly show that the incorporation of graphene nano-engineers and improves the conventional concrete resistance to flexural loading, crack formation and maximum point of failure. The huge increase in total fracture energy required to propagate a crack in GRC, as compared to SC, indicates that the hydration reaction is changed at its very early stages which results in improved mechanical interlocking of cementitious hydration crystals. Graphene's large surface area enhances the formation of nucleation sites and provides more rapid growth of cementitious crystals as well as strengthening the bond between cement and larger aggregate. A denser matrix with large load-bearing capacity is formed which increases the critical stress intensity and ductility of concrete specimens. The improved mechanical performance and decreased brittleness of the construction material are analysed through two different nonlinear fracture mechanics approaches for better understanding of its properties. Both approaches show consistant increase in all parameters such as G_f, l_{ch} and K^e_{IC}. Graphene nano-engineered concrete outperforms any other reinforcements[26;22;37;58] and paves the way for applications of nano-reinforced concrete materials in the construction industry.

Part III

Graphene-Cement Composites

7

MULTIFUNCTIONAL GRAPHENE-CEMENT BASED COMPOSITES

INTRODUCTION

The previous two chapters examined the fundamental mechanical properties of graphene reinforced concrete, including a complex computational analysis of its nonlinear fracture mechanics. Now its time to turn the reader's attention to the numerous other type of applications of the construction material. Since they are so versatile and cheap, cement-based materials have been used in roads, bridges, dam walls and at oil refineries at sea. Engineers use their multifunctional purposes for potential impermeability applications which can reduce internal damage of a structure, or for example act as an oil barrier, thus preventing sea pollution. In some parts of the globe where there is extensive snowfall or roads get iced due to extremely low temperatures, researchers are trying to create a "sandwich" type of road. This multistructure includes a layer on top of the standard asphalt which has electrical conductivity properties and therefore upon applied voltage can heat up and de-ice the road (melt snow as well). This approach can be used on helicopter landing pads, airports, highways etc. and needless to say, this innovation can save thousands of

lives by preventing car crashes. A more futuristic potential application of conductive cement-based materials in roads also include wireless charging of electric cars.

RELEVANT BACKGROUND WORK

Previous work was conducted on incorporating various materials to the cement matrix, aiming to improve other properties than conventional mechanical strength. Examples of such materials are carbon nanotubes (CNT)[7;75], graphene nanoplatelets(GNP)[7], graphite nanoplatelets[30], carbon fibers(CF)[7], hexagonal boron nitride[66] and graphene oxide[53;58]. Researchers mixed these materials, ranging from the nm to mm scale, with cement by different methods such as ball milling[66], ultrasonication[7], adding powders to the overall mix[30;7;84] and the lengthy Hummers' method[53;58] (which is a method used to oxidise graphite and produce graphite oxide. After that graphite oxide is exfoliated into graphene oxide used for the cited experiments). Their results show improvement in transport properties, oil barrier enhancement and improving electrical conductivity, however none of these papers show a truly promising method for large scale application. Moreover, their studies are performed on very small samples made from cement-only or mortar pastes and the process of addition of all fibers or nanomaterials is quite expensive.

A new perspective from graphene, directly exfoliated from pristine graphite through high-shear mixing, arises to cope with the problems mentioned above and truly make cement-based composite a multifunctional material. The most important difference lies in the improved cost-time relationship of production and huge scalability (more than $100L/h$). The results presented in the following sections show how graphene not only significantly improve the mechanical properties of concrete but also enhances the water impermeability, electrical conductivity and heat transfer properties. The intrinsic mechanical properties of the nanomaterial not only bond well with the cement crystals, but also serve as protective barrier against water infiltration. The ionic

drift among the hydration crystals allows for these composites to be electrically conductive. The increase in resistivity suggests a hindering effect that could be caused by graphene which prevents water ingress. This, in turn, means that the compound is depleted of ions that are responsible for drift current, resulting in a diminished conductivity.

WATER PERMEABILITY

To gain further understanding into the durability of concrete and in particular whether graphene reinforcement plays any critical role in enhancing it, I performed water permeability studies. In general, the durability of concrete depends on the capacity of a fluid to penetrate its microstructure. Degradation mechanisms of concrete often depend on whether water can penetrate into the concrete, possibly causing damage. To investigate the water permeability, I compared the water penetration in samples made of standard and IG reinforced concrete using the same IG concentrations to those presented in Chapters 5 and 6. The cylinders were left in water tank as indicated on Fig.7.1 for 7 days and each day the water level was remeasured. I marked the initial water level and compared it to the upward depth of penetration at the end.

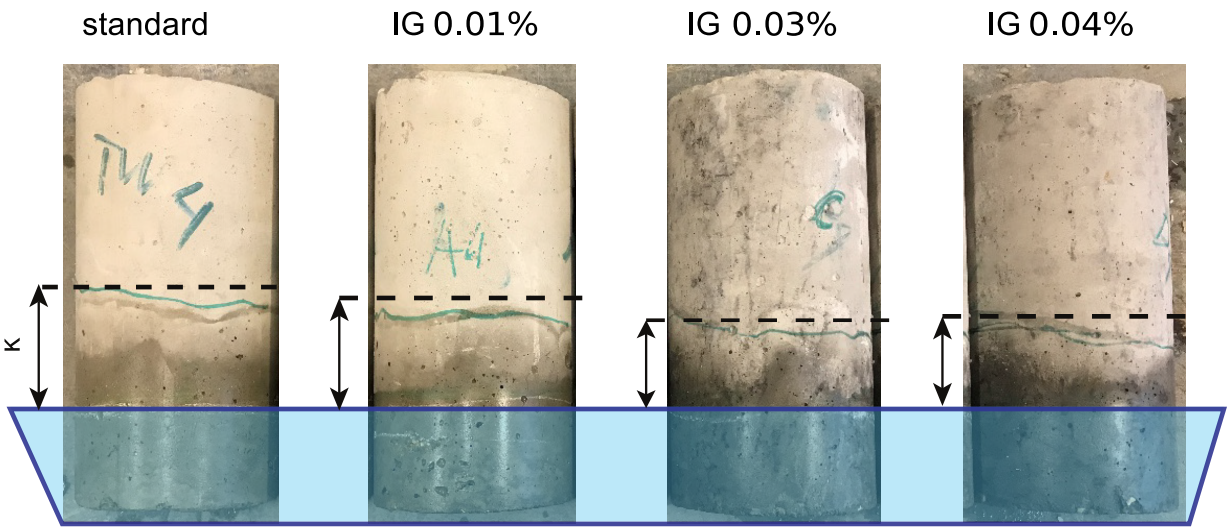

Figure 7.1: Photographs of the outer side of concrete cylinders used for water penetration tests. The blue schematic indicates initial water level and black arrows show the depth of moisture. From left to right – standard concrete and 3 samples reinforced with different graphene concentrations.

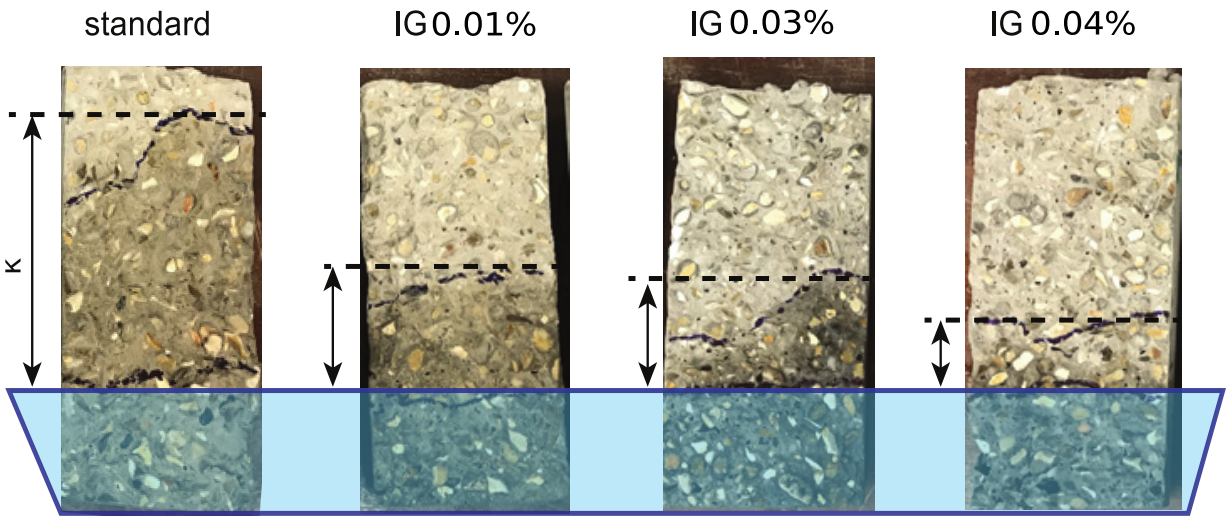

Figure 7.2: Photographs of the inner side of the same concrete cylinders from Fig.7.1.

The black lines in Fig.7.2 show the level to which the water has infiltrated through the concrete

structure after 7 days of immersion in water. It is evident that water penetrates to a lower level in the concrete reinforced with graphene than in standard concrete. Furthermore the length over which water infiltrates decreases with increasing the concentration of graphene, as apparent in Fig.7.2. This effect is also visible in Fig.7.3 which plots the maximum distance (κ) between the initial water level and the infiltration level as a function of graphene concentration. Thus concrete reinforced with graphene acts as a barrier against water infiltration.

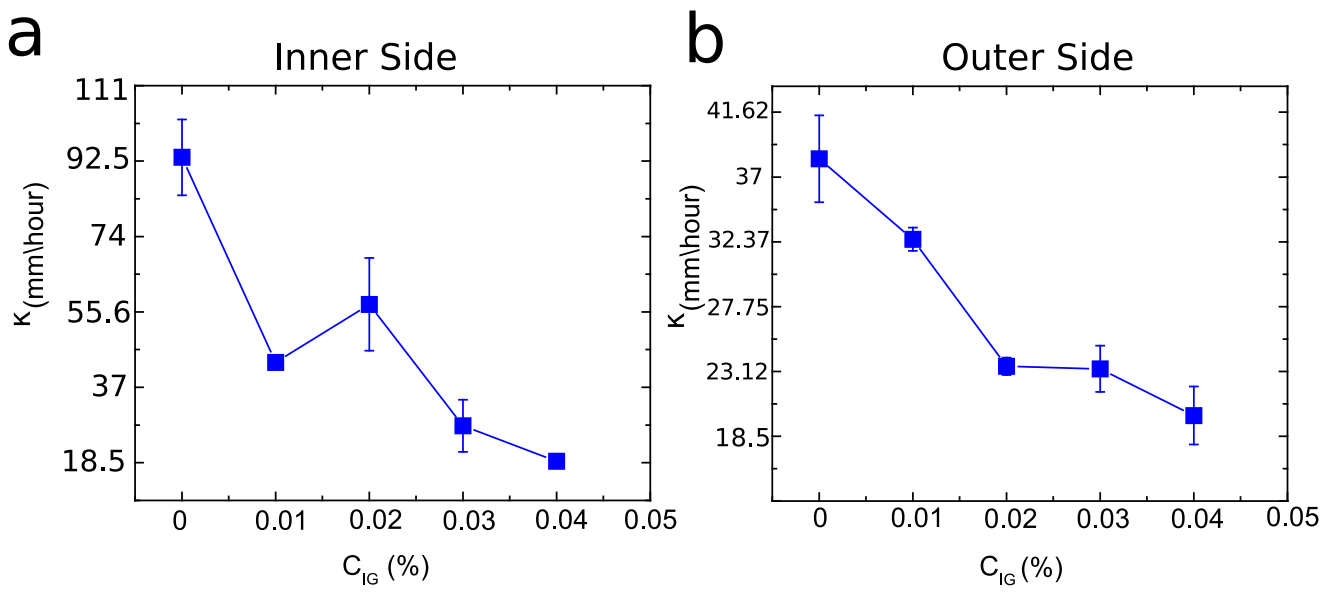

Figure 7.3: Plots showing the relationship between level of water penetration (κ), measured in ($mm/hour$) and increasing graphene concentration (C_{IG}), measured as a fraction volume of cement, used in concrete reinforcement for (**a.**) the inner side of the samples and (**b.**) outer side.

The denser and enhanced matrix of cement crystals, in combination with graphene's large surface area, reduce the microcapillary pores in size and gross volume (%) which blocks the water. In particular, a concentration of 0.04% of graphene per cement weight, decreases water permeability of concrete four times.

These findings suggest that the enhanced formation of nucleation sites for the C-S-H hydration crystals and the high surface of graphene form a denser network of interlocked cement crystals which not only increases the mechanical properties of concrete but also acts as a water infiltration barrier and drastically decrease the amount of water that can penetrate the concrete matrix through capillary pores or crack voids.

This property is extremely important for the long durability of concrete and in particular for the prevention of alkali-silica reaction (ASR), a swelling reaction that occurs in the presence of moisture between the highly alkaline cement paste and the reactive amorphous silica, resulting in serious cracking and critical structural problems. Indeed ASR can be prevented by a watertight graphene reinforced concrete barrier which could stop the evolution of the reaction[43].

ELECTRICAL AND THERMAL CONDUCTIVITY OF GRAPHENE-CEMENT COMPOSITES

The decreased water permeability of concrete reinforced with graphene could have profound consequences on its electric properties. Indeed, resistivity measurement is a common test for identifying damp in concrete structures, which typically show enhanced electrical conductivity in the presence of moisture infiltration. To quantify the effects of the addition of graphene to the cement and concrete on their electric properties, we have measured the resistivity and the temperature profile of several cement mixtures, with IG concentrations ranging from 0 (as reference) to 8 g/L, upon application of electric bias. The cement was moulded into a $4{\times}4{\times}15$ cm bar mould and the concrete into a $10{\times}10{\times}10cm$ cube moulds. For the four probes measurements, the samples are biased using the outer electrodes with a source-measurement unit that also measures the current (the schematic details are presented in Chapter 3). The inter-electrode distance (l_{2p}) is $12cm$ and $7cm$ for the cement bars and concrete cubes, respectively. While biasing the sample, the potential difference between the two inner electrodes (V_{4p}) is measured using a voltmeter. Using

the known inter-electrode distance for the inner electrodes (l_{4p}), the sample's resistivity (ρ) is given by $\rho = (A \cdot V_{4p}) / (I \cdot l_{4p})$, where I is the measured current. The total sample resistance (R) can then be calculated from $R = \rho \cdot l_{2p}/A$, whereas the contact resistance (R_c) can be estimated from $R_c = (V_A/I - R)/2$, where V_A is the applied bias. The results of the I-V sweeps, shown in Fig.7.4a, give the first indication of an increased resistivity with increased concentration of IG.

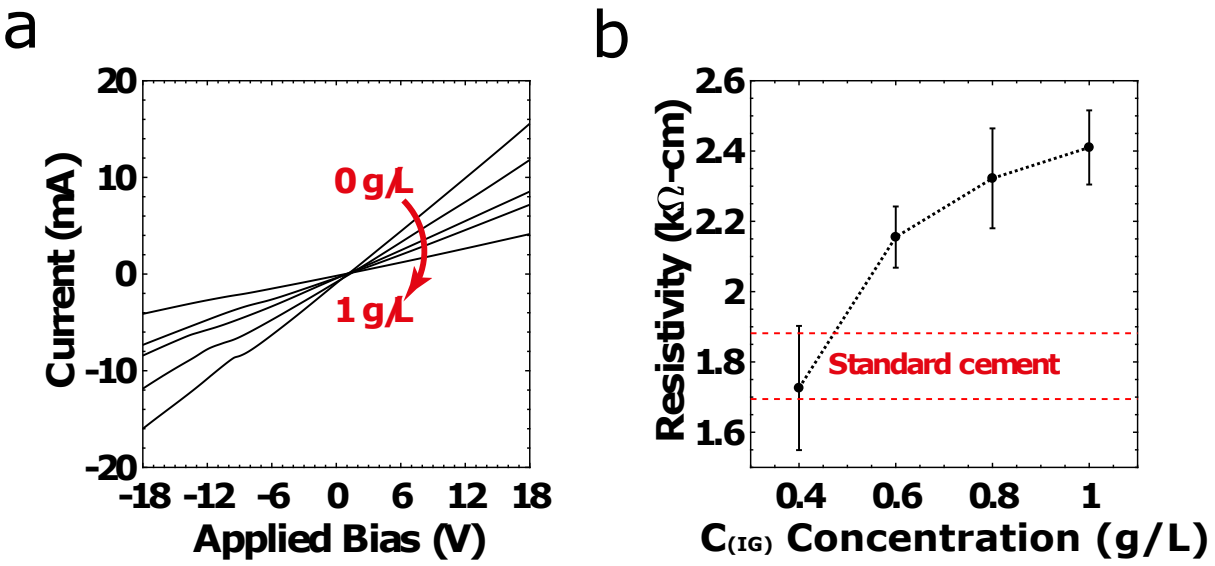

Figure 7.4: (**a.**) Current-Voltage (I-V) curves measured on cement bars with various concentration of IG ranging from 0 to 1 g/L. The arrow shows the direction of increasing IG concentration. (**b.**) Equilibrium resistivity measured on cement bars with IG concentration ranging from 0.4 to 1 g/L. The red dashes show the resistivity obtained in standard cement.

The curves are plotted for concentrations of 0 to 1 g/L IG, with increasing concentration marked by the direction of the arrow, and show a steadily decreasing slope which suggests that the overall resistance in the circuit ($R_t = 2R_c + R$) is monotonously rising with the IG concentration. However, due to the nature of the conduction mechanism in concrete, which is predominantly governed by ionic drift, the slope of the I-V curve as well as the hysteresis around 0 V are

dependent on the sweep rate. To exclude the time-dependent contribution, we have measured the steady-state resistivity by allowing the system to reach a constant current over a period of 10 minutes. The measured currents and potential drops over the last 60 seconds were then averaged and used to determine the samples' resistivity, which is shown in Fig.7.4b. In contrast to the I-V sweeps, the steady-state resistivity shows an increase in resistivity that saturates under 3 kΩ-cm. It is important to note, however, that the estimated contact resistance remains relatively constant for the different concentrations and ranges between 10 and 50 Ω for the different samples, without showing a clear trend.

The relatively low resistivity of the graphene-reinforced concrete suggests that it can be readily utilised as a resistive heater for various applications. It is well known that resistive (Joule) heating occurs when a current is passed through a resistor and that the output heat (W) is given by $W = IV = V^2/R$, where V is the applied bias, I is the induced current and R is the resistance. However, since the difference in resistance between standard concrete and graphene reinforced concrete is relatively small, as suggested by the I-V sweeps in Fig.7.5c, it is expected that the power output of a standard cube will be relatively similar to that of a reinforced one.

To maximise the power output, the cubes were biased using the inner electrodes, resulting in a lower resistance, for long periods of time, while the temperature was monitored continuously using an embedded thermocouple positioned half way between the inner electrodes. The surface temperature of the cubes was monitored periodically using a thermal camera. Fig. 7.5d shows a graphene reinforced cube with an IG concentration of 8 g/L after it has been biased for 3 hours at 50 V on the left, and a reference unbiased cube at room temperature on the right.

The striking difference in the thermal properties of the different concrete cubes is revealed when examining the heating (Fig. 7.6a and cooling (Fig.7.6b) rates of the cubes. The measurements show that both cubes follow a Newtonian cooling cycle: $dT/dt = k(T - T_0)$ where T is the instantaneous temperature, T_0 is the final (room) temperature, t is the time and k is a constant

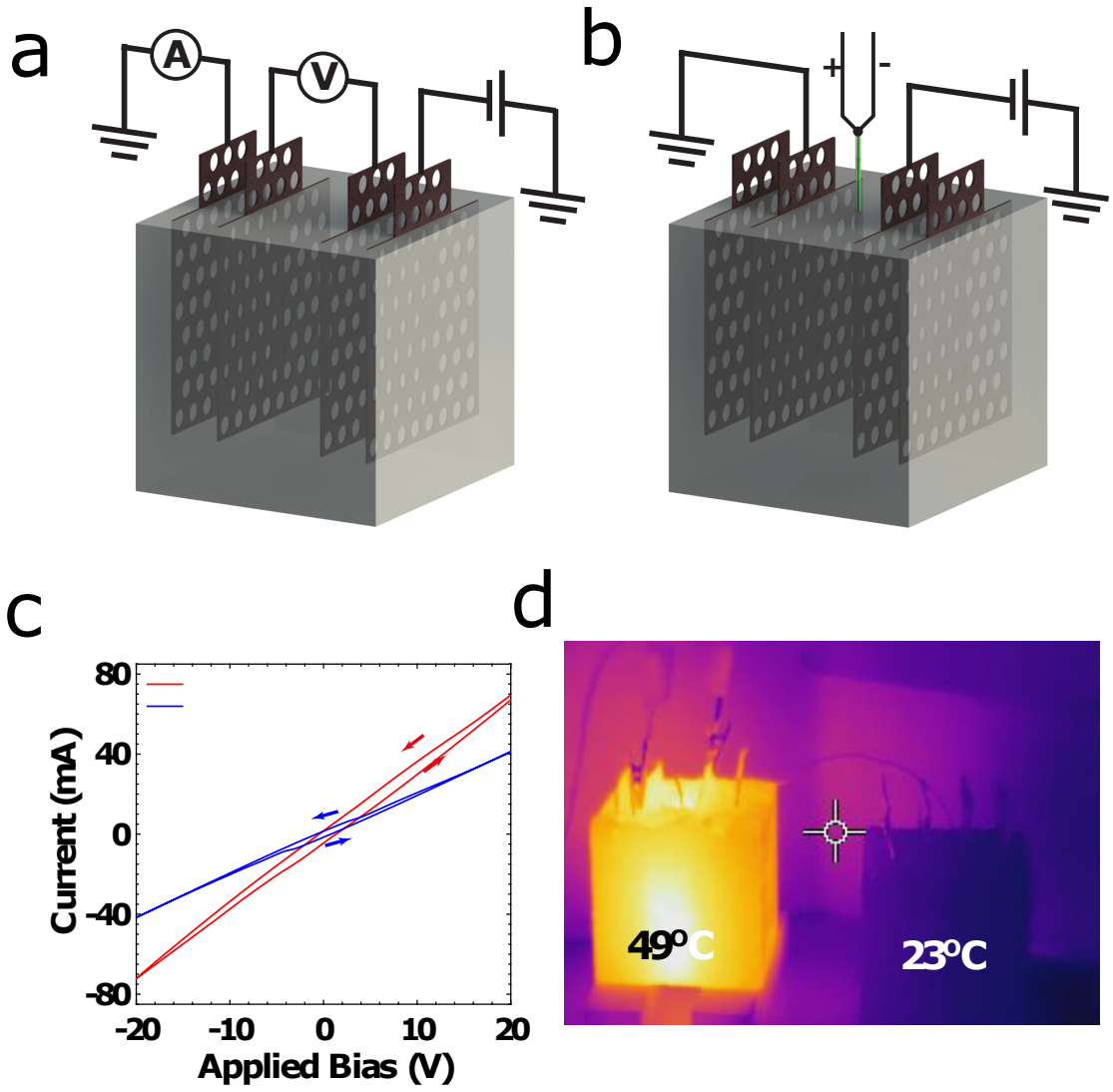

Figure 7.5: (**a.**) Schematic illustration of a concrete cube showing the embedded electrodes (not to scale) and the electric 4-probe configuration used to measure the resistivity. (**b.**) The electric configuration used to heat up the cubes and measure the developing temperature profile. (**c.**) I-V sweeps of standard concrete (red) and graphene reinforced concrete (blue) using 8 g/L IG concentration. (**d.**) Thermal image of graphene reinforced concrete cube biased with 50 V over three hours (left), and a reference unbiased cube (right).

that depends on the thermal conductivity and heat capacity of the sample, as well as on the sample geometry. The Newtonian cooling cycle indicates that the emission of heat from the sample is dominated by conduction to the surrounding environment (as opposed to convection) which is the same mechanism by which the samples heat up. While the samples reach the same steady-state temperature over long periods of time, it is clear that the heating and cooling rate of the graphene reinforced cube is substantially lower than that of standard concrete. As discussed before, the lower temperature change rate can be a consequence of lower thermal conductivity, higher heat capacity, or a combination of both. However, the thermal imaging reveals that the spatial heat profile that develops across the surface of the two cubes is qualitatively similar, suggesting that the addition of graphene contributes to the concrete's thermal stability mainly through the increase in heat capacity.

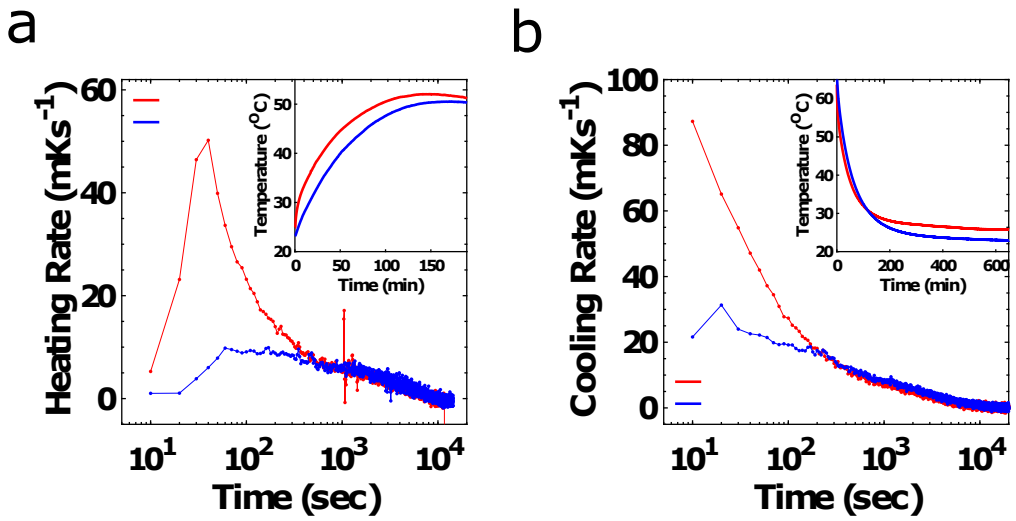

Figure 7.6: (**a.**) Heating rate of standard (red) and graphene reinforced (blue) concrete cubes shown on a semi-logarithmic scale for clarity. The inset shows the heating curves for both samples.(**b.**) Cooling rate of standard and graphene reinforced concrete cubes, shown on a semi-logarithmic scale using the same colour convention from (G). The inset shows the cooling curves obtained for both samples.

The observed resistivity of graphene reinforced concrete is also crucial for preventing corrosion when steel rebars are used as conventional reinforcement. This potential corrosion of steel, which is an electrochemical process forming corrosion cells, causes deterioration of steel reinforced concrete beams or columns through expansion, cracking, and eventual spalling of the steel rebars' cover[57]. This decreases the bond strength between steel and concrete, thus leading to severe damage to the overall structure. This incidence of damage is especially large in the structures exposed to deicing chemicals[57]. However, due to its resistive heater behaviour graphene reinforced concrete can exclude the addition of such chemicals and yet keep the corrosion formation to minimum in cases when steel embedding is required.

8

X-RAY DIFFRACTION OF GRAPHENE-CEMENT COMPOSITES

INTRODUCTION

As it was demonstrated in chapter 5, incorporation of graphene in concrete leads to increase in fundamental mechanical properties. To investigate the mechanisms behind various reinforcement, presented in earlier chapters 5 and 6 it is important to perform different type of studies to better understand the microscopic mechanisms of graphene-cement bonds.

Cement, and its hydration products, are multiphase systems which experience physical transformation upon reacting with water. The full hydration of these crystals can take enormous amount of time but the most rapid transformations happen within the first days and weeks. Phase quantifications are needed for characterising and identifying the various cement crystals, as outlined by Richardson[67;68]. Quantitative phase analysis is much needed for this work in order to identify the changes that graphene introduces to the nucleation of cement crystals, followed by their rapid growth and mechanical interlocking. The accurate knowledge about phase composition of a hydrating cementitious system given at early ages can be sufficient argument to support

the hypothesis outlined in previous chapters regarding the increased mechanical performance of concrete.

The rate of development of compressive strength of concrete made from Ordinary Portland Cement (OPC) is principally determined by the rate of hydration of its four major constituents, alite, belite, aluminate and ferrite[83]. Typical proportions for these major constituents are in the range alite (45-60%) belite (12.5-25%), aluminate (7-12.%) and ferrite (6.0-10.0%).

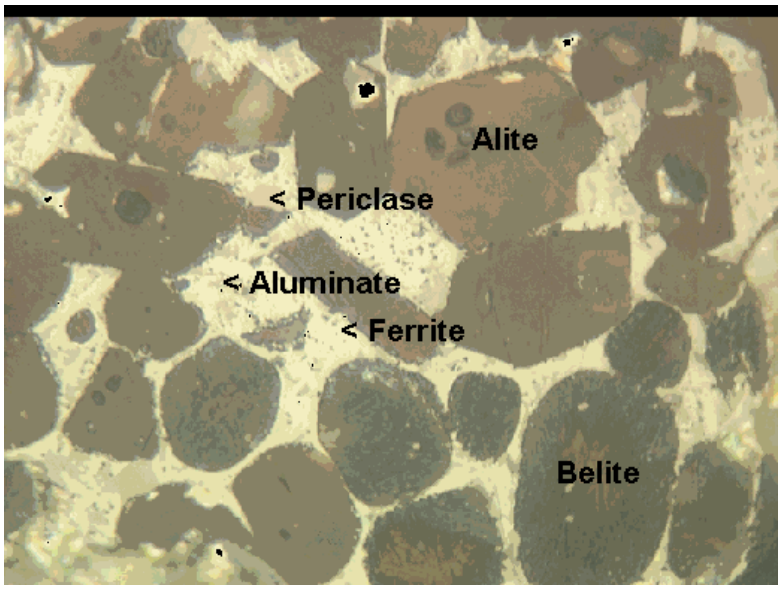

Figure 8.1: Photograph of hydrated cement groups, including Alite, Belite, Aluminate and Ferrite - which comprise more than 80% of the overall cement composition, adopted from[5]

The aluminate and ferrite which constitute the minor phases, consequently make only a minor contribution to strength development relative to the two silicate phases, especially alite[83].

Several authors have introduced the X-Ray Diffraction system (XRD) as a powerful and versatile tool for studying cementitious hydration crystals[38;15;56;64]. Measurement conditions are key factor for successful analysis and interpretation of data. For this experiment, Standard Cement (SC) , FG and IG reinforcement cement were compared after 24h of hydration. The samples were dried at air temperature and ball-milled back into fine powder prior to scanning. Cement-

to-water ratio (0.5) and amount of cement used were strictly kept the same for all experimental groups. The mechanical performance of FG and IG reinforced concrete was shown in previous chapters and now the focus is shifted towards their phase compositions and time-dependent phase transformations.

RESULTS

A number of works have investigated hydration of the individual cement compounds in OPC. Work by Copeland et al[19] suggests that hydration of the pure cement compounds is slower than that of the same compounds in cement paste. Also water/cement ratio (w/c) influences the rate of hydration, the tendency being that the greater the w/c ratio, the greater the hydration rate. Alite and belite hydrate at very different rates, belite being much slower to hydrate than alite[19;9] Although differences in the cements in relation to factors such as specific surface, impurities and differences in curing conditions produce a wide variation in hydration rates, it is undoubtedly the case that in OPC a very substantial proportion of alite has hydrated within the first few days, and by 28 days[19], hydration is near to completion, whilst belite takes slightly more time to achieve the same degree of hydration. Therefore, the major contribution to strength development of concrete within the first few days of curing is derived from alite hydration, with small contributions from belite hydration and hydration of the aluminate and ferrite phases. As curing progresses, belite hydration makes an increasing contribution to the strength development, and beyond 28 days, it is the principal contributor to strength gain, that from alite hydration becoming negligible[19].

The results in this section aim to explore the phase differences and degree of crystallinity in SC, FG and IG cement samples. The family of cement hydration crystals is huge[67] and therefore only 5 main groups have been identified and different crystals have been allocated accordingly. The work by presents a detailed breakdown of crystals' names and corresponding diffraction angle

(2θ):

1. Tricalcium Silicates, alite [C_3S]

2. Dicalclum Silicates, belite [C_2S]

3. Calcium Aluminates [$CaAl_4$]

4. Calcium Aluminoferrites [$Ca(AlFe)_2O_5$]

5. Calcium Carbonate [$Ca(OH)_2$]

Fig.8.2 shows a comparison between the three experimental groups. It plots the intensity (a.u. units) of various crystal peaks against their relative location (degrees).

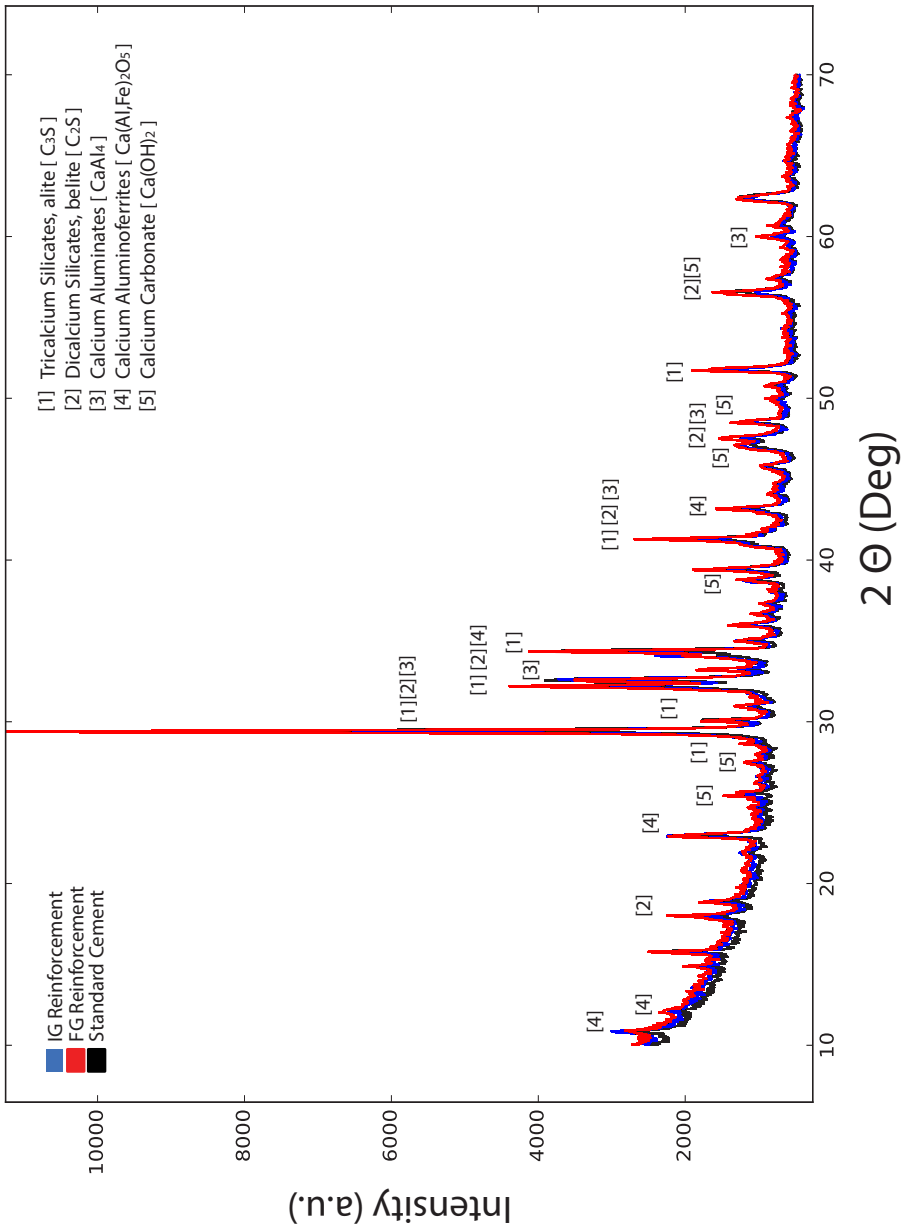

Figure 8.2: Full X-Ray Spectra of representative cement hydrated samples, ranging from 10° to 70°.

601626 This chapter examines different regions in the whole range (between 5° and 70°) of the typical 2θ spectrum of cement phases. Fig.8.3 shows the peak around 23°. It can be seen that both FG and IG graphene dispersions react with the calcium aluminoferrites and the high intensity or sharp peak is an indication of more order, crystallization and arrangement, but it can also be due to strain. The increased intensity suggests enhanced microstructure of either Alumina or Ferrite composites. Looking at the range between 25° and 26° there are two new graphene peaks present in FG and IG[88].

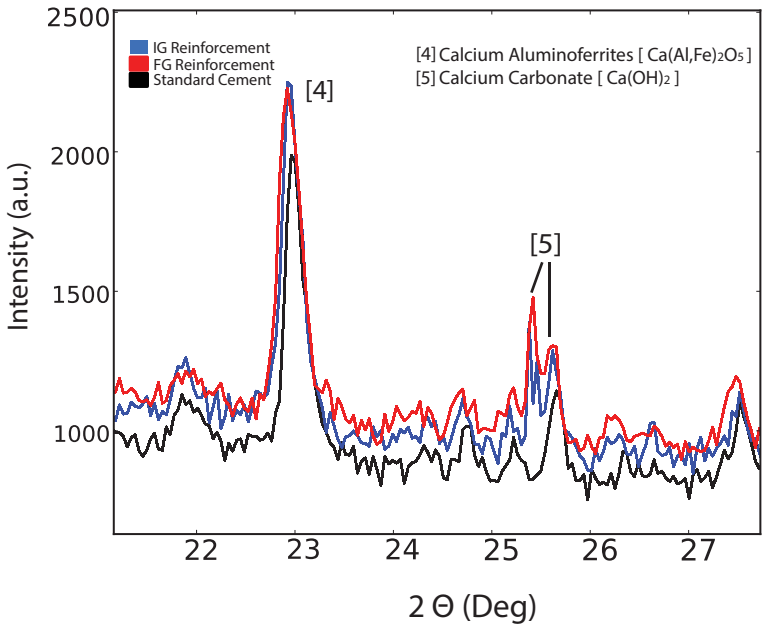

Figure 8.3: Zoom in into the X-Ray spectra, between 22° and 28° with a focus on the graphene-calcium carbonate bond at 25.5°.

Since the calcium silicate groups of the C-S-H gel are mainly responsible for the mechanical strength of the cement paste[67], and there is consistent increase in strength due to graphene enhancement, it can be concluded that the graphene flakes interact not only with the Calcium Carbonates but with the silicates as well. Next, Fig.8.4 focuses on the peak at 29.5° where another

set of $Ca(OH)_2$ crystals are located. It is evident that both FG and IG have impact on the calcium groups, however, FG increases the peak intensity by more than 30%[88].

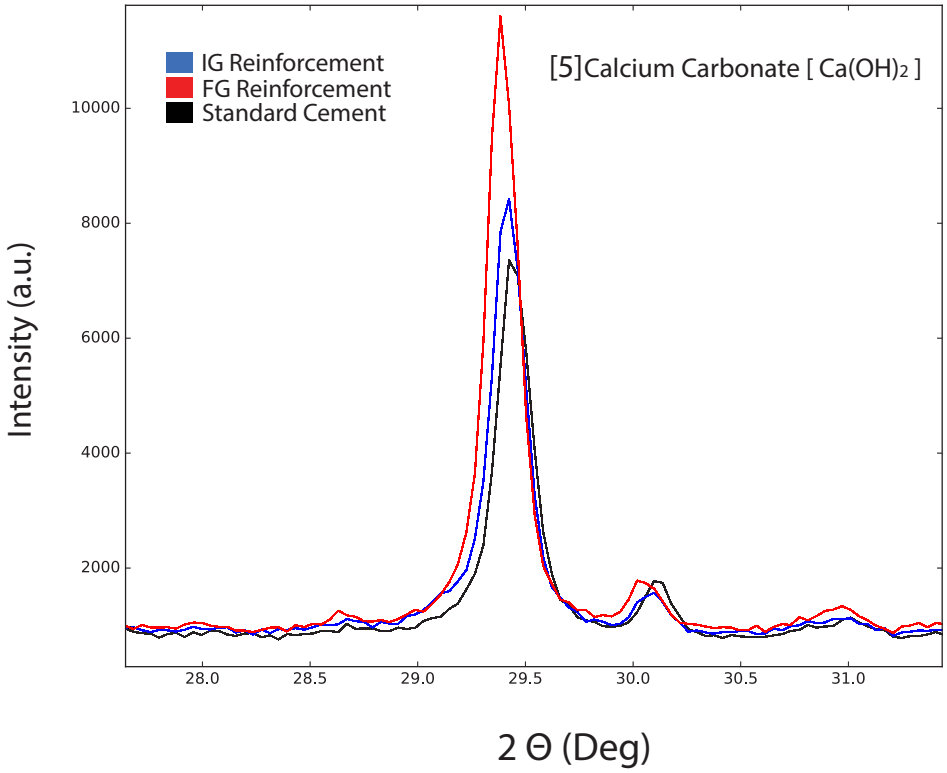

Figure 8.4: Zoom in into the X-Ray spectra between 28° and 31.5°. The Calcium Carbonate peak reacts with the FG dispersions to form a bigger crystal.

This suggests that the smaller the lateral size, and fewer number of layers per flake, have better impact on the carbonation of cement. Fig.8.5 and the next region on the XRD spectrum, it can be noted that the addition of graphene has an effect on multiple crystals. First, looking at the Tricalcium and Dicalcium silicates at 32° , 32.8° and 33°, the small lateral dimension of FG dispersion has better effect than the IG. Alite (C_3S) and Belite (C_2S) are both responsible for

concrete strength, as described earlier, and the results indicate that FG improves the degree of crystallinity of

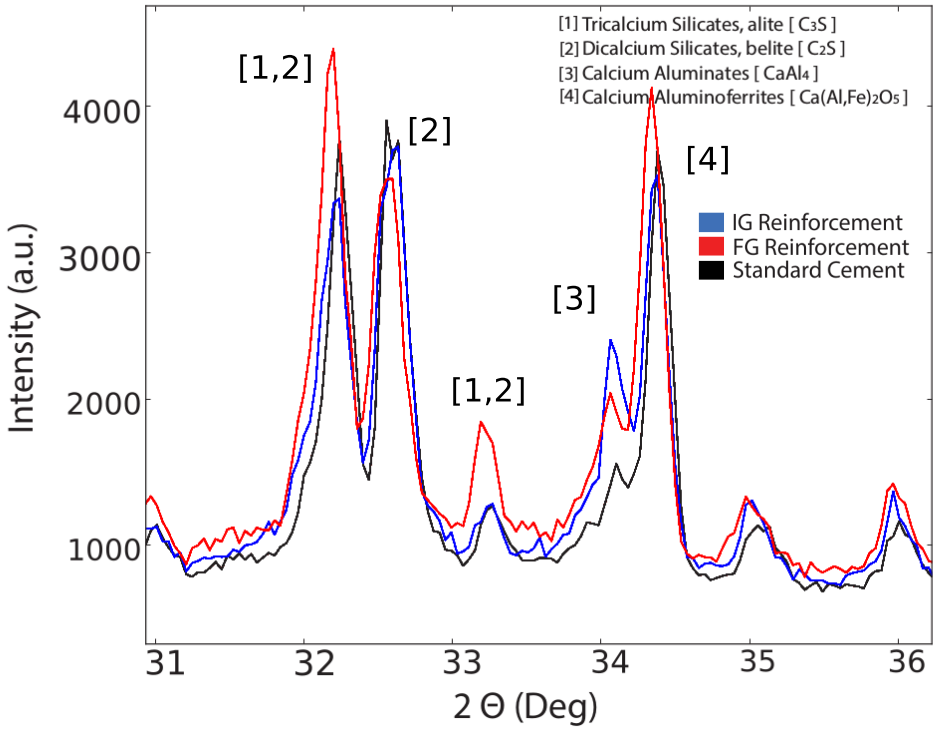

Figure 8.5: Focus on the region between 31° and 36.5° of the X-Ray spectra. Graphene peak present at 33°.

both crystals at early age strength. The small shoulder peak at 34° shows that both FG and IG graphene have direct impact on the aluminates. Upon reacting with water the nature of the hydrates formed is dependent on the temperature of hydration. At lower temperatures CAH_{10} is the first hydrate formed, at intermediate temperatures C_2AH_8 and AH_3, and at higher temperatures C_3AH_6 and AH_3[71] . The stable phases are C_3AH_6 and AH_3, and the other phases will inevitably convert to these at a rate dependent on temperature and moisture. C_3AH_6 has the highest density of the calcium aluminate hydrates, resulting in a higher porosity at a given

degree of hydration[71]. However, the conversion reaction also leads to the release of water, which is available for further reaction of remaining anhydrous material. For this reason the aluminates, controlled by the initial w/c ratio, play a very important role in the early stage strengthening of cement, and consequently of concrete.

The bond between graphene and alumina has been reported previously[16;47]. Broniszewski et al introduced graphene oxide (GO) into ceramic matrix and their work focused on investigating influence of GO on mechanical properties of alumina matrix ceramic composites such as hardness, fracture toughness and Young's modulus[16]. Another work which confirms the interaction between the two materials is by Liu et al[47]. Their work on alumina (Al_2O_3) ceramic composites reinforced with graphene platelets (GPLs), shows that GPLs are well dispersed in the ceramic matrix. The flexural strength and fracture toughness of the GPL-reinforced Al_2O_3 ceramic composites are significantly higher than that of monolithic Al_2O_3 samples[47]. A 30.75% increase in flexural strength and a 27.20% increase in fracture toughness for the $Al2O_3$ ceramic composites have been achieved by adding GPLs[47]. The reported results indicate that FG and IG in this work have truly changed the morphology of alumina crystals in the cement which resulted in overall increase in mechanical strength of concrete.

Fig.8.6 focuses on another region, which shows further microstructural improvements of cement crystals. The shoulder peaks at 47°, as well as 47.5° show significant increase in crystal size and structure, due to the addition of both FG and IG. There is a new small peak present at 47.2° with IG, which suggests for morphological alterations due to graphene reinforcement. Both belite (C_2S) and aluminates ($CaAl_4$) increased durability and mechanical interlocking, as confirmed with the

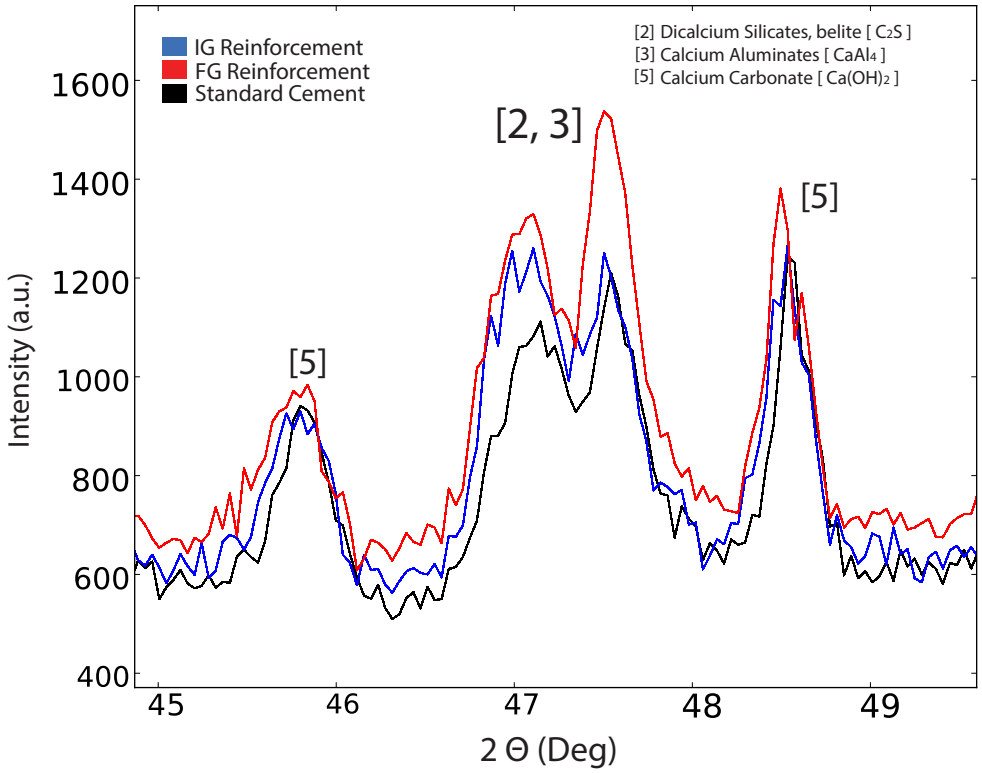

Figure 8.6: Focus on the region between 45° and 50°.

non-linear fracture studies in Chapter 7. The delayed formation and propagation of cracks under flexural loading could be as a result of the increased crystal size of both C_2S and $CaAl_4$. The calcium carbonate chemical bond with graphene is also confirmed in other literature. For example, Wang et al[82] demonstrated that the composite crystals of calcium carbonate ($CaCO_3$) and graphene with hexagonal plate or ring, dendritic and rhombohedral shapes were synthesized by the hydrothermal reaction of calcium acetate and urea in the presence of graphene oxide (GO) sheets. Their crystal structures were characterized to be vaterite, aragonite and calcite, respectively. In this case, the hydrothermally reduced graphene oxide (rGO) acted as an atom-thick, two-dimensional template for controlling the nucleation and growth of the $CaCO_3$ crystals[82].

The group showed that their samples (PVA, VCC) exhibit increased Young's modulus and tensile strength of PVA/45 wt% VCC were tested to be 34.1 ± 2.5 GPa and 165 ± 6 MPa, respectively. Another work by Zhao et al[91] demonstrates graphene synthesis from caclium carbonate, which further confirms the molecular interaction between the two materials.

CONCLUSIONS

In conclusion, this Chapter investigated the microstructural changes and degree of crystallinity of three different cement pastes - the control group mixed with Tap Water, and two with graphene dispersions (FG and IG). The same concentrations of FG and IG were used as in previous chapters, to observe and study the degree of impact that graphene has on hydration crystals of cement. XRD diffractometer was used in this experiment to quantify the results and present a spectrum of peaks, comparing the three experimental groups. All samples were left to hydrate and dry $24h$ prior to measurements.

Various regions of the XRD spectra were studied, investigating the 5 main groups of cement hydration crystals - C_3S, C_2S, $CaAl_4$, $Ca(AlFe)_2O_5$ and $Ca(OH)_2$. The results show that both FG and IG have huge impact on all 5 groups, creating new crystal or enhancing the structure and durability of existing ones. These conclusions confirm and solidify the results from previous chapters and are in agreement with various other studies on the bond between graphene and the aforementioned crystals.

Part IV

Conclusions

9

DISCUSSION AND CONCLUSIONS

Chapter 9 aims to summarise all results, conclusions, hypothesis and discuss a few important topics which arise as a follow up to my thesis.

This research work demonstrated a novel method for reinforcing traditional construction material concrete using the nanomaterial graphene, two dimensional allotrope of carbon with exceptional mechanical and electrical conductivity properties. The addition of graphene – and in particular its large surface area and ability to retain initial size after strain, promotes changes in the main chemical reaction behind concrete strengthening. One of its main constituents – cement, undergoes physical transformation upon reaction with water and graphene enhances the evolution and growth of cement crystals during their hydration period. This leads to a denser matrix of fibrous calcium silicate crystals which not only make the composite material stronger, but also decrease its water permeability and increase the heat resistivity[73].

Firstly, an optimised method for producing large quantities of defect-free graphene flakes, dispersed in water was demonstrated. There were two types of graphene investigated and both showed long-term stability and avoided agglomeration, despite their hydrophobic nature. This was achieved by introducing the surfactant sodium cholate which bridged the carbon atoms with

water molecules. Raman Spectroscopy was used to quantify the number of graphene layers – the majority being between 6-8 layers per flake. This calculation was then supported with statistical study of over 400 individual Raman spectras, for each graphene type, plotted as $20\times20\mu$m maps to show the uniformity and continuity of liquid-exfoliated suspensions. An industrial grade 3 graphene nanoplatelets were also exfoliated in the very same method of high-shear blending and they demonstrated similar uniform distribution, with predominantly 10 layers per flake. Following this study, I examined the nature of defects in both types of graphene, showing that for all concentrations there are no basal-plane defect introduced via the high-shear blending exfoliation. This conclusions was supported by both plotting the individual I_D/I_G ratios as a Raman map and by relating the intensities of D and D$\prime$ peaks for all graphene types. Finally, it was showed that this method is scalable for production rates exceeding $100L/h$.

After this in-depth systematic study of the nature of liquid-exfoliated graphene suspensions, I focused on exploring the fundamental properties of concrete. For all experiments with concrete, there were two experimental groups for comparison – one mixed with tap water, which served as a reference and multiple others containing various graphene concentrations. The sample preparation and testing conditions were always kept strictly the same in order to minimise the source of error and derive conclusions based purely on chemical alterations. I studied the evolution of concrete's compressive strength as a function of time and as a function of increasing graphene concentration, showing a linear increase in both cases with maximum improvement by 146%. The results were further supported by a statistical study, comprising more than 200 concrete cubes, which showed that the increased strength is not due to a technical error but rather due to the reinforcement indeed. The flexural strength of concrete was also improved by 79% after 28 days of curing and also increased linearly as more graphene was added. However, there is a threshold of the graphene concentration (g/L). It is valid to say, for both mechanical properties, that adding too much initial graphene powder to the solution can result in left-over sediment and this hampers the hydration

of cement.

Chapter 6 presented a very different approach in studying the mechanical behaviour of graphene reinforced concrete. I investigated the nonlinear fracture mechanics (NFM) of concrete beams during constant loading and the consequential evolution and propagation of cracks within the internal cement-graphene matrix. Two NFM approached were selected among literature and implemented in specifically designed computer algorithm, which upon inputting raw data from experiments, calculated various parameters such as total fracture energy accumulated during flexural loading (showing 134% increase with reinforcement), stress intensity factor for in-plane separation (increased by 78.7%), improved ductility by 79%, double-G fracture parameters etc. Standard concrete samples were compared to graphene reinforced ones with various concentrations. All of the fracture parameters showed linearly increasing relationship with graphene concentration.

To gain further understanding of the graphene reinforcement and complete the full gamma of concrete properties, I explored various multifunctionalities of cement-based composites in Chapter 7. Firstly, water impermeability of reinforced concrete was studied by immersing it in water tank for 7 days and observing the resultant water penetration. The large surface area of graphene flakes not only improves the mechanical performance of concrete, but solidifies the cement matrix and acts as a barrier for H_2O molecules, showing four times total decrease of of water permeability. Furthermore, cement prisms with 4 electrodes were prepared to measure and compare the resistivity of cement upon adding various graphene concentrations. After showing a consistent trend, I decided to explore the heat transfer capacity, by measuring the potential difference between the two inner electrodes of a 4-probe cube sample. The temperature was monitored continuously using an embedded thermocouple and the surface temperature was observed using a thermal camera. Combining both time-dependent data and thermal observations it was shown that there is a huge difference in heating and cooling rates of standard and reinforced concrete samples. The observed resistivity of graphene reinforced concrete is also crucial for preventing corrosion when

steel rebars are used as conventional reinforcement. This potential corrosion of steel, which is an electrochemical process forming corrosion cells, causes deterioration of steel reinforced concrete beams or columns through expansion or cracking. This decreases the bond strength between steel and concrete, thus leading to severe damage to the overall structure.

To continue the discussion, attention has to be focused on two inevitably arising questions, following the analysis and results presented above. Firstly – where does the graphene bond, i.e. how does it change the cementitious crystals? Since there are more than 60 different types of cement crystals which comprise the C-S-H gel, as discussed in Chapter 2, it will be very difficult to provide scientifically valid answer. Other researchers have tried to identify and localise carbon nanotubes with SEM within a hardened cement matrix, claiming their micrographs as evidence for the nanomaterial's bond, however, this result is not entirely correct simple due the fact that there is no data analysis supporting the elements shown on the image. The second approach in trying to answer this question would be using XRD spectroscopy to potentially identify and quantify the type of crystals from the cement spectra. This can be helpful for one to derive conclusions based on crystals' size and shape – it can be assumed that the graphene promotes crystal growth indeed, but yet again it does not give a precise answer to the question where exactly does it bond to. Only through a statistical study conclusions can be derived for the composites' mechanical performance.

The second big question that follows up this research work lies in the economical and cost analysis – how much more expensive is this novel reinforcement, when compared to normal concrete? Since the samples prepared are according to British and European standards for construction, it is important to look into the cost of $1m^3$ of normal concrete and analyse the increased price due to the addition of graphene. Synthesised economic research was conducted to compare and evaluate the cost-effectiveness of our nanoengineered concrete. I had to take into account multiple factors like materials' costs, raw graphene powder, reduction of carbon emissions and extra production

costs for graphene exfoliation. Preliminary calculations for 1 m^3 of concrete are presented in Table9.1:

Table 9.1: Price comparison of standard and graphene reinforced concrete

		Normal Concrete	Reinforced Concrete
Compound	Volume (kg)	Price (£)	Price (£)
water	200L	0	£547
cement	400	£87	£87
sand	800	£102	£102
aggregate	1200	£68	£68
Total price:		**£257**	**£804**

At first look the costly graphene solution nearly triples the total price of concrete, however if the improvement in mechanical performance is taken into account, then the total volume of materials can be reduced by half. This leads to a final 56% increase in total cost per m^3. There is no doubt that this % is quite high and it will take time before graphene prices drop, due to increased manufacturing.

Undoubtedly the single most important benefit of this nanoengineered concrete is the reduction of cement usage. Reports on global greenhouse gas emissions, from various sources, summarised in a study[2] show that the largest proportion of emissions (65%) comes from Carbon Dioxide, as shown at Fig.9.1a.

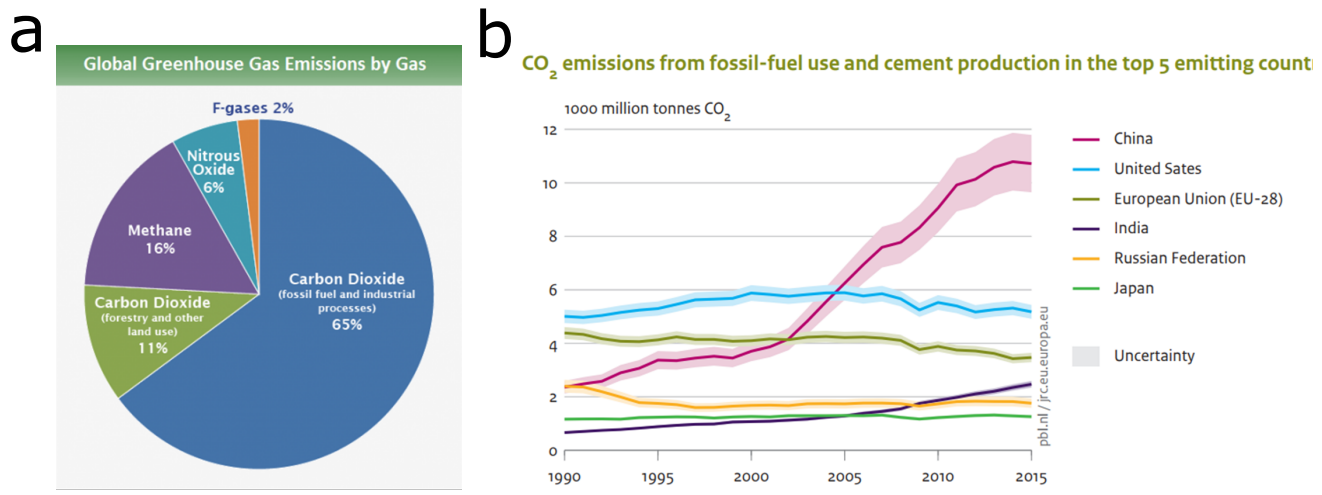

Figure 9.1: (**a**) Pie chart showing the % distribution of total global greenhouse gas emissions. (**b**) Plot showing the CO_2 emissions from fossil fuel use and cement production as function of time in billions tonnes for the top 5 emitting countries, adopted from[2].

The primary source of CO_2 are industrial processes, including cement manufacturing. Fig.9.1b indicates the uprising trend in CO_2 emissions in billions of tonnes in the top 5 emitting countries[55].

PUBLICATIONS

The ideas and data presented in this thesis are subject of the following publications. At the time of writing (and submission), the first paper on the list has been published, the second has been accepted and is due to be published, and the third has been submitted to a journal.

- Dimov, D., Amit, I., Gorrie, O., Barnes, MD., Townsend, NJ., Neves, A.I.S., Whiters, F., Russo, S., and Craciun, MF. Ultrahigh Performance Nanoengineered Graphene–Concrete Composites for Multifunctional Applications. *Advanced Functional Materials 28*, 23 (2018), 1705183.

- D.W. Shin, M. D. Barnes, K. Walsh, D. Dimov, P. Tian, A. I. S. Neves, C. D. Wright, S. M. Yu, J.B. Yoo, S. Russo, M. F. Craciun, *Advanced Materials*. 2018, 30, 1802953.

- Dimov, D., Craciun, MF., Non-Linear Fracture Mechanics of Graphene Enhanced Concrete. *Submitted* (2018)

ACKNOWLEDGEMENTS

This section of my thesis remains private to the reader and the only part where I can share some personal thoughts, aside from technical analysis. I would like first and foremost to thank my parents, Rossi and Miro, for their continuous push and support since I was about 12 years old. If it wasn't for their efforts, care, persistence, attention, and financial support, I would not have had the opportunity to attend the best private high school in Bulgaria - the American College of Sofia, which was the stepping stone for my entire path up to the submission of this work. Back then I could have never realised the true potential of attending this institution, but now, 12 years later it all makes sense. Of course, their warm support, unconditional love, smiles and appreciation have extended to this day August 2018 and I'm sure that it will continue. Completing my PhD without their financial support would have not been possible, for which I will be forever grateful.

Secondly, I would like to acknowledge and thank my first supervisor Prof Craciun. Back in 2014 when I had some turbulence in my private life, she was the one who decided to trust a 2^{nd} year undergraduate student, and support my idea about reinforcing concrete with graphene. Monica was the one who literally picked me up from the ashes in May 2014 and gave me opportunity to stay over the summer leading up to my 3^{rd} year and begin, what it turned out to be, a four year long journey. Her continuous support and mentoring earned me the Phillip Booth Prize in Engineering for the highest mark in the department (part of my BENG course) and she backed me

up in front of the college to be accepted for a PhD position, despite having a 2:2 overall. Needless to say, but without Monica's smile and calm supervision I would have not ended up here writing this final section of my thesis. To me, Monica, you are part of my family and friends, and forever will be, because of your enormous contribution not only to my personal growth and development, but the huge jump-start you provided to my career as well. I would like to also thank my second supervisor, Prof Saverio Russo, who taught me to always aim for the sky and never settle down with the mediocrity.

I would like to dedicate the next words to a person who came to my life very unexpectedly, on my 24^{th} birthday, and now proved to be my better half in life. Even though we knew each other since high school, I never imagined that you'd be the one whom I appreciate and love so much today. Of course, these feelings did not come for granted. You were the one who supported me mentally during this long and difficult journey as a PhD. As I've said many times before, the greatest challenge of the doctorate degree is not reading papers or doing experiments, but keeping yourself motivated for 1000 days without any immediate reward for your efforts. Well, you kept me on the right track and if it weren't for you, I could've easily dropped out at 2 different times. Your kindness, personal values, appreciation, care and strong character stood like a concrete pillar behind my back for the past 2 years and despite what the future holds for us, I'd like you to know that at this point in my life, I'd choose no one else but you, Donika.

Lastly, I would like to acknowledge and thank all of my true friends, who expressed enormous support and appreciation equally during the past years whilst I was struggling with the unknown adventures of the PhD. Thank you Viktorio, Dorotea, Joana, Lachlan, Martin, Stefan, Ivan, Lachezar, Nadya, Thomas, Shiva, Arnav, Tumnishki, Niki, Alek, Lin and Andrey.

BIBLIOGRAPHY

[1] Geopolymer research - queen's university belfast. https://blogs.qub.ac.uk/geopolymer/geopolymer-background/. Accessed: 2018-07-16.

[2] Global construction market worth 10.3d trillion in 2020. https://www.prnewswire.com/news-releases/global-construction-market-worth-103-trillion-in-2020-50-largest-most html. Accessed: 2018-02-13.

[3] Graphene applications and uses. https://www.graphenea.com/pages/graphene-properties#.W0ynJ9Izo54. Accessed: 2018-07-16.

[4] Graphite powder. http://www.sigmaaldrich.com/catalog/product/aldrich/282863?lang=enregion=GB. Accessed: 2018-02-18.

[5] Phase composition analysis of the nist reference clinkers by optical microscopy and x-ray powder diffraction = https://ciks.cbt.nist.gov/~garbocz/tn1441/node1.htm, note = Accessed: 2018-07-16,.

[6] Use and importance of plasticizers and super-plasticizers in concrete. https://www.strukts.com/2012/07/use-and-importance-of-plasticizers-and-super-plasticizers-in-concrete/. Accessed: 2018-02-13.

[7] Al-Dahawi, A., Öztürk, O., Emami, F., Yildirim, G., and Şahmaran, M. Effect of mixing methods on the electrical properties of cementitious composites incorporating different

carbon-based materials. *Construction and Building Materials 104* (2016), 160 – 168.

[8] Allen, M. J., Tung, V. C., and Kaner, R. B. Honeycomb carbon: A review of graphene. *Chemical Reviews 110*, 1 (2010), 132–145.

[9] Ash, J., Hall, M., Langford, J., and Mellas, M. Estimations of degree of hydration of portland cement pastes. *Cement and Concrete Research 23*, 2 (1993), 399 – 406.

[10] Avouris, P., and Dimitrakopoulos, C. Graphene: synthesis and applications. *Materials Today 15*, 3 (2012), 86 – 97.

[11] Barros, J. A. O., Cunha, V. M. C. F., Ribeiro, A. F., and Antunes, J. A. B. Post-cracking behaviour of steel fibre reinforced concrete. *Materials and Structures 38*, 1 (Jan 2005), 47–56.

[12] Bianco, A., Cheng, H.-M., Enoki, T., Gogotsi, Y., Hurt, R. H., Koratkar, N., Kyotani, T., Monthioux, M., Park, C. R., Tascon, J. M., and Zhang, J. All in the graphene family – a recommended nomenclature for two-dimensional carbon materials. *Carbon 65* (2013), 1 – 6.

[13] Boey, X. H. Z. Y. S. W. X. Q. Q. H. Q. Z. Q. Y. F., and Zhang, H. Graphene-based materials: Synthesis, characterization, properties, and applications. *Small 7*, 14 (June 2011), 1876–1902.

[14] Bointon, T. H., Barnes, M. D., Russo, S., and Craciun, M. F. High quality monolayer graphene synthesized by resistive heating cold wall chemical vapor deposition. *Advanced Materials 27*, 28 (2015), 4200–4206.

[15] Brindley, G. Effect of grain or particle size on x-ray reflections from mixed powders and alloys considered in relation to quantitative determination of crystalline substances by x-ray methods. 347–369.

[16] Broniszewski, K., Wozniak, J., Kostecki, M., and Olszyna, A. Properties of

alumina – graphene oxide composites. *Materials Today: Proceedings 2*, 1 (2015), 370 – 375. ANM2014: 5th International conference on Advanced Nanomaterials.

[17] Chen, T., Zeng, B., Liu, J. L., Dong, J. H., Liu, X. Q., Wu, Z., Yang, X. Z., and Li, Z. M. High throughput exfoliation of graphene oxide from expanded graphite with assistance of strong oxidant in modified hummers method. *Journal of Physics: Conference Series 188*, 1 (2009), 012051.

[18] Chuah, T. J. S., Pan, Z., Sanjayan, J. G., Wang, C. M., and Duan, W. Nano reinforced cement and concrete composites and new perspective from graphene oxide. *Construction and Building Materials 73* (2014), 113 – 124.

[19] Copeland, L., and Kantro, D. 387.

[20] D. Akinwandea C. J. Brennana J. S. Bunchb, P. Egbertsc, J. R. F. H. G. R. H. J.-S. K. T. L. Y. L. K. M. L. N. L. H. S. P. E. J. R. P. W. B. I. Y. T. Z. Y.-W. Z. Y. Z., and Zhuo, Y. A review on mechanics and mechanical properties of 2d materials—graphene and beyond. *Extreme Mechanics letters 13* (May 2017), 42–77.

[21] Eckmann, A., Felten, A., Mishchenko, A., Britnell, L., Krupke, R., Novoselov, K. S., and Casiraghi, C. Probing the nature of defects in graphene by raman spectroscopy. *Nano Letters 12*, 8 (2012), 3925–3930.

[22] Emiroglu, M., Ala Eddin Douba, R. A. T., and Kandil, U. F. New polymer concrete with superior ductility and fracture toughness using alumina nanoparticles. *Journal of Materials in Civil Engineering 29* (2017).

[23] F. Babak, H. A., and Parviz, G. Preparation and mechanical properties of graphene oxide: Cement nanocomposites. *The Scientific World Journal* (2014).

[24] Ferrari, A. C., and Basko, D. M. Raman spectroscopy as a versatile tool for studying the properties of graphene. *Nature Nanotechnology 04* (April 2013), 8–235.

[25] Feynman, R. There's plenty of room at the bottom (reprint from speech given at annual

meeting of the american physical society). *Engineering and Science* (1960), 22–36. cited By 23.

[26] Golewski, G., and Sadowski, T. The fracture toughness the kiiic of concretes with f fly ash (fa) additive. *Construction and Building Materials 143* (2017), 444 – 454.

[27] Granju, J.-L., and Balouch, S. U. Corrosion of steel fibre reinforced concrete from the cracks. *Cement and Concrete Research 35*, 3 (2005), 572 – 577.

[28] Gu, X. *Basic Properties of Concrete*. Springer Berlin Heidelberg, 2016.

[29] Hernandez, Y., V. Nicolosi, M. L., and Colemann, J. High-yield production of graphene by liquid-phase exfoliation of graphite. *Nature Nanotechnology 3* (2008), 563–568.

[30] Hongjian Du, Ser Tong Quek, S. D. P. Smart multifunctional cement mortar containing graphite nanoplatelet. *Proc.SPIE 8692* (2013), 8692 – 8692 – 10.

[31] Horszczaruk, E., Mijowska, E., Kalenczuk, R. J., Aleksandrzak, M., and Mijowska, S. Nanocomposite of cement/graphene oxide – impact on hydration kinetics and young's modulus. *Construction and Building Materials 78* (2015), 234 – 242.

[32] J. Lee, D. Y., and Cheong, H. Estimation of young's modulus of graphene by raman spectroscopy. *Nano Letters 12*, 9 (August 2012), 4444–4448.

[33] J.B. Mander, M. P., and R.Park. Theoretical stress strain model for confined concrete. *Journal of Structural Engineering 114* (1988).

[34] J.M.Tour. Top-down versus bottom-up fabrication of graphene-based electronics. *Chemical Materials 26*, 1 (August 2014), 163–171.

[35] Jumate, E., and Manea, D. L. X-ray diffraction study of hydration processes in the portland cement. *Civil Engineering and Installations 1* (2011), 79–86.

[36] Kaniyoor, A., Baby, T. T., and Ramaprabhu, S. Graphene synthesis via hydrogen induced low temperature exfoliation of graphite oxide. *J. Mater. Chem. 20* (2010), 8467–8469.

[37] Konsta-Gdoutos, M. S., Metaxa, Z. S., and Shah, S. P. Highly dispersed carbon

nanotube reinforced cement based materials. *Cement and Concrete Research 40*, 7 (2010), 1052 – 1059.

[38] Korpa, A., Kowald, T., and Trettin, R. Phase development in normal and ultra high performance cementitious systems by quantitative x-ray analysis and thermoanalytical methods. 69–76.

[39] Kysar, C. L. X. W. J., and Hone, J. Measurement of the elastic properties and intrinsic strength of monolayer graphene. *Science 321*, 5887 (July 2008), 385–388.

[40] Lam, L., Wong, Y., and Poon, C. Degree of hydration and gel/space ratio of high-volume fly ash/cement systems. *Cement and Concrete Research 30*, 5 (2000), 747 – 756.

[41] Larbi, J., Fraay, A., and Bijen, J. The chemistry of the pore fluid of silica fume-blended cement systems. *Cement and Concrete Research 20*, 4 (1990), 506 – 516.

[42] Larsen, M. B. B., Mackenzie, D. M., Caridad, J. M., Bøggild, P., and Booth, T. J. Transfer induced compressive strain in graphene: Evidence from raman spectroscopic mapping. *Microelectronic Engineering 121* (2014), 113 – 117.

[43] Lea, F. M. *The Chemistry of Cement and Concrete*. Edward Arnold (Publishers) Ltd, 1970.

[44] Lee, J.-U., Yoon, D., and Cheong, H. Estimation of young's modulus of graphene by raman spectroscopy. *Nano Letters 12*, 9 (2012), 4444–4448.

[45] Liang, X., Fu, Z., and Chou, S. Y. Graphene transistors fabricated via transfer-printing in device active-areas on large wafer. *Nano Letters 7*, 12 (2007), 3840–3844.

[46] Lim, D., and Oh, B. Experimental and theoretical investigation on the shear of steel fibre reinforced concrete beams. *Engineering Structures 21*, 10 (1999), 937 – 944.

[47] Liu, J., Yan, H., and Jiang, K. Mechanical properties of graphene platelet-reinforced alumina ceramic composites. *Ceramics International 39*, 6 (2013), 6215 – 6221.

[48] Lotya, M., Hernandez, Y., King, P. J., Smith, R. J., Nicolosi, V., Karlsson, L. S., Blighe, F. M., De, S., Wang, Z., McGovern, I. T., Duesberg, G. S.,

and Coleman, J. N. Liquid phase production of graphene by exfoliation of graphite in surfactant/water solutions. *Journal of the American Chemical Society 131*, 10 (2009), 3611–3620.

[49] Lotya, M., King, P. J., Khan, U., De, S., and Coleman, J. N. High-concentration, surfactant-stabilized graphene dispersions. *ACS Nano 4*, 6 (2010), 3155–3162.

[50] M. K. Blees, A. W. B., P. A. Rose, S. P. R., Kevek, J. W., B. Kobrin, D. A. M., and McEuen, P. L. Graphene kirigami. *Nature 524* (August 2015), 204–207.

[51] Magalhães, F., Caetano, E., Álvaro Cunha, Flamand, O., and Grillaud, G. Ambient and free vibration tests of the millau viaduct: Evaluation of alternative processing strategies. *Engineering Structures 45* (2012), 372 – 384.

[52] Mattevi, C., Kim, H., and Chhowalla, M. A review of chemical vapour deposition of graphene on copper. *J. Mater. Chem. 21* (2011), 3324–3334.

[53] Mohammed, A., Sanjayan, J., Duan, W., and Nazari, A. Incorporating graphene oxide in cement composites: A study of transport properties. *Construction and Building Materials 84* (2015), 341 – 347.

[54] Neville, A. *Properties of Concrete*. Pearson Education Limited, 1995.

[55] Novoselov, K., and Geim, A. The rise of graphene. *Nature Materials 6*, 3 (Mar 2007), 183–191.

[56] Odler, I. *Hydration, setting and hardening of Portland cement In: Lea's Chemistry of Cement and Concrete (P.C. Hewlett, editor)*. 03 2018.

[57] P. Kumar Mehta, P. J. M. M. *Concrete: Microstructure, Properties, and Materials*. Prentice-Hall, Inc, 1993.

[58] Pan, Z., He, L., Qiu, L., Korayem, A., Li, G., Zhu, J., Collins, F., Li, D., Duan, W., and Wang, M. Mechanical properties and microstructure of a graphene oxide-cement composite. *CEMENT AND CONCRETE COMPOSITES 58* (2015), 140–147.

[59] Pan, Z., He, L., Qiu, L., Korayem, A. H., Li, G., Zhu, J. W., Collins, F., Li, D., Duan, W. H., and Wang, M. C. Mechanical properties and microstructure of a graphene oxide–cement composite. *Cement and Concrete Composites 58* (2015), 140 – 147.

[60] Paredes, J. I., Villar-Rodil, S., Fernandez-Merino, M. J., Guardia, L., Martinez-Alonso, A., and Tascon, J. M. D. Environmentally friendly approaches toward the mass production of processable graphene from graphite oxide. *J. Mater. Chem. 21* (2011), 298–306.

[61] Park, S., and Ruoff, R. Chemical methods for the production of graphenes. *Nature Nanotechnology 4* (April 2010), 217–224.

[62] Paton, K. R., and Coleman, J. N. Scalable production of large quantities of defect-free few-layer graphene by shear exfoliation in liquids. *Nature Materials 13* (April 2014), 624–630.

[63] Petersson, P. Fracture energy of concrete: Practical performance and experimental results. *Cement and Concrete Research 10*, 1 (1980), 91 – 101.

[64] Pritula, O., Smrčok, L., Ivan, J., and Ižd inšk, K. X-ray quantitative phase analysis of residues of the reference portland clinkers. 34–39.

[65] R. Raccichini, A. Varzi, S. P., and Scrosati, B. The role of graphene for electrochemical energy storage. *Nature Materials 14* (December 2015), 271–279.

[66] Rafiee, M. A., Narayanan, T. N., Hashim, D. P., Sakhavand, N., Shahsavari, R., Vajtai, R., and Ajayan, P. M. Hexagonal boron nitride and graphite oxide reinforced multifunctional porous cement composites. *Advanced Functional Materials 23*, 45 (2013), 5624–5630.

[67] Richardson, I. The nature of the hydration products in hardened cement pastes. *Cement and Concrete Composites 22*, 2 (February 2000), 97–113.

[68] Richardson, I. The calcium silicate hydrates. *Cement and Concrete Research 38*, 2 (February 2008), 137–158.

[69] S. P. Shah, S. E. S., and Ouyang, C. *Fracture Mechanics of Concrete: Applications of Fracture Mechanics to Concrete, Rock, and Other Quasi-Brittle Materials*. John Wiley & and Sons, INC., 1995.

[70] Sanchez, F., and Sobolev, K. Nanotechnology in concrete – a review. *Construction and Building Materials 24*, 11 (2010), 2060 – 2071.

[71] Scrivener, K. L., Cabiron, J.-L., and Letourneux, R. High-performance concretes from calcium aluminate cements. *Cement and Concrete Research 29*, 8 (1999), 1215 – 1223.

[72] Scrivener, K. L., and Kirkpatrick, R. J. Innovation in use and research on cementitious material. *Cement and Concrete Research 38*, 2 (2008), 128 – 136. Special Issue — The 12th International Congress on the Chemistry of Cement. Montreal, Canada, July 8-13 2007.

[73] Sedaghat, A., Ram, M. K., Zayed, A., Kamal, R., and Shanahan, N. Investigation of physical properties of graphene-cement composite for structural applications. *Open Journal of Composite Materials 4*, 1 (January 2014), 12–21.

[74] Shahriary, L., and Athawal, A. Graphene oxide synthesized by using modified hummers approach. *International Journal of Renewable Energy Environmental Engineering 2014 2*, 1 (January 2014), 58–63.

[75] Sharma, S., and Kothiyal, N. Comparative effects of pristine and ball-milled graphene oxide on physico-chemical characteristics of cement mortar nanocomposites. *Construction and Building Materials 115* (2016), 256 – 268.

[76] Silvestre, N., and de Brito, J. Review on concrete nanotechnology. *European Journal of Environmental and Civil Engineering 20*, 4 (June 2015), 455–485.

[77] Sobolev, K., and Gutiérrez, M. How nanotechnology can change the concrete world. *American Ceramic Society Bulletin 84*, 10 (2005), 14–18. cited By 91.

[78] T. Tanabe, K. Sakata, H. M. R. S. K. M. H. N. *Creep Shrinkage and Durability Mechanics of Concrete and Concrete Structures*. Taylor and Francis Group, 2016.

[79] Varrla, E., Backes, C., Paton, K. R., Harvey, A., Gholamvand, Z., McCauley, J., and Coleman, J. N. Large-scale production of size-controlled mos2 nanosheets by shear exfoliation. *Chemistry of Materials 27*, 3 (2015), 1129–1139.

[80] W. Choi, I. Lahiri, R. S., and Kang, Y. Synthesis of graphene and its applications: A review. *Critical Reviews Solid State Materials Science 35* (February 2010), 52–71.

[81] W. Choi, I. Lahiri, R. S., and Kang, Y. S. Synthesis of graphene and its applications: A review. *Critical Reviews in Solid State and Materials Sciences 35*, 1 (2010), 52–71.

[82] Wang, X., Bai, H., Jia, Y., Zhi, L., Qu, L., Xu, Y., Li, C., and Shi, G. Synthesis of caco3/graphene composite crystals for ultra-strong structural materials. *RSC Adv. 2* (2012), 2154–2160.

[83] Wild, S., Sabir, B., and Khatib, J. Factors influencing strength development of concrete containing silica fume. *Cement and Concrete Research 25*, 7 (1995), 1567 – 1580.

[84] Wu, J., Liu, J., and Yang, F. Three-phase composite conductive concrete for pavement deicing. *Construction and Building Materials 75* (2015), 129 – 135.

[85] Wu, Z.-S., Ren, W., Gao, L., Liu, B., Jiang, C., and Cheng, H.-M. Synthesis of high-quality graphene with a pre-determined number of layers. *Carbon 47*, 2 (2009), 493 – 499.

[86] Xu, S., and Zhang, X. Determination of fracture parameters for crack propagation in concrete using an energy approach. *Engineering Fracture Mechanics 75*, 15 (2008), 4292 – 4308.

[87] Yamamoto, K., Fujimoto, K., Ametani, A., Sakai, K., Higano, A., and Watanabe, K. Current distribution and transient magnetic fields in an observatory of tokyo skytree. *Electric Power Systems Research 113* (2014), 64 – 69. Lightning Research and Lightning Protection Technologies.

[88] Yan, H., Tian, C., Sun, L., Wang, B., Wang, L., Yin, J., Wu, A., and Fu, H.

Small-sized and high-dispersed wn from clusters loading on go-derived graphene as promising carriers for methanol electro-oxidation. *Energy Environmental Science 7* (2014), 1939–1949.

[89] Yoon, D., Moon, H., Son, Y.-W., Choi, J. S., Park, B. H., Cha, Y. H., Kim, Y. D., and Cheong, H. Interference effect on raman spectrum of graphene on sio_2/Si. *Phys. Rev. B 80* (Sep 2009), 125422.

[90] Zhang, A. N. A. B. D. L. C., and Agarwal, A. Graphene reinforced metal and ceramic matrix composites: a review. *International Materials Reviews 62*, 5 (July 2016), 241–302.

[91] Zhao, J., Guo, Y., Li, Z., Guo, Q., Shi, J., Wang, L., and Fan, J. An approach for synthesizing graphene with calcium carbonate and magnesium. *Carbon 50*, 13 (2012), 4939 – 4944.

[92] Zhou, J., Zuo, Y., Wan, X., Long, G., Zhang, Q., Ni, W., Liu, Y., Li, Z., He, G., Li, C., Kan, B., Li, M., and Chen, Y. Solution-processed and high-performance organic solar cells using small molecules with a benzodithiophene unit. *Journal of the American Chemical Society 135*, 23 (2013), 8484–8487.